SOLID OXIDE CELL CONSTRICTION RESISTANCE EFFECTS

A Thesis
Presented to
The Academic Faculty

By

George J. Nelson

In Partial Fulfillment
Of the Requirements for the Degree
Master of Science in Mechanical Engineering

Georgia Institute of Technology

May 2006

SOLID OXIDE CELL CONSTRICTION RESISTANCE EFFECTS

Approved by:

Dr. Comas Haynes, Research Co-Advisor
Georgia Tech Research Institute
Georgia Institute of Technology

Dr. Jianmin Qu, Academic Co-Advisor
School of Mechanical Engineering
Georgia Institute of Technology

Dr. Sam Shelton
School of Mechanical Engineering
Georgia Institute of Technology

Date Approved: April 3, 2006

ACKNOWLEDGEMENTS

The present work was completed with the assistance of many people. I would first like to thank Dr. Comas Haynes, my primary research advisor, for the guidance he provided throughout the course of this project. I would also like to thank Dr. Jianmin Qu, my academic co-advisor, and Dr. Sam Shelton who, as members of my reading committee, enabled the further refinement of this work. Additionally, I would like to thank Dr. Tommaso Pacini and Chris Raczynski for their assistance on various technical aspects of this work.

Furthermore, I would like to thank my parents, Robert and Carol Nelson. In addition to providing their parental support, each served as an informal committee member by lending technical and editorial advice, respectively.

Finally, and most of all, I would like to thank my lovely and amazing fiancée Jennifer Indech. Through her love, support, and encouragement she enables the full realization of my potential.

TABLE OF CONTENTS

LIST OF TABLES

LIST OF FIGURES

NOMENCLATURE

a	Unit Cell Half Width, m or cm
ASR	Electronic Area Specific Resistance (Ω-cm^2)
ASR_{diff}	Diffusion Area Specific Resistance (s/m)
b	Fuel Stream Half Width, m or cm
C	Molar Concentration, mol/m^3
$\overline{C}$	Average Molar Concentration, mol/m^3
D_{ij}	Binary Diffusion Coefficient, m^2/s
E_o	Nernst Potential, V
F	Faraday Constant, C/mol
i''	Current Density, A/m^2 or A/cm^2
i''_{cs}	Cathode Limiting Current Density, A/m^2 or A/cm2
i_o	Exchange Current Density, A/m^2 or A/cm2
J''	Molar Flux Rate, mol/m^2-s
L_{Total}	Unit Cell Total Width, m or cm
L_{FS}	Fuel Stream Contact Width, m or cm
LF	Length Fraction
p	Partial pressure, kPa
$\overline{p}$	Average Partial pressure, kPa
r_c	Delamination Crack Radius, m or cm
R_0	Outer Radius of Delamination Button-Cell, m or cm
R_u	Universal Gas Constant, kJ/mol-K

T	Temperature, K
t	Thickness, m or cm
V	Voltage, V
$\overline{V}$	Average Voltage, V

Greek Symbols

α	Charge Transfer Coefficient,
ε	Anode Porosity
σ	Electronic or Ionic Conductivity, $(\Omega\text{-cm})^{-1}$ or S/cm
τ	Anode Tortuosity

Recurring Subscripts

an	Bulk Anode Parameter
an-elec	Anode-Electrolyte Interface
an-FS	Anode-Fuel Stream Interface
an-IC	Anode-Interconnect Interface
cath	Bulk Cathode Parameter
eff	Effective
elec	Bulk Electrolyte Parameter
FD	Fuel Depletion
H_2	Hydrogen
H_2O	Steam

SUMMARY

Solid oxide cells are best known in the energy sector as novel power generation devices through solid oxide fuel cells (SOFCs), which enable the direct conversion of chemical energy to electrical energy and result in high efficiency power generation. However, solid oxide electrolysis cells (SOECs) are receiving increased attention as a hydrogen production technology through high temperature electrolysis applications. The development of higher fidelity methods for modeling transport phenomena within solid oxide cells is necessary for the advancement of these key technologies. The proposed thesis analyzes the increased transport path lengths caused by "constriction resistance" effects in prevalent solid oxide cell designs. Such effects are so named because they arise from reductions in active transport area.

Constriction resistance effects of SOFC geometry on continuum level mass and electronic transport through SOFC anodes are simulated. These effects are explored via analytic solutions of the Laplace equation with model verification achieved by computational methods such as finite element analysis (FEA). Parametric studies of cell geometry and fuel stream composition are performed based upon the models developed. These studies reveal a competition of losses present between mass and electronic transport losses and demonstrate the benefits of smaller SOFC unit cell geometry. Furthermore, the models developed for SOFC transport phenomena are applied toward the analysis of SOECs. The resulting parametric studies demonstrate that geometric configurations that demonstrate enhanced performance within SOFC operation also demonstrate enhanced performance within SOEC operation.

Secondarily, the electrochemical degradation of SOFCs is explored with respect to delamination cracking phenomena about and within the critical electrolyte-anode interface. For thin electrolytes, constriction resistance effects may lead to the loss of electro-active area at both anode-electrolyte and cathode-electrolyte interfaces. This effect (referred to as "masking") results in regions of unutilized electrolyte cross-sectional area, which can be a critical performance hindrance. Again analytic and computational means are employed in analyzing such degradation issues.

CHAPTER 1

INTRODUCTION

Solid oxide cells are an environmentally attractive technology that could play a key role in the development of a more sustainable global energy infrastructure. Solid oxide cells are best known in the energy sector as novel power generation devices via solid oxide fuel cells (SOFCs), which enable the direct conversion of chemical energy to electrical energy. Through this direct conversion of chemical energy, SOFCs can eliminate many of the power generation losses associated with thermal and mechanical energy conversion methods. In addition to their direct energy conversion benefits, fuel cells produce fewer criteria pollutants than combustion-based technologies by operating below the temperature ranges associated with thermal NO_x formation and operating upon desulfurized fuels. Finally, SOFCs allow for more modular designs, cogeneration, and more flexible siting options than most current combustion-based technologies [1].

In addition to fuel cell applications, solid oxide cells are receiving increased attention via solid oxide electrolysis cells (SOECs), which enable the production of hydrogen through high temperature electrolysis driven by various power sources (e.g., nuclear [2-3]). In high temperature electrolysis applications solid oxide cells offer the distinct advantage of lowered power input requirements due to the enhanced thermodynamics and chemical kinetics associated with higher temperatures [2, 3]. Furthermore, hydrogen production via high temperature electrolysis of steam does not require the use of fossil fuels as a feedstock (as in steam reformation) and does not involve corrosive environments (as in thermochemical methods) [3].

The development of higher fidelity methods for modeling transport phenomena within solid oxide cells is necessary for the advancement of these key technologies. The present work develops one such method through the analysis of increased transport path lengths caused by "constriction resistance" effects in prevalent solid oxide cell designs. Such effects are so named because they arise from reductions in active transport area, which can result from interconnect contact geometry effects or electrochemical and thermo-mechanical degradation of cell components. These effects are explored using analytic solutions of the Laplace equation and computational methods such as finite element analysis (FEA).

A thorough understanding of mass and electrical transport within solid oxide fuel cell component layers is necessary for the development of future SOFC systems. Prevalent analyses of these key transport phenomena are often conducted employing a herein-labeled "button-cell" approximation in which one-dimensional transport is presumed to occur within the SOFC electrodes (Figure 1.1). This approximation is employed in both theoretical and experimental analyses [4-6]. In such analyses the effects of actual SOFC interconnect geometry are not directly addressed. However, given actual SOFC operation, contact between the gas stream and anode surface is restricted to a fuel channel defined by the interconnect geometry. Thus, contact between the gas stream and anode occurs over only a portion of the anode surface. It is known that the change in cross-sectional area from the fuel stream-anode to the anode-electrolyte interface, due to interconnect design, will affect mass transfer significantly compared to the present button-cell idealization of mass transfer in SOFCs. Similarly, the reduction in electrical cross-sectional area from the electrolyte-anode interface to the anode-solid

contact interface, due to interconnect design, causes a distortion of electronic current and thus increases ohmic losses. These additional resistances are due to the added path lengths associated with multi-dimensional flow within the electrode (Figure 1.2).

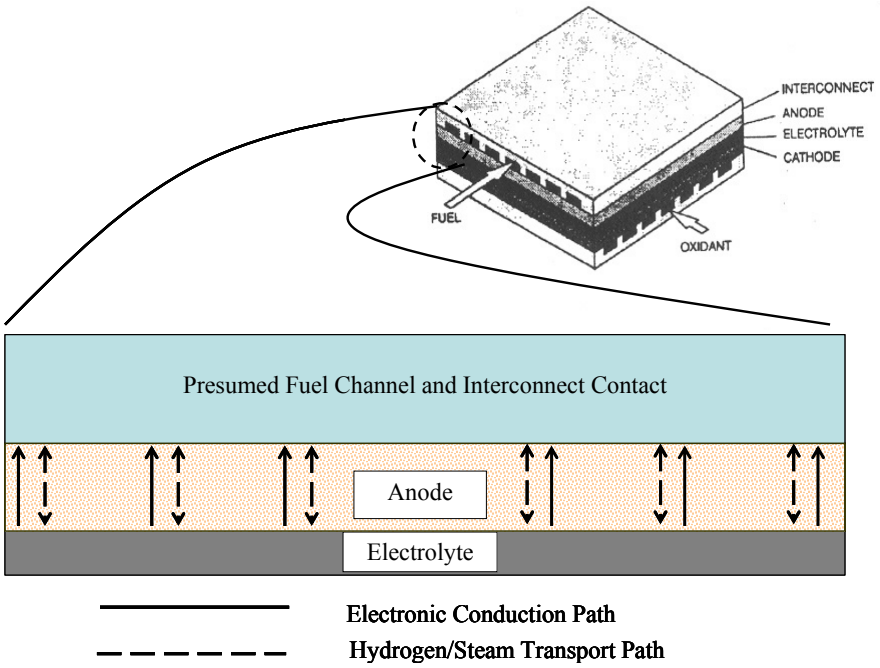

Figure 1.1. The button-cell model of a planar SOFC

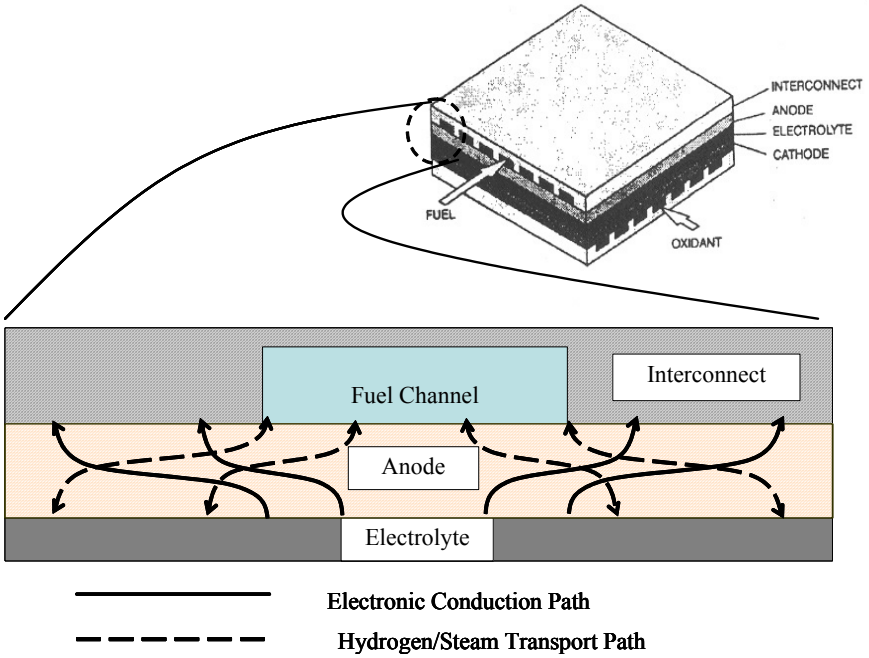

Figure 1.2. Model of actual planar SOFC geometry

The present work demonstrates that in steady-state operation solid oxide fuel cell geometry effects can be examined in a straightforward manner employing the analytic solution of the Laplace equation over a rectangular domain. This approach is applied toward the anodic voltage and partial pressure distributions by the establishment of three boundary value problems: one for hydrogen transport, one for steam transport, and one for the voltage distribution. The use of a simplified potential flow approach to the partial pressure problems is made possible primarily through the basic assumptions of equimolar counterdiffusion of hydrogen and steam within the anode and that for large anode thicknesses (250+ μm) relatively thin reaction zones (~10 μm) may be presumed [6]. A uniform pressure distribution across the fuel channel cross-section is also assumed as a result of low resistance to convective mass transport within the fuel channel when compared to the resistance to diffusion within the anode. It is important to note that present analyses are conducted for a two-dimensional cross-section of an SOFC. While the effects of pressure drop along the length of the SOFC fuel channel will also influence cell performance, they are not considered in the present work. This exclusion allows for the greater emphasis on the performance effects of two-dimensional transport in SOFCs.

Solution of the previously mentioned boundary value problems allows for the formulation of basic anodic transport models. The models developed from these potential flow solutions are verified using FEA. It is shown that anode and interconnect geometry have a significant effect upon anodic resistance to mass and electronic transport. The nature of the effects and their relation to cell geometry establish a competition of losses between anodic ohmic and concentration polarizations. Parametric studies of cell geometry, current loading, and fuel stream composition are performed

based upon the analytic models developed, and the optimization of cell geometry based upon these studies is discussed. Development of these studies is carried out through a design of experiments approach. The effects of anode thickness and permeability, fuel channel and interconnect width, current loading, and fuel stream hydrogen content are emphasized.

Additionally, the models developed for geometry effects on SOFC anodic transport phenomena are leveraged toward the analysis of SOECs. This application is made possible by the common physics that govern SOFC and SOEC operation. Essentially, the electrolysis cell is treated as a fuel cell operated under reversed current and mass flow regimes, with an applied voltage allowing for the production of hydrogen. The optimization of SOEC geometry is discussed based upon parametric studies similar to those mentioned above. The existence of an optimum geometry for reversible solid oxide cells is proposed. Such a dual-mode solid oxide cell would allow for hydrogen production or power generation as warranted by market demands.

Secondarily, constriction resistance effects associated with the electrochemical degradation of SOFCs is explored with respect to delamination cracking phenomena about and within the critical electrolyte-anode interface. These phenomena can result from processing imperfections or mismatched thermal expansion characteristics within SOFC electrode-electrolyte assemblies. The increased internal ohmic losses caused by delamination cracks located at the electrode-electrolyte interfaces are emphasized in the present work. Delamination cracks are treated as current flow obstructions that lead to the distortion of current within the electrolyte. For thin electrolytes, these constriction resistance effects may lead to the loss of electroactive area at both anode-electrolyte and

cathode-electrolyte interfaces, via actual and "virtual" delamination. Additionally, regions of unutilized electrolyte cross-sectional area may result. These collective phenomena are referred to as masking and can result in regions of unutilized electrolyte cross-sectional area, which can be a critical performance hindrance.

For ionic transport within SOFC electrolytes the potential flow model is particularly relevant. Assuming an idealized circular delamination footprint, a delamination crack may be modeled using the analytic solution of the Laplace equation within a cylindrical domain. Although an analytical solution exists for this problem, a singularity is encountered about the crack tip, which results in slow convergence of the solution. Computational methods used in analogous thermal conduction cases are applied to ionic conduction within the fuel cell electrolyte in an attempt to resolve the convergence issues encountered in the analytic solution. Finite element analysis studies based upon the thermal analogy to ionic conduction are employed. These studies are applied toward the development of three dimensionless parameters. A dimensionless electrolyte thickness parameter is developed by relating electrolyte thickness to crack radius, and a dimensionless current parameter is developed as a function of this dimensionless electrolyte thickness. The relation of these parameters and a threshold at which masking will occur is proposed. A method is proposed for incorporating the electrochemical effects of delamination within full cell- and stack-level simulations via a dimensionless radius. This dimensionless radius is developed through relating crack radius to the radial distance at which ionic conduction within the electrolyte is primarily in the axial direction.

CHAPTER 2

LITERATURE REVIEW

The concept of constriction resistance is well known within engineering practice, and is most commonly encountered in problems involving the study of thermal and electrical contact resistance. The thermal or electrical resistance between the contacting media can be described in terms of resistance to potential flow caused by a reduction in conducting area. This reduction in area stems from the fact that the contacting surfaces are not in perfect contact. Instead, these surfaces are comprised of microscopic contact spots resulting from the contact of raised portions of the rough surfaces as shown in Figure 2.1 [7-9]. The flow of potential for each constriction is modeled as contained within a larger semi-infinite cylinder, or flux column, that has a uniform flow at distances far from the contact interface. At the level of the microscopic contacts the heat flow within each column is forced through a constricted region creating a resistance to flow of heat or electric current.

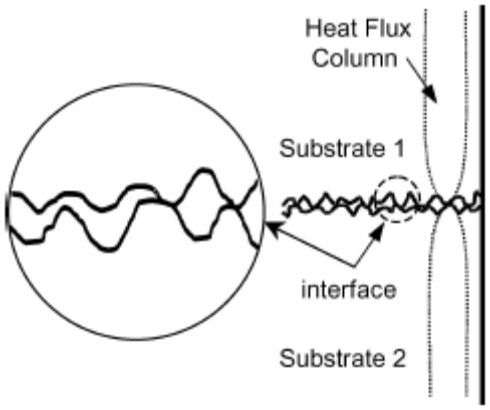

Figure 2.1. Contact geometry of two heat conducting media [7]

The concept of constriction resistance caused by micro-contacts was most notably studied by Greenwood [8]. More contemporary studies of thermal and electrical contact resistance can be found in the work of Black, et al. [7], Rostami, et al. [10], and Timsit [9]. An in-depth review of thermal and electrical contact resistance literature is beyond the scope of the present work. However, a brief discussion of the methods employed in solving such problems is warranted since they served as the initial inspiration for the present work.

Potential flow between contacting media is governed by the Laplace equation in multiple dimensions.

$$\nabla^2 T = 0 \text{ or } \nabla^2 V = 0 \tag{2.1}$$

For most analyses, Equation (2.1) is solved over a cylindrical domain independent of the angular dimension [7, 9, 11], but analyses over multi-dimensional rectangular domains have also been performed [10]. While solution of the Laplace equation can be straightforward, a common trait of contact resistance analyses is that the domains are semi-infinite in at least one direction, a complication that often requires numerical techniques to achieve a solution. Most contemporary analyses employ computational fluid dynamics as a numerical technique [7, 10].

The concept of constriction resistance can be leveraged toward solid oxide cell transport phenomena by analyzing the effects of reductions in cross-sectional area that can occur between cell component layers. The reduction in cross-sectional area between the anode-electrolyte interface and anode-fuel stream/interconnect interface reduces the active transport area thereby constricting the flow of mass or electric current. Similarly, cracking about the electrolyte-electrode interfaces can create such a reduction in active

transport area. As in the case of thermal or electrical contact resistance a perceived contact region is replaced with a smaller region of real contact, which restricts the flow of mass or electric current. Characterization of the resulting resistance effects is crucial to the greater understanding of solid oxide cell transport phenomena.

Most analyses of solid oxide fuel cell transport phenomena typically rely upon a simplified button-cell approximation, which has been explained previously. In experimental works, such as those of Zhao and Virkar [5] and Kim, et al. [6], this approximation is created through the use of a metallic wire mesh as a current collector, as shown in Figure 2.2 below. Such current collectors are laid across the fuel and air sides of a single cell to achieve uniform mass and electronic contact areas over the entire cell surface. While ensuring such contact is vital for consistent experimental results, it does not serve to recreate the common operational contact conditions of SOFCs.

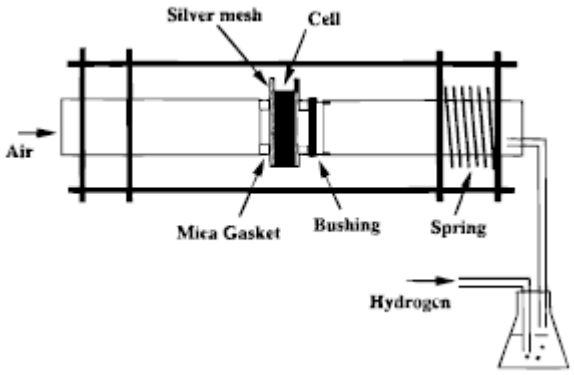

Figure 2.2. SOFC set-up employing wire mesh for enhanced contact [6]

While efforts to more accurately model geometry effects have been made, those employing analytical methods toward understanding geometry effects have focused more on developing general expressions for cell concentration and ohmic polarization [12] and

typically rely upon a one-dimensional characterization of transport [4, 13]. Chan and Xia explicitly treat electronic and ionic transport phenomena as one-dimensional in their analysis of SOFC polarization effects through the application of Ohm's law to describe the distribution of potential across electronic and ionic conducting materials within a SOFC [4]. Gemmen and Johnson establish a button-cell approximation by assuming one-dimensional transport behavior in the direction parallel to the flow of reactants within the fuel and air channels [14]. Other models recognize the significance of interconnect geometry effects, but leave such effects for consideration in the development of appropriate model parameters [15].

Analyses seeking a more detailed description of transport phenomena rely heavily upon numerical techniques to ascertain the multidimensional characteristics of SOFC transport phenomena [2, 16-19]. Campanari, et al. solve thermal and electrochemical equations for current flow, cell power output, reactant and product compositions, and temperature distributions for single finite volumes similar to that defined in Figure 2.3 [17]. These finite volumes are then linked via appropriate boundary conditions to construct a thermal and electrochemical model of a single planar SOFC. In addition to the finite volume method employed in the thermal and electrochemical calculations, this model relies upon computational fluid dynamics (CFD) to model reactant distributions within the fuel channel. Ferguson, et al., also apply the finite volume method toward modeling the thermal and mass transport within an electrolyte supported solid oxide fuel cell [16]. A key result of this work is that the effects of interconnect rib size on cell efficiency are demonstrated, and the cross-sectional distribution of hydrogen within the anode is calculated for several anode thicknesses. Ohmic losses are shown to be reduced

by broader interconnect ribs. However, the interconnect is shown to reduce hydrogen concentration in regions not directly beneath the anode-fuel stream interface. A competition between ohmic and concentration polarization within the anode, arising from cell geometry, can be inferred from these results.

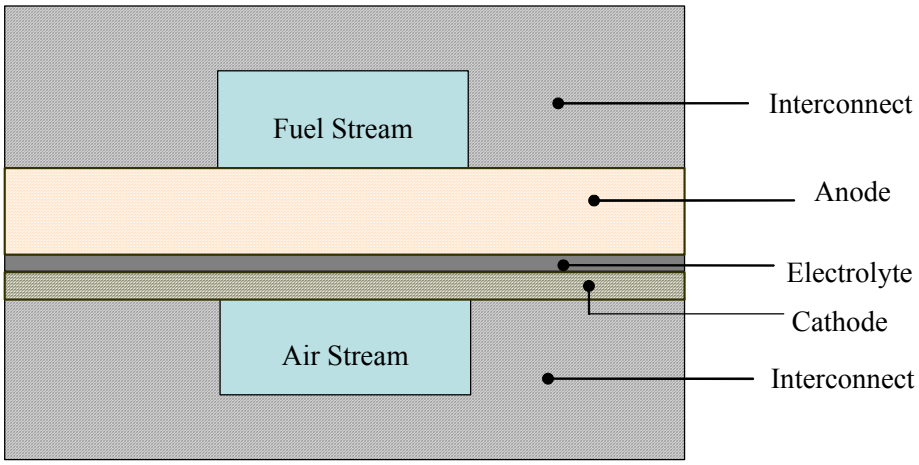

Figure 2.3. Cross-sectional view of SOFC finite volume

In addition to finite volume approaches, finite element analysis (FEA) has been applied to the modeling of SOFC transport phenomena. Khaleel, et al., use FEA to develop an electrochemical model of a SOFC, but, as noted, the model developed does not consider the effects of interconnect geometry on cell transport characteristics [15]. Fleig and Maier, and later Fleig, et al., used FEA to determine the effects of electrode-electrolyte contact on potential distributions within the electrolyte layer of a solid oxide fuel cell [18, 19]. This work serves as the most express application of the concept of constriction resistance to the analysis of SOFC transport phenomena. Ultimately, Fleig demonstrated that triple-phase boundaries at the electrode-electrolyte interface act as

constrictions within the flow of current through the electrolyte and increases the electrolyte resistance [19].

Attempts have been made to describe the effects of SOFC interconnect geometry via analytical methods [12, 13]. Lin, et al., examined the effects of rib width on planar SOFC concentration polarization using discretized integration across the width of the anode. Sources of mass flow were assumed to decay exponentially throughout the anode thickness as distance from the anode-fuel stream interface increased. Step functions were employed to account for the proximity of the interconnect rib to a given location across the anode width. The pressure at a given location was the found through the summation of seven separate integrals calculated across the anode width. While an analytic representation of concentration polarization losses resulted from this work, it was not a particularly straightforward approach.

Cameron and Virkar examined the effects of interconnect geometry on solid oxide fuel cell ohmic polarization losses via analytic solution of a one–dimensional, second order ordinary differential equation for cell voltage. What is unique in their analysis is that the distribution of voltage varies only along the width of the cell electrodes but not through the thickness of the cell electrodes. Using this model, Cameron and Virkar demonstrate that the common one-dimensional rectangular interconnect contact geometry, as shown in Figure 2.3 and in the previous chapter, is superior to a two-dimensional circular interconnect contact geometry.

While interconnect geometry holds strong influence over SOFC performance, the degradation of cell components is also an important factor in cell performance. Delamination cracking about the electrode-electrolyte interfaces within SOFC component

layers has been demonstrated to be a significant issue in the performance of solid oxide fuel cells. Hsiao and Selman, and Radovic, et al., both demonstrated the occurrence of delamination between the anode and electrolyte component layers of planar SOFC materials [20, 21]. Although the occurrence of delamination can result in the total failure of a SOFC, small non-catastrophic delaminations may also affect performance over the cell lifetime. Hsiao and Selman demonstrated increases in cathode impedance over test cell lifetimes that coincided with the anode component layer delaminating from the electrolyte layer. That the delamination crack blocked the conduction path of ions across the electrolyte was suggested as a cause for this increase in cathode impedance. Additionally, analyses of SOFC system performance have demonstrated that distributions of microcracks can cause significant decreases in cell performance [22]. As in Fleig's analyses of electrode-electrolyte contact [18, 19], a delamination serves to increase the constriction of current flow through cell component layers by reducing the available contact area. Thus the use of the concept of constriction resistance in the analysis of delamination effects on cell performance is of great importance in achieving a greater understanding of solid oxide cell electrochemical degradation.

Under reversed current flow conditions a solid oxide cell can be used for hydrogen production via electrolysis. Treating solid oxide electrolysis cells as reversed operation solid oxide fuel cells is a common practice. This approach is employed by Gemmen and Johnson in their analysis of load transient effects [14], and it is expressly stated by Eguchi, et al., in their experimental characterizations of solid oxide cells [23].

As in the analysis of SOFCs, the performance of solid oxide electrolysis cells has most notably been analyzed using numerical and experimental methods. Hawkes, et al.,

modeled the performance of a SOEC using the computational fluid dynamics software FLUENT and verified this model via experiment on a bench-top SOEC stack [2]. Additional experimental characterizations of this set-up are documented by O'Brien, et al. [3]. Unlike prevalent SOFC experimental analyses, this work was conducted using what is designed to be an operational cell stack configuration.

An advantage of the reversible nature of solid oxide cells is that production of hydrogen or power can be controlled based upon its economic merit. However, whether optimum SOEC geometry coincides with optimum SOFC geometry is yet to be determined. Extant dedicated SOECs typically employ planar configurations with thick electrolytes and relatively thin anodes [2, 3], while the trend in SOFC geometry favors planar anode supported cells with thin electrolytes and thicker electrodes. Furthermore, under fuel cell operation, a solid oxide cell is an exothermic system, and, under electrolysis mode, it is endothermic. The effects of thermal cycling between these modes may lead to significant reliability issues within reversible solid oxide cells.

While it is an active area of research, the modeling of multidimensional transport within solid oxide cells is also a nascent area of research. More in-depth description of the resistance effects rising from solid oxide fuel cell component geometry and electrochemical degradation is necessary for further technological development. The enhanced modeling of key mass and electronic transport phenomena can be achieved via classical analytic techniques, specifically potential flow theory. Models developed from these classical techniques can be used to gain greater insight into the design and operation of cell component layers.

CHAPTER 3

GEOMETRY EFFECTS

3.1 Analytic Models

Steady-state operation of SOFCs that incorporate hydrogen-steam fuel feed allows for the examination of interconnect geometry effects through analytic solutions of the Laplace equation. This is made possible through the basic assumptions of equimolar counterdiffusion of hydrogen and steam within the anode and that for large anode thicknesses (250+ μm) relatively thin reaction zones (~10 μm) may be presumed [6]. A uniform pressure distribution across the fuel channel (i.e., within the plane of the cross-sectional view) is also assumed as a result of low resistance to convective mass transport within the fuel channel when compared to the resistance to diffusion within the anode. The performance effects of the pressure drop along the length of the fuel channel are not considered in the present work. These effects will also affect cell performance and will therefore require consideration in future analyses.

The first of these assumptions, equimolar counterdiffusion, enables the use of Fickian diffusion by the elimination of the molar average velocity terms that would typically require consideration for characterizing diffusion. The diffusion of hydrogen from the fuel stream to the anode-electrolyte interface is balanced by the diffusion of steam from the anode-electrolyte interface to the fuel stream. In the process, the molar average velocity of each constituent cancels the molar average velocity of the other. The assumption of thin reaction zones, supported by the work of Kim, et al. [6], allows for the

neglect of internal generation of both charge and species (hydrogen and steam) within the anode.

The final assumption is justified via a brief comparison of the diffusive and convective mass transfer resistances. The diffusive mass transfer resistance is defined as

$$R_{Diff} = \frac{t_{anode}}{D_{H_2,eff} A_s} \tag{3.1}$$

Where t_{anode} is the anode thickness ~750 μm, and A_s is the surface area of the anode in contact with the fuel flow channel. As defined in Kim, et al. [6] the *effective* diffusion coefficient of hydrogen in the anode, $D_{H2,eff}$, is given by

$$D_{H_2,eff} = \frac{\varepsilon}{\tau} D_{H_2-H_2O} \tag{3.2}$$

The binary diffusion coefficient for a hydrogen-steam mixture, $D_{H2\text{-}H2O}$, is defined using the Chapman-Enskogg model as outlined by Reid et al. [24]. The variables ε and τ are the anode porosity and tortuosity, respectively; their ratio is the anodic permissivity.

The convective mass transfer resistance is defined as

$$R_{conv} = \frac{D_h}{D_{H_2-H_2O} \cdot Sh \cdot A_s} \tag{3.3}$$

Here,

D_h = flow channel hydraulic diameter = $4wh/(2w+2h)$
w = flow channel width
h = flow channel height
Sh = Sherwood Number

It should be noted that the binary diffusion coefficient for the hydrogen-steam mixture is used because the convective mass transfer resistance relates to diffusion within the fuel stream, which would have a permissivity of 1.0.

Flow channel geometry was taken to be on the order of 1 mm. A nominal flow channel height of 1 mm was assumed. Flow channel widths were varied to provide aspect ratios ranging between 1.0 and 8.0. These ratios were used in determining the Sherwood number [25]. The ratio of convective to diffusive mass transfer resistance can be found from equations (3.1) and (3.3)

$$R_{ratio} = \frac{R_{conv}}{R_{cond}} = \frac{D_h \cdot \varepsilon}{t_{anode} \cdot Sh \cdot \tau} \tag{3.4}$$

As shown in Table 3.1, the convective mass transfer resistance within the fuel channel is 2-3% the diffusive mass transfer resistance. For the present model, the diffusive resistance is therefore considered to be the dominant resistance.

Table 3.1. Ratio of convective to conductive mass transfer resistance

Width, w	Aspect Ratio	Sh	R_{ratio}
1.00	1.00	2.98	0.027
2.00	2.00	3.39	0.031
3.00	3.00	3.96	0.030
4.00	4.00	4.44	0.029
5.00	5.00	4.84	0.028
6.00	6.00	5.16	0.027
7.00	7.00	5.41	0.026
8.00	8.00	5.60	0.025

3.1.1 Unit Cell Geometry

A unit cell is defined as a single fuel channel bordered by corresponding solid contact regions, as shown in Figure 1. The lengths *a* and *b* are defined as half the total unit cell width and half the fuel stream width, respectively. A symmetry boundary condition is applied about the centerline of the fuel channel to further simplify the unit cell geometry. Finally, a dimensionless length fraction (LF) is defined to compare the fuel stream contact length to the total unit cell length.

$$a = \frac{L_{Total}}{2}; \quad b = \frac{L_{FS}}{2}; \quad LF = \frac{b}{a} = \frac{L_{FS}}{L_{Total}} \tag{3.5}$$

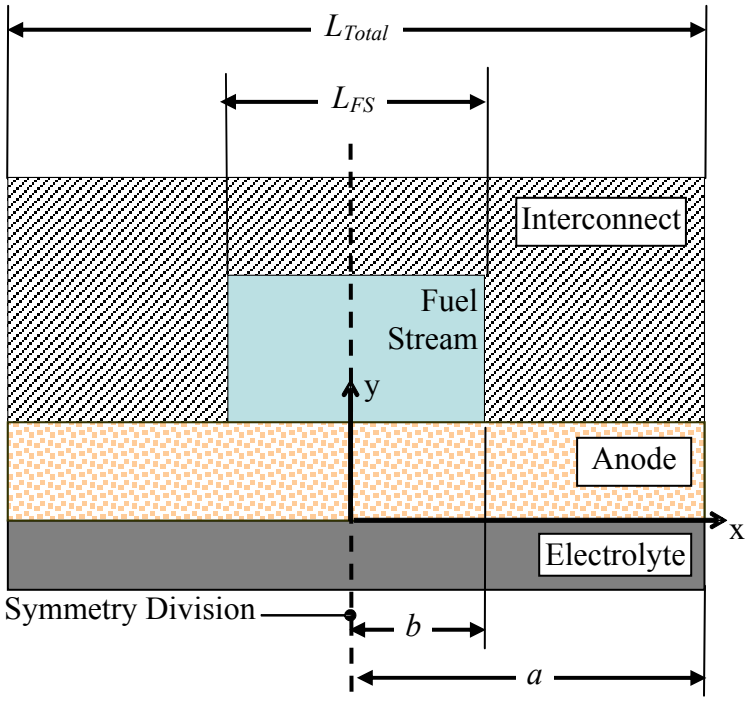

Figure 3.1. Unit cell geometry employed in present analysis

3.1.2 Anode Partial Pressure Model

The boundary value problem for the hydrogen partial pressure is defined in Equations (3.6)-(3.9). This problem consists of the Laplace equation with no generation within the anode. Constant species flux boundary conditions are specified at the anode-electrolyte and anode-fuel stream interfaces. These boundary conditions, shown in Equations (3.7) and (3.8), are based upon an *a priori* assumption of uniform flux at the anode-electrolyte and anode-fuel stream interfaces. The appropriateness of this assumption is presumed adequate, but it will be further investigated in future work. A zero species flux boundary condition is specified at the anode-interconnect interface. A corresponding problem can be defined for the steam partial pressure by reversing the sign of the boundary conditions given in Equations (3.7) and (3.8). The domain studied in the development of the anode partial pressure model is shown in Figure 3.2. This domain is also used in the development of the anode voltage model.

$$\frac{\partial^2 p_{H_2}}{\partial x^2} + \frac{\partial^2 p_{H_2}}{\partial y^2} = 0 \tag{3.6}$$

$$\frac{\partial p_{H_2}}{\partial y}(x,0) = \frac{R_u T}{2FD_{H2-H2O}} \frac{\tau}{\varepsilon} i'' = A_0 \tag{3.7}$$

$$\frac{\partial p_{H_2}}{\partial y}(x,t_{an}) = \begin{cases} \dfrac{R_u T}{2FD_{H2-H2O}} \dfrac{a}{b} \dfrac{\tau}{\varepsilon} i''; & 0 < x < b \\ 0, & b < x < a \end{cases} \tag{3.8}$$

$$\frac{\partial p_{H_2}}{\partial x}(0,y) = 0 \,, \quad \frac{\partial p_{H_2}}{\partial x}(a,y) = 0 \tag{3.9}$$

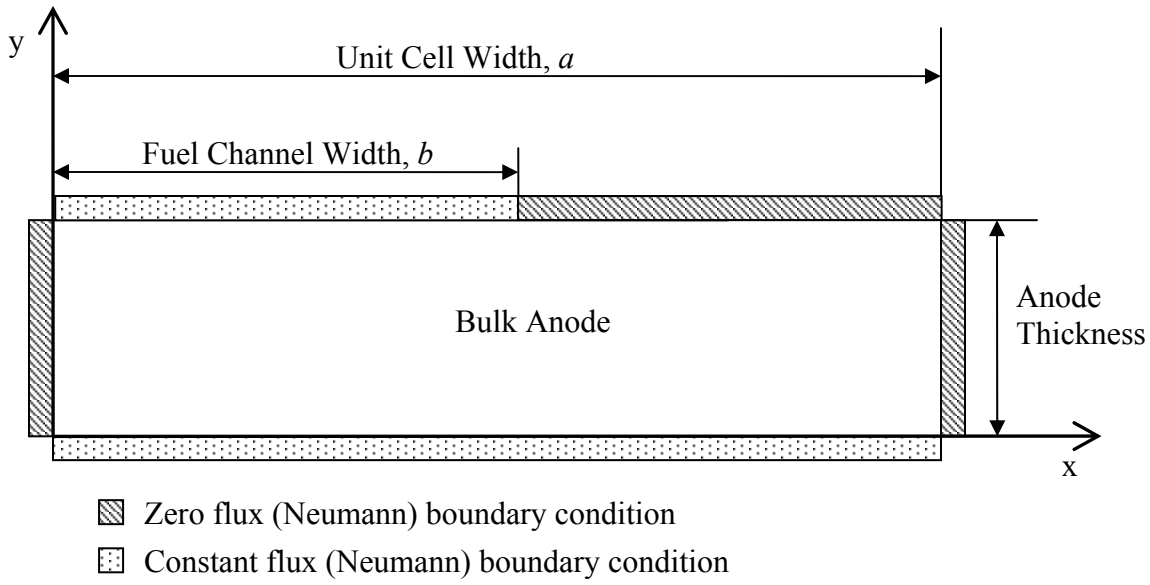

Figure 3.2. Domain studied for potential flow model development

The scaling factor, *a/b*, in Equation (3.8) is the result of species conservation and the reduction in area between the respective interfaces. The molar flow rates of the species *i* at each interface are equated, and the anode-fuel stream molar flux is found. This calculation readily reveals the scaling relationship.

$$\dot{n}_{i,an-FS} = \dot{n}_{i,an-elec}$$

$$J''_{i,an-FS} \int dA_{an-FS} = J''_{i,an-elec} \int dA_{an-elec}$$

$$J''_{i,an-FS} = J''_{i,an-elec} \frac{a}{b}$$

The solution to the hydrogen partial pressure problem is given in Equation (3.10). The solution for the corresponding steam partial pressure distribution is given in Equation (3.11). It is important to note that the sum of these solutions is equal to the set total pressure at all locations within the anode. Also of importance is the presence of hyperbolic and trigonometric functions in the series term of each solution. The nature of

these functions provide for swift convergence of the series term, hence a reduced calculation time.

$$p_{H_2}(x,y) = p_{H_2,an-FS} - A_0(t_{an} - y) - \sum_{n=1}^{\infty} A_n\left[\cosh(\lambda_n t_{an}) - \cosh(\lambda_n y)\cos(\lambda_n x)\right] \tag{3.10}$$

$$p_{H_2O}(x,y) = p_{H_2O,an-FS} + A_0(t_{an} - y) + \sum_{n=1}^{\infty} A_n\left[\cosh(\lambda_n t_{an}) - \cosh(\lambda_n y)\cos(\lambda_n x)\right] \tag{3.11}$$

$$A_n = \frac{2A_0\sin(\lambda_n b)}{n\pi\lambda_n \sinh(\lambda_n t_{an})}\left(\frac{a}{b}\right); \quad \lambda_n = \frac{n\pi}{a} \tag{3.12}$$

3.1.3 Anode Voltage Model

A similar potential flow problem can be solved to find the anode voltage distribution. Similar to the partial pressure case, the assumption of no internal charge generation is applied. Flux boundary conditions are applied, with the composite Neumann boundary condition Equation (3.15) reversed to account for electrical contact at the anode-interconnect interface. As in the partial pressure model, the scaling factor can be derived by applying charge conservation and accounting for the reduction in area between the anode-electrolyte and anode-interconnect interfaces.

$$\frac{\partial^2 V}{\partial x^2} + \frac{\partial^2 V}{\partial y^2} = 0 \tag{3.13}$$

$$\frac{\partial V}{\partial y}(x,0) = \frac{i''}{\sigma_{an}} \tag{3.14}$$

$$\frac{\partial V}{\partial y}(x,t_{an}) = \begin{cases} 0; & 0 < x < b \\ \dfrac{i''}{\sigma_{an}\left(1-\dfrac{b}{a}\right)}, & b < x < a \end{cases} \tag{3.15}$$

$$\frac{\partial V}{\partial x}(0,y) = 0\ ,\ \frac{\partial V}{\partial x}(a,y) = 0 \tag{3.16}$$

The solution obtained takes the following form

$$V(x,y) = \overline{V}_{an-elec} + \frac{i''}{\sigma_{an}} y + \sum_{n=1}^{\infty} A_n \cosh(\lambda_n y)\cos(\lambda_n x) \tag{3.17}$$

In Equation (3.17), $\overline{V}_{an-elec}$, is the average voltage at the anode-electrolyte interface. The necessary constants are defined as follows

$$A_n = \frac{-2i''\sin(\lambda_n b)}{n\pi\sigma_{an}\left(1-\dfrac{b}{a}\right)\lambda_n \sinh(\lambda_n t_{an})}; \quad \lambda_n = \frac{n\pi}{a} \tag{3.18}$$

An expression for the average anode-electrolyte voltage is developed using Equations (3.19) through (3.22). The total cell voltage can be defined by subtracting the anode lead voltage from the cathode lead voltage (Equation (3.19)). The cathode lead voltage used in the present work was set at 1.0 V. Although this is an arbitrary setting, it facilitates the establishment of a numerical baseline for the desired analysis and is approximately representative of an ideal Nernst potential value. Additionally, the cell voltage can be defined by subtracting the electrochemical losses from the Nernst potential, E_o. These losses include those caused by the ohmic resistance within the

anode, cathode, and electrolyte layers (ASR_{total}), cell activation losses, and the cathode concentration polarization. Concentration polarization on the anode side is accounted for by introducing a second pressure dependent term within the Nernst potential calculation shown in Equation (3.20). This accounting is achieved by basing the pressure dependent term on the average partial pressures at the anode-electrolyte interface, as calculated by the preceding anode partial pressure model. More in depth accounting for anodic concentration polarization could be achieved in future work by expanding this calculation to obtain pressure values and Nernst potentials at each point along the anode-electrolyte interface. The anode-electrolyte voltage can then be obtained by substituting Equation (3.21) into Equation (3.19) and solving for $\overline{V}_{an-elec}$. The complete anode-electrolyte interfacial voltage calculation is summarized in Equation (3.22).

$$\begin{aligned} V_{cell} &= V_{cath,lead} - V_{an,lead} \\ &= E_o - i''\,ASR_{total} - a_{act} - b_{act}\ln i'' + \frac{R_u T}{4F}\ln\left[1 - \frac{i''}{i''_{cs}}\right] \end{aligned} \tag{3.19}$$

$$E_o = -\frac{\Delta G}{2F} + \frac{R_u T}{2F}\ln\left[\frac{\overline{p}_{H_2,an-elec}}{\overline{p}_{H_2O,an-elec}}\right] \tag{3.20}$$

$$V_{an,lead} = \overline{V}_{an-elec} + i''\,ASR_{an} \tag{3.21}$$

$$\overline{V}_{an-elec} = 1 - \left\{E_o - i''\,ASR_{cath,elec} - a_{act} - b_{act}\ln i'' + \frac{R_u T}{4F}\ln\left[1 - \frac{i''}{i''_{cs}}\right]\right\} \tag{3.22}$$

The Nernst potential is established as a temperature dependent parameter using techniques outlined by Khaleel et al. [15]. Specifically, ΔG for the cell reaction shown in Equation (3.23) is defined as

$$\mathrm{H_2} + \tfrac{1}{2}\mathrm{O_2} \rightarrow \mathrm{H_2O} \tag{3.23}$$

$$\Delta G(T, p_0) = G_{H2O}(T, p_0) - G_{H2}(T, p_0) - \tfrac{1}{2} G_{O2}(T, p_0) \tag{3.24}$$

The temperature dependency of Equation (3.24) is established through the quadratic approximation of the temperature dependence of specific heat for each species. This approximation is valid from 273 to 1500 K [26] and thus covers the operational range for a solid oxide fuel cell. The Gibbs free energy for each of the species can be found using the appropriate experimentally determined constants: a_i, b_i, and c_i [26].

$$\begin{aligned} G_i(T, p_0) = G_i^0 + a_i(T - T_0) + \frac{b_i}{2}\left(T^2 - T_0^2\right) + \frac{c_i}{3}\left(T^3 - T_0^3\right) \\ - \left[TS_i(T, p_0) - T_0 S_i(T_0, p_0)\right] \end{aligned} \tag{3.25}$$

Here the subscript i denotes an individual species. The entropy at a given temperature can be found using Equation (3.26). It is important to note that the present definition of the Gibbs free energy treats the oxidant stream as pure oxygen. This simplifying assumption is currently allowed because of the reduced emphasis on cathodic transport phenomena.

$$S_i(T, p_0) = S_i(T_0, p_0) + a_i \ln\left(\frac{T}{T_0}\right) + b_i(T - T_0) + \frac{c_i}{2}\left(T^2 - T_0^2\right) \tag{3.26}$$

The ohmic resistance of the cathode and electrolyte component layers is taken from values provided by Zhao and Virkar [5]. The third and fourth terms in Equation (3.19) represent the activation polarization as calculated via the Tafel Equation [6]. The constants a_{act} and b_{act} are defined in Equation (3.27) below, with the exchange current

density i_o and charge transfer coefficient α taken from available literature [27]. The final term represents the cathodic concentration polarization. Where i''_{cs} is the limiting current density for the cathode as defined by Kim, et al. [6].

$$a_{act} = -\frac{R_u T}{4\alpha F}\ln i_o; \quad b_{act} = \frac{R_u T}{4\alpha F} \tag{3.27}$$

3.1.4 Anode Partial Pressure Distribution

Initial studies of the solutions obtained for the potential flow problems defined in Equations (3.6)-(3.9) and (3.13)-(3.16) were performed for a nominal unit cell geometry of width 2.0 mm and anode thickness of 750 μm. A current density of 1.0 A/cm^2 was applied at a cell temperature of 800 °C (1073 K), and a binary mixture of 89% hydrogen and 11% steam was used to model the fuel stream.

The partial pressure distributions for the button-cell and actual interconnect geometry cases are compared in Figures 3.3 and 3.4. The influence of interconnect geometry is readily discernible in each case. The hydrogen partial pressure at the anode-electrolyte interface is reduced by approximately 5% when accounting for interconnect geometry. Correspondingly, the steam partial pressure at the anode-electrolyte interface shows a subsequent increase.

As previously mentioned the sum of the hydrogen and steam partial pressures at a given point within the anode should equal the total pressure of hydrogen and steam within the fuel stream. Subsequent checks of the partial pressure distributions within the anode, as shown in Figures 3.3 and 3.4, have revealed that the sum of the hydrogen and steam partial pressures throughout the anode is one atmosphere. This condition was also found to be true for the other geometries analyzed in the present work.

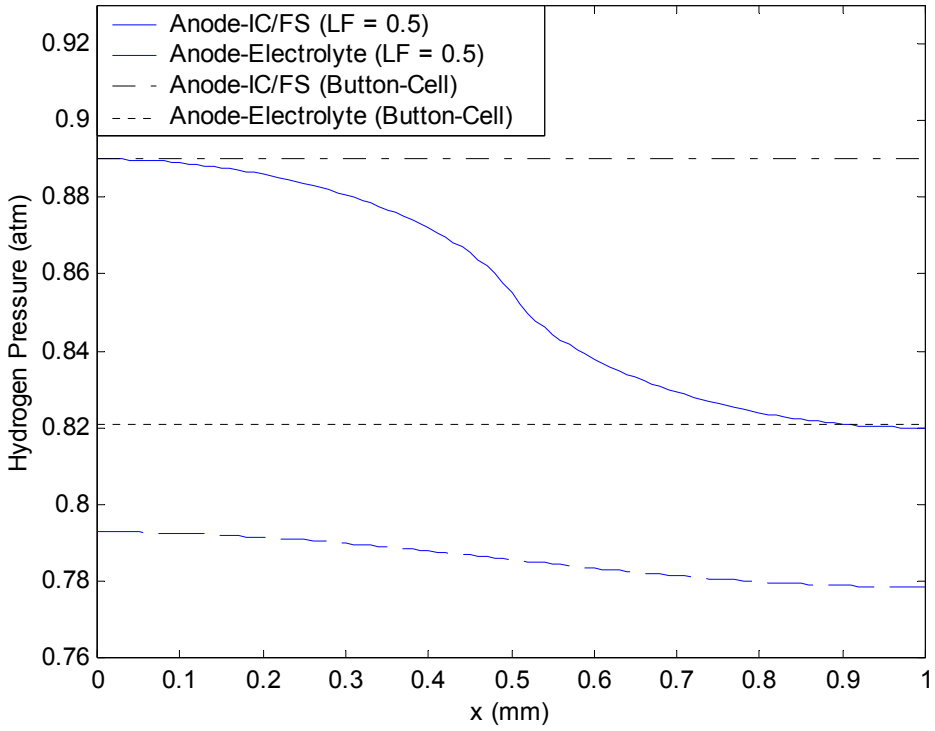

Figure 3.3. Hydrogen partial pressures for button-cell and actual cell geometries

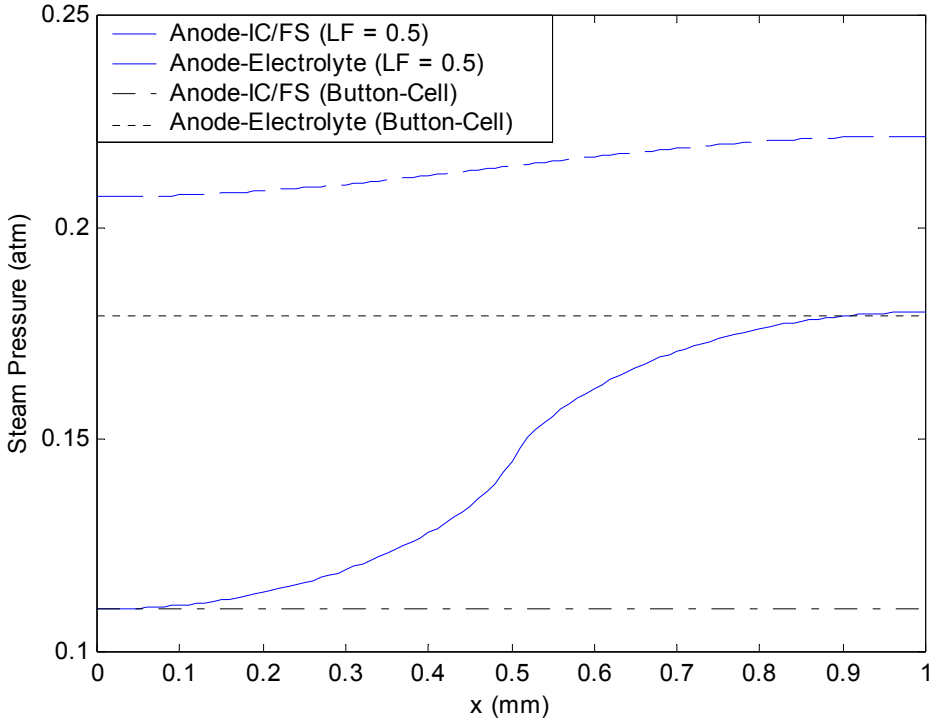

Figure 3.4. Steam partial pressures for button-cell and actual cell geometries

The effects of length fraction on hydrogen transport within the anode are summarized in Table 3.2. The values in the last row represent the button-cell case for mass transport (ideal fuel stream contact). The partial pressure drop was calculated as the difference between the fuel stream hydrogen partial pressure, set at 89% (or 0.89 atm) per the prescribed fuel stream pressure and composition, and the average anode-electrolyte interfacial partial pressure. This average was calculated from values obtained using Equation (3.10). Overall, a decrease in length fraction results in an increase in resistance to the transport of hydrogen. It can be seen that the geometry effects are significant with the fractional pressure drop, $\Delta P/P$, increasing approximately 50% when accounting for the nominal interconnect geometry. The effects of length fraction for several anode thicknesses are given in Figure 3.5. In each case shown in Figure 3.5 the current density was maintained at 1.0 A/cm^2, and the fuel stream hydrogen partial pressure was set at 0.89 atm. Resistance increases with anode thickness, and thinner anode geometries show an increased sensitivity to changes in length fraction. The former trend regarding anode thickness is intuitive for a fixed unit cell width (2.0 mm in the present case), while the increased sensitivity of thin anodes can be attributed to the heightened impact of in-plane, or "sheet," resistance given smaller transverse resistances of thin anodes.

An alternate means of describing the resistance to hydrogen mass transport is through a proposed diffusion mass transport area specific resistance, ASR_{diff,H_2}, which has been defined similarly to the diffusion mass transport resistance [25]. This parameter experiences the same length fraction effects as the fractional pressure drop.

$$ASR_{diff,H_2} = \frac{C_{H_2,an-FS} - \overline{C}_{H_2,an-elec}}{J''_{H_2,an-elec}} \tag{3.28}$$

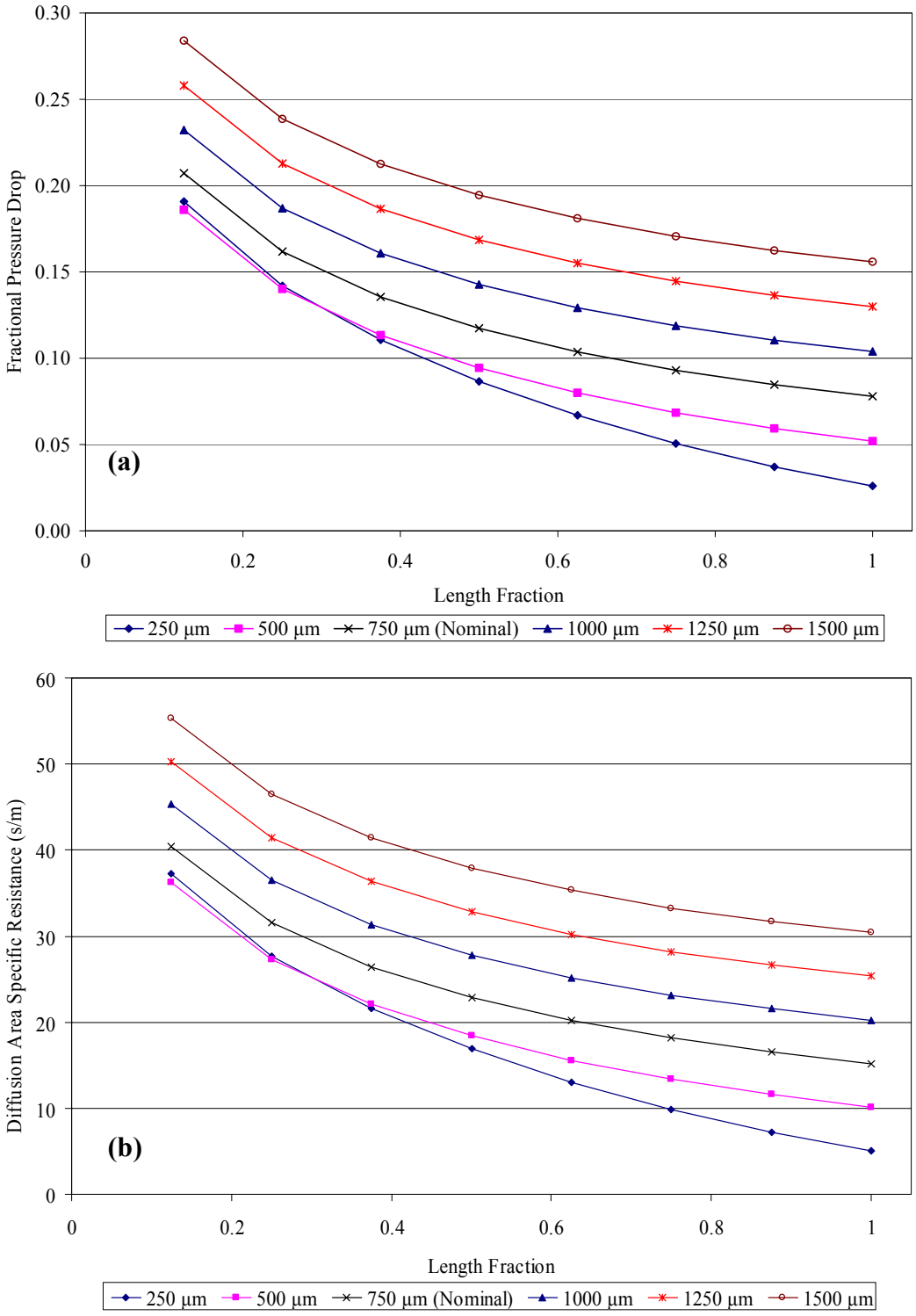

Figure 3.5. Variation of (a) fractional pressure drop and (b) mass transfer diffusional ASR with length fraction for several anode thicknesses (hydrogen transport)

Table 3.2. Length fraction dependence for several hydrogen transport metrics

Length Fraction	Partial Pressure Drop (atm)	ΔP/P	$ASR_{m,diff}$ (s/m)
0	----	----	----
0.125	0.184	0.207	40.41
0.25	0.144	0.162	31.55
0.375	0.121	0.136	26.43
0.5	0.104	0.117	22.88
0.625	0.092	0.104	20.22
0.75	0.083	0.093	18.14
0.875	0.075	0.085	16.50
1	0.069	0.078	15.20

The case of a 250 μm thick anode demonstrates an increase in sensitivity to changes in length fraction. This increase is evident in the intersection of the curves of both fractional pressure drop and mass transfer diffusional ASR for the 250 and 500 μm cases. The increased sensitivity to changes in length fraction is made more evident when analyzing the derivative of the fractional pressure drop with respect to length fraction. As shown in Figure 3.6, across the range of length fractions analyzed, the derivative of the fractional pressure drop for a thickness of 250 μm shows a marked change from all other thickness values. For a thickness of 500 μm, the change in this value is slight in comparison. The increased sensitivity to length fraction can be attributed to an increased influence of "sheet" resistance within the anode. For the case of a 250 μm thick anode, the width of the interconnect rib is greater than or equal to the anode thickness for six of the eight length fraction values studied. The exceptions are the length fraction values of 0.875 and 1.0. This fact is demonstrated in Figure 3.7, with the ratio of anode thickness to interconnect rib width defined in Equation (29).

$$\frac{\text{Anode Thickness}}{\text{Interconnect Rib Width}} = \frac{t_{an}}{a\left(1 - LF\right)} \tag{3.29}$$

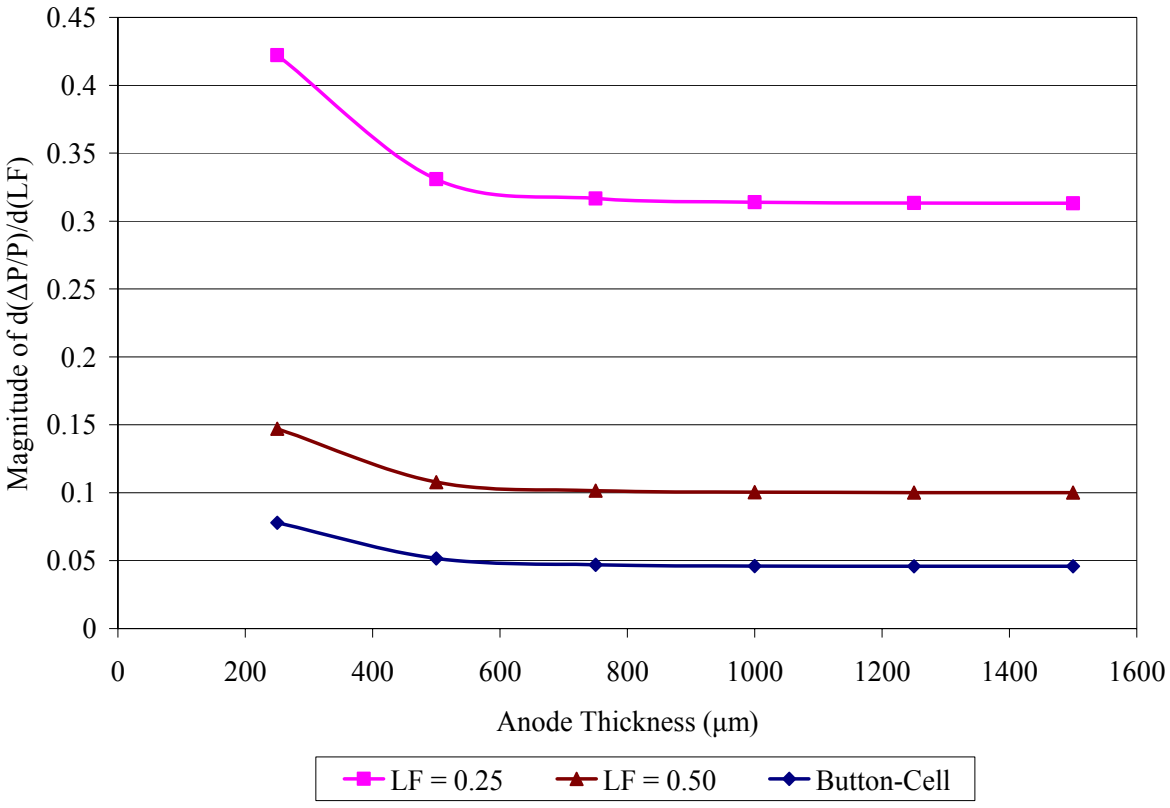

Figure 3.6. Derivative of the fractional pressure drop with respect length fraction as a function of anode thickness (shown for LF = 0.25, 0.5, and 1)

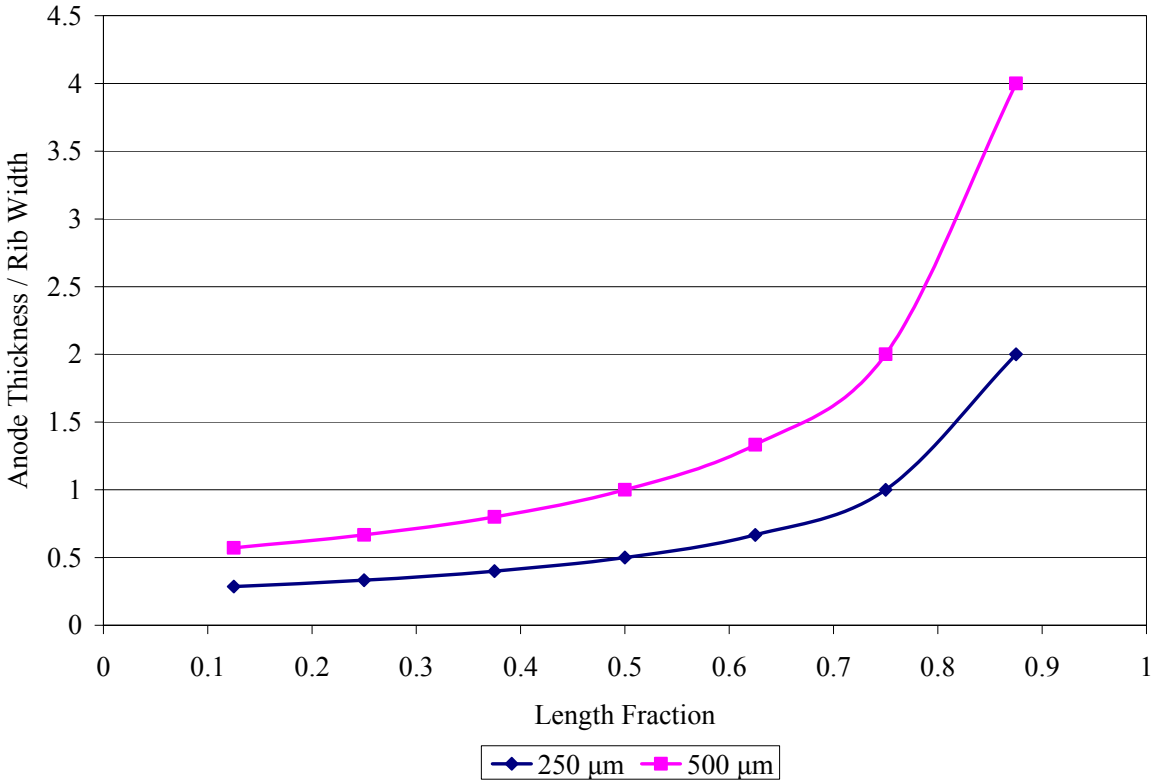

Figure 3.7. Ratio of anode thickness to interconnect rib width as function of length fraction (shown for t_{an} = 250 µm, 500 µm)

3.1.5 Anode Voltage Distribution

The anode voltage distribution for both the button-cell and interconnect geometry cases are compared in Figure 3.8. As in the mass transport case, significant geometry effects can be seen. It is important to note that electrical contact only occurs between 0.5 and 1.0 mm for the nominal geometry (LF = 0.50). Thus a higher voltage drop occurs across the anode when accounting for geometry effects. Furthermore, an increased anode lead voltage results from accounting for cell geometry. This increase will ultimately result in a decreased total cell voltage as defined in Equation (3.19).

Length fraction effects on anode electronic transport are summarized in Table 3.3. The values in the first row represent ideal, uniform electrical contact. The voltage drop in the electronic transport case was calculated as the difference between the average voltage along the anode-interconnect contact surface and the average anode-electrolyte voltage. Both averages were calculated from voltage values obtained with Equation (3.17). The anode area specific resistance was calculated using Equation (3.30).

$$ASR = \frac{\Delta V_{an}}{i''_{an-elec}} = \frac{\overline{V}_{an-IC} - \overline{V}_{an-elec}}{i''_{an-elec}} \tag{3.30}$$

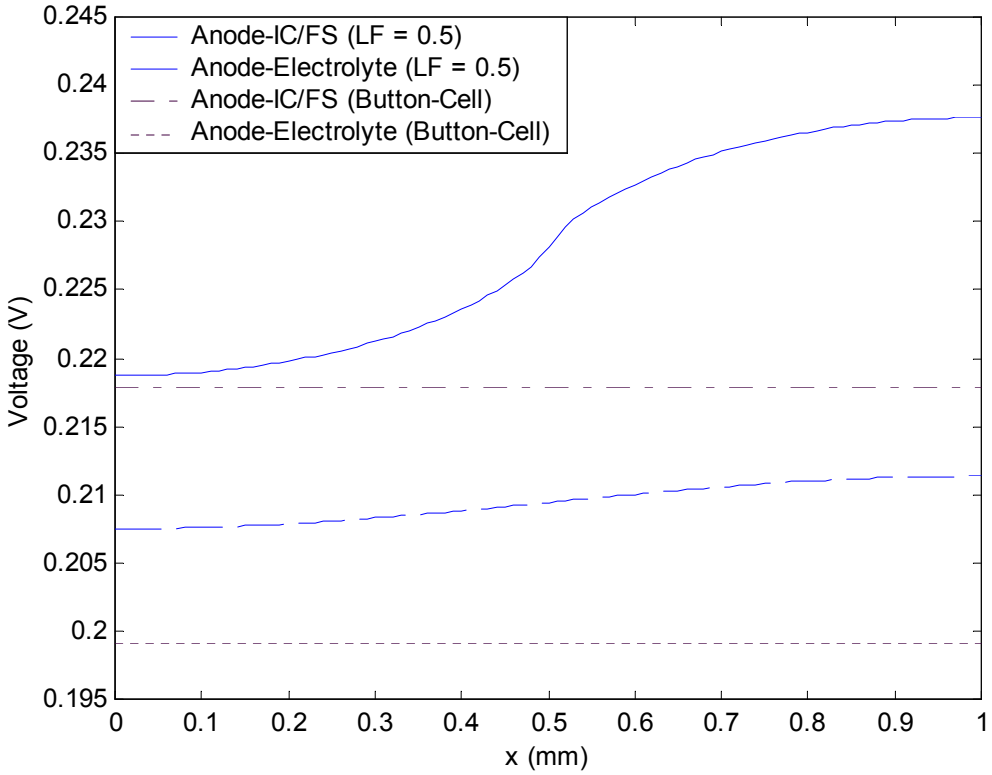

Figure 3.8. Comparison of anodic voltage distributions for button-cell and actual cell geometries

The effect of actual cell geometry on anode and cell area specific resistance can be seen in Figure 3.9, with the anode area specific resistance for the nominal case increasing by ~36% when accounting for actual interconnect geometry. The anode area specific resistance is also shown to increase with length fraction. The variation of geometry effects on anode and cell ASR is illustrated for several anode thicknesses in Figure 3.9. As in the hydrogen transport case, total resistance increases with anode thickness and demonstrates an increased sensitivity to length fraction for thinner anodes.

The values for anode and cell area specific resistances, calculated using potential flow theory, are in close agreement with values calculated from experimental models [5]. The results of Zhao and Virkar demonstrate an anode resistivity of 0.24 Ω-cm. Applying potential flow theory to the button-cell case predicts an effective anode resistivity of 0.25 Ω-cm. This agreement is further demonstrated in Figure 3.10. The increased anode resistance effects for actual interconnect geometry were extended to the total cell area specific resistance by adding 0.084 Ω-cm^2 to the anode area specific resistance values. This value represents the combined resistance of the remaining cell component layers as given in Zhao and Virkar [5]. The cell total resistance increases by ~7% when accounting for the nominal interconnect geometry.

Table 3.3. Length fraction dependence for several electronic transport metrics

Length Fraction	ΔV_{an} (V)	Anode ASR (Ω-cm^2)	Cell ASR (Ω-cm^2)
0	0.0188	0.0188	0.1028
0.125	0.0193	0.0193	0.1033
0.25	0.0206	0.0206	0.1046
0.375	0.0226	0.0226	0.1066
0.5	0.0256	0.0256	0.1096
0.625	0.0298	0.0298	0.1138
0.75	0.0358	0.0358	0.1198
0.875	0.0469	0.0469	0.1309
1	----	----	----

As seen in Tables 3.2 and 3.3 and Figures 3.5 and 3.9, a larger fuel stream contact area, represented by increasing length fraction, decreases mass transfer resistance and increases electronic resistance. Similarly, decreasing fuel stream contact reduces electronic resistance while increasing mass transfer resistance. Overall, the resistance to mass transfer displays a greater sensitivity to changes in interconnect geometry. Thus, mass transfer resistance effects limit anode transport phenomena more so than electronic resistance effects. The optimization of interconnect geometry based on these resistance effects will be of key importance in future SOFC designs.

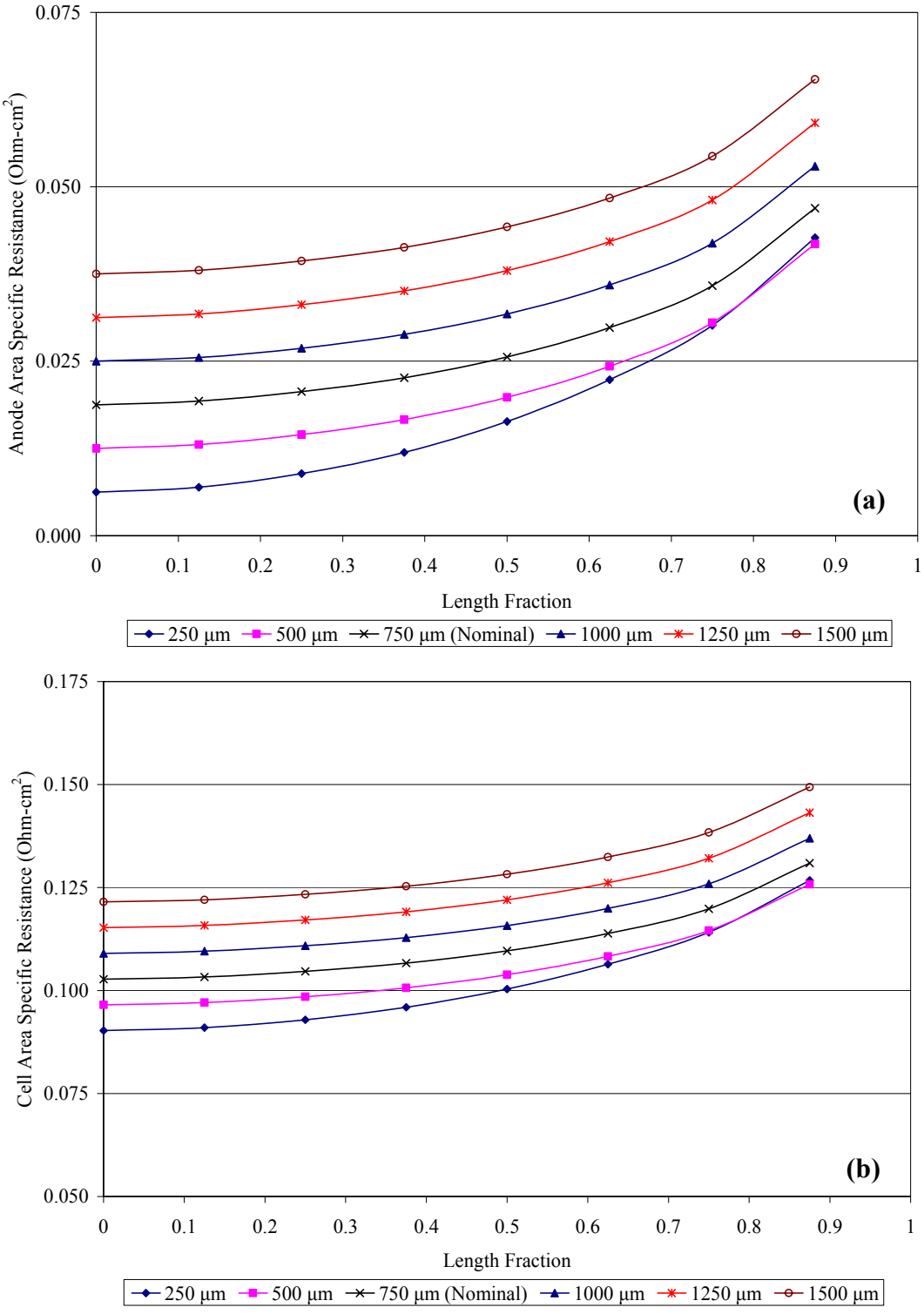

Figure 3.9. Variation of (a) anode ASR and (b) cell total ASR with length fraction for several anode thicknesses.

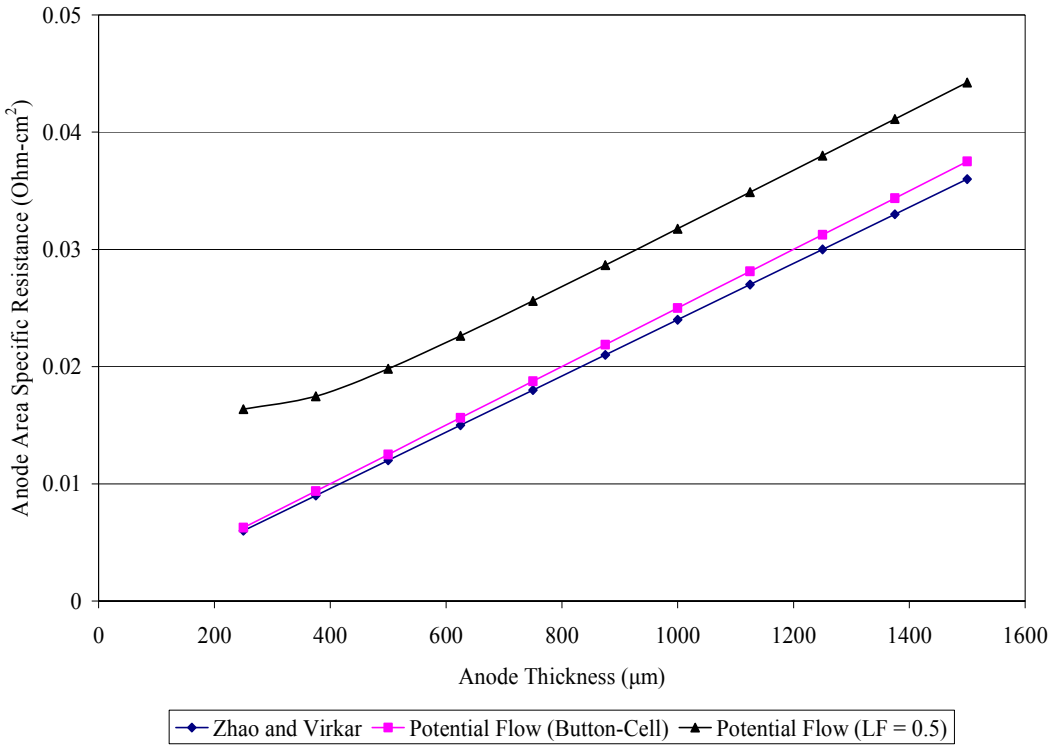

Figure 3.10. Variation of anode ASR with anode thickness as predicted from potential flow theory and existing experimental models [5]

3.2 Numerical Corroboration of Pressure Model

In the absence of internal species generation and mass average velocity effects, steady-state mass transport can be described via potential flow theory. Similarly, steady-state heat transfer in the absence of internal heat generation can be modeled as a potential flow phenomenon. As these two types of transport phenomena are described by the Laplace equation, an analogy between the two types can be established.

$$k\left(\frac{\partial^2 T}{\partial x^2}+\frac{\partial^2 T}{\partial y^2}\right)=0 \tag{3.31}$$

$$\frac{D_{H2-H2O}}{R_u T}\frac{\varepsilon}{\tau}\left(\frac{\partial^2 p_{H2}}{\partial x^2}+\frac{\partial^2 p_{H2}}{\partial y^2}\right)=0 \tag{3.32}$$

Equation (3.31) treats heat flux with units of W/m^2, and Equation 3.32 treats molar flux in $mol/m^2 \cdot s$. While the constant terms outside of the parentheses are typically removed as well, they are retained in the above equations for instructive purposes. Many available finite element analysis programs offer the capability to perform basic heat transfer analyses, but these same programs do not offer mass transfer analyses in their base packages. However, base level finite element analysis (FEA) can be performed using the above thermal analogy by defining hydrogen partial pressure in kPa as the analog for the absolute temperature in Kelvin. An analogous thermal conductivity for the medium can also be defined using the constant term from Equation (3.32).

$$k_{\text{analog}} = \frac{D_{H2-H2O}}{R_u T}\frac{\varepsilon}{\tau} \quad [\text{m}^2 \cdot \text{mol/kJ} \cdot \text{s}] \tag{3.33}$$

The problem defined in Equations (3.6)-(3.9) and illustrated in Figure 3.2 can then be established in an FEA program for the anode geometry using the same boundary conditions: a continuous Neumann boundary condition at the anode-electrolyte interface and at the left and right symmetry bounds of the unit cell; and a composite Neumann boundary condition at the anode-interconnect/fuel stream interface. An additional pressure constraint is required to obtain a numerical solution. This pressure constraint performs the same role as the first constant term in Equation (3.10) by establishing a necessary reference pressure for use in computation. This constraint is defined by setting the hydrogen partial pressure at the center of the anode-fuel stream interface, $p_{H2}(0, t_{an})$, equal to the fuel stream hydrogen partial pressure.

The nominal geometry used in the initial analyses of the anode partial pressure and voltage distributions was established in the finite element program ANSYS (ANSYS, Inc.). As previously established, this geometry has a unit cell width of 2.0 mm and anode thickness of 750 μm. The above boundary conditions and constraints were applied along with a current density of 1.0 A/cm^2 and a cell temperature of 800 °C (1073 K). The partial pressure of hydrogen in the fuel stream was specified as 0.89 atm (i.e., 90.179 kPa, which is analogous to an absolute temperature of 90.179 K). The molar fluxes of hydrogen across the anode-electrolyte and anode-fuel stream interfaces, which are analogous to the heat flux in W/m^2, are defined from the current density using Equations (3.34) and (3.35)**,** respectively. As hydrogen is consumed at the anode-electrolyte interface, the negative sign in Equation (3.34) is used exclusively within the ANSYS environment to indicate hydrogen flux out of the anode.

$$J''_{H2,an-elec} = -\frac{i''}{2F} \tag{3.34}$$

$$J''_{H2,an-FS} = \frac{a}{b}\frac{i''}{2F} \tag{3.35}$$

The results of the ANSYS model for the nominal geometry with a length fraction of 0.5 are shown in Figure 3.11. The strong agreement between the analytic and numerical models is evident. Subsequent error analysis was conducted for multiple geometry cases. These cases are shown in Table 3.4. The geometries tested were for anode thicknesses from 250-1500 μm. The extreme values of length fraction (0.125 and 0.875) were examined in addition to the nominal value of 0.5. For all cases the

maximum relative error between the FEA and analytic model was substantially less than 0.1%.

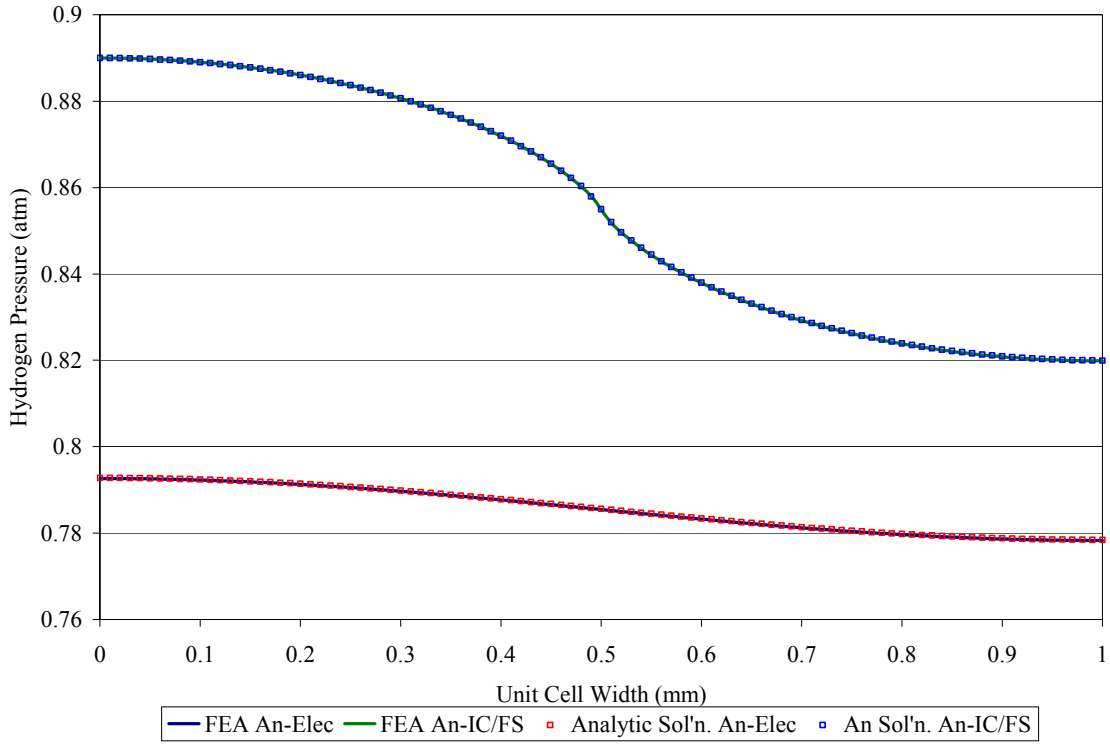

Figure 3.11. Comparison of FEA and analytic solution for the nominal geometry with a length fraction (LF) of 0.5

Table 3.4. FEA verification cases for the analytic partial pressure model

Anode Thickness (μm)	IC Contact (mm)	FS Contact (mm)	Length Fraction	Maximum % Error
250	1.75	0.25	0.125	0.06
	1	1	0.5	0.02
	0.25	1.75	0.875	0.02
500	1.75	0.25	0.125	0.05
	1	1	0.5	0.05
	0.25	1.75	0.875	0.02
750	1.75	0.25	0.125	0.05
	1	1	0.5	0.02
	0.25	1.75	0.875	0.02
1000	1.75	0.25	0.125	0.06
	1	1	0.5	0.02
	0.25	1.75	0.875	0.02
1500	1.75	0.25	0.125	0.07
	1	1	0.5	0.03
	0.25	1.75	0.875	0.03

3.3 A Modified Concept of Limiting Current Density

The current drawn from a SOFC is ultimately limited by mass transfer within the electrode layers. For a given fuel stream partial pressure, a large enough current will cause hydrogen to be consumed at the anode-electrolyte interface faster than it can be supplied. This scenario is referred to as fuel depletion and leads to fuel starvation, or the complete absence of fuel at the anode-electrolyte interface. Within actual SOFC geometries, fuel depletion can occur along discrete sections of the anode-electrolyte interface, with other sections remaining operational. In such cases redox reactions at the anode-electrolyte interface can have deleterious effects on SOFC performance and reliability. In common SOFC designs the issue of fuel starvation, which occurs at the limiting current density, is treated as being synonymous with the onset of fuel depletion.

However, if the effects of interconnect geometry are accounted for, this is not the case. Thus, a distinction must be made between the limiting current density, and what is hereafter referred to as the fuel depletion current density.

The beginning of fuel depletion at the anode-electrolyte interface coincides with the hydrogen partial pressure at the lower right-hand corner of the anode domain being zero (Figure 3.12). The fuel depletion current density can be found by solving for the current density when the condition in Equation (3.36) is satisfied.

$$p_{H_2}(a,0) = p_{H_2,an-FS} - A_0 t_{an} - \sum_{n=1}^{\infty} A_n \left[\cosh(\lambda_n t_{an}) - \cos(\lambda_n a)\right] = 0 \tag{3.36}$$

$$p_{H_2,an-FS} = \frac{R_u T}{2FD_{H2-H2O}} \frac{\tau}{\varepsilon} i'' \left\{ t_{an} + \sum_{n=1}^{\infty} B_n \left[\cosh(\lambda_n t_{an}) - \cos n\pi\right] \right\} \tag{3.37}$$

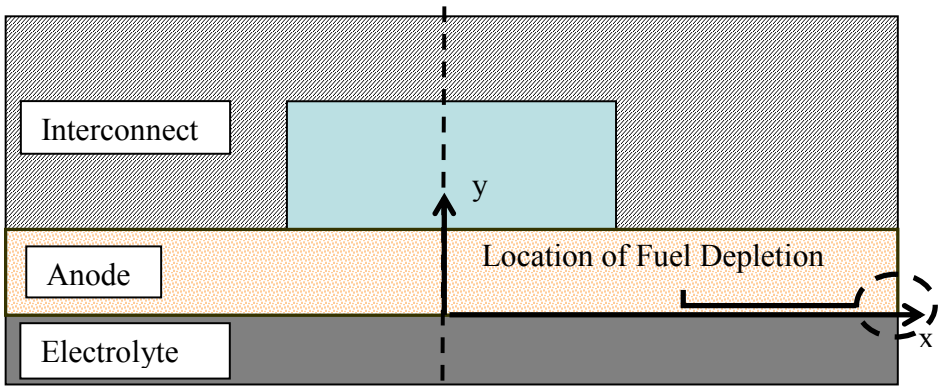

Figure 3.12. Region of concern for fuel depletion initiation

This process yields the fuel depletion current density, i''_{FD}.

$$i''_{FD} = \frac{2FD_{H2-H2O}}{R_u T} \frac{\varepsilon}{\tau} \frac{p_{H_2,an-FS}}{t_{an} + \sum_{n=1}^{\infty} B_n \left[\cosh(\lambda_n t_{an}) - \cos n\pi\right]} \tag{3.38}$$

$$B_n = \frac{A_n}{A_0} = \frac{2\sin(\lambda_n b)}{n\pi\lambda_n \sinh(\lambda_n t_{an})}\left(\frac{a}{b}\right) \tag{3.39}$$

This definition can be compared to the definition of limiting current density provided in [6]. For an anode supported cell the limiting current density is defined as follows.

$$i''_{FD} = i''_{\lim} = \frac{2FD_{H2-H2O}}{R_u T}\frac{\varepsilon}{\tau}\frac{p_{H_2,an-FS}}{t_{an}} \tag{3.40}$$

This definition is taken from Kim, et al. [6]. However, it is also a standard definition of limiting current density. If the button-cell approximation is applied (i.e., $b = a$), the constant B_n defined in Equation (3.39) is zero. That is,

$$B_n = \left[\frac{2\sin(\lambda_n a)}{n\pi\lambda_n \sinh(\lambda_n t_{an})}\left(\frac{a}{b}\right)\right], \quad \lambda_n = \frac{n\pi}{a}, \text{ and } \sin\left(\frac{n\pi}{a}a\right) = \sin(n\pi) = 0$$
$$\therefore \quad B_n = 0$$

In this case, the fuel depletion current density defined by the potential flow approach then reduces to the more commonly used concept of limiting current density that is defined in Equation (3.40).

The ramifications of a fuel depletion current density are particularly important when considering the effects of interconnect geometry. This fact is demonstrated in Figure 3.13. Under the button-cell approximation, the fuel depletion current density corresponds to the established definition of limiting current density, and is predicted to increase significantly as the anode becomes thinner. However, when interconnect

geometry is accounted for (as shown for a length fraction of 0.50) the fuel depletion current density decreases after the thickness decreases below 500 μm. The cases shown are for a unit cell width of 2.0 mm. The decrease in the fuel depletion current density in the case with LF = 0.50 can be attributed to the dominance of sheet resistance effects over the total anodic resistance to mass transfer. For excessively thin anodes, this shift to sheet resistance effects limiting mass transfer can become a significant performance issue.

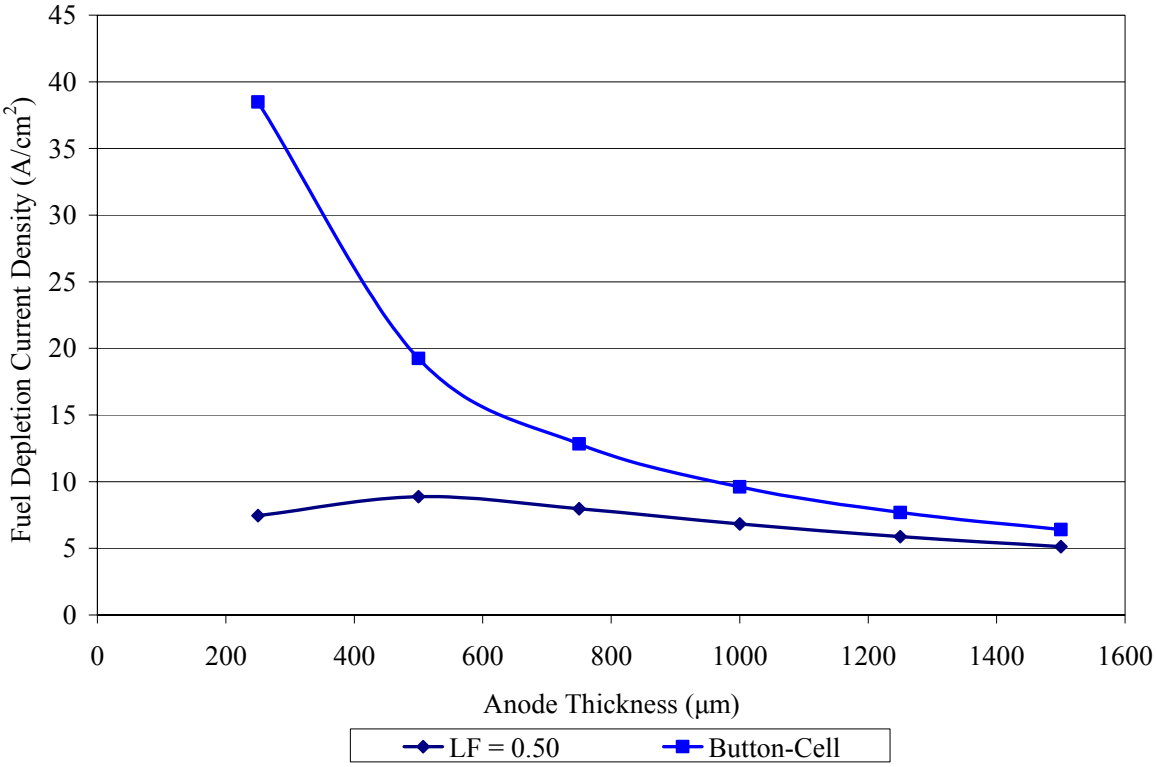

Figure 3.13. Effects of interconnect geometry on fuel depletion current density

CHAPTER 4

SOFC MODELING APPLICATIONS

In the preceding chapter the effects of SOFC interconnect geometry were established through analytic solutions of potential flow problems that describe anodic mass and electronic transport phenomena. The solutions obtained allow for greater insight into the effects of actual SOFC geometry in comparison to the common button-cell assumption. Specifically, significant effects on mass transfer and electronic resistance were demonstrated when accounting for actual interconnect geometry. These effects tend to be more pronounced with respect to mass transfer resistance. However, resistance to electronic transport experiences an increase of similar magnitude, thus creating a competition between mass transfer and electronic resistance effects. For a representative interconnect geometry of 2.0 mm total (unit cell) width and an equal division of fuel stream and interconnect contact area (i.e., length fraction of 0.50) resistances were found to be ~50% higher for hydrogen transport and ~36% higher for electronic transport. The minimization of such resistance effects through the proper sizing of the fuel stream-anode and anode-interconnect contact areas could play a significant role in the development of SOFC power generation technologies. For mass and electronic transport cases this minimization could be achieved by increasing the respective contact areas. However, fundamental interconnect design creates a competition between the mass transfer and electronic resistance effects. For example, increasing interconnect electrical contact area will reduce ohmic resistance, but it will also increase fractional pressure drop across the anode and reduce the operational fuel

depletion current density. This competition creates an optimization problem that will be initially explored in the present chapter through parametric studies constructed using a design of experiments (DOE) approach. The present studies focus on the effects of two-dimensional transport within the unit cell cross-section, as defined in the previous chapter, and serve as an initial exploration of optimum SOFC geometry. Future analyses will require consideration of the effects of fuel channel sizing on the pressure distribution along the length of the fuel channel.

In addition to the direct effects SOFC interconnect geometry has on mass and electronic transport phenomena, the compounded effects of fuel stream concentration and cell current loading are considered. For the mass transport cases resistances were studied for a fuel stream mixture of 89% hydrogen and 11% steam. In typical reformate fuel streams the concentration of hydrogen is much lower. This lower hydrogen concentration may lead to more pronounced geometry effects on anodic resistance to mass transport. Similarly, the typical SOFC operates under a range of current loading regimes that will affect performance with respect to mass and electronic transport.

Finally, the parametric studies run for SOFC operation are applied to the operation of solid oxide electrolysis cells (SOECs) to determine if interconnect design that benefits SOFC performance is mutually beneficial to SOEC performance. In these studies the potential flow models developed for SOFC anodic transport phenomena are run under reversed current loading, with fuel stream steam concentration treated as the mass transport limiting variable. This reversed arrangement is based upon the operation of SOECs as devices that produce hydrogen from a hydrogen-steam mixture under an applied electrical load.

4.1 Design of Experiments for SOFC Anodic Transport Phenomena

A design of experiments approach was applied to the mass and electronic transport models developed using the commercially available statistical analysis software JMP (SAS Institute). Central composite designs of experiments were established for the primary model outputs of hydrogen fractional pressure drop, fuel depletion current density, anode area specific resistance, and average anode-interconnect voltage (i.e. anode lead voltage). This central composite design (CCD) was achieved by calculating the model output parameters at the minimum, midpoint, and maximum values of the input variables used in the design of experiments studies. These input variables and their corresponding ranges are given in Tables 4.1-4.3. Additionally, random combinations of values within these ranges were introduced to provide a better regression fit to the analytic models developed.

A response surface equation is generated from a quadratic fit to the data generated from the array of model runs for the hydrogen fractional pressure drop, fuel depletion current density, the anode ASR, and anode lead voltage. Subsequent refinement of the models created within JMP demonstrated that better fits to the data were achieved when a logarithmic transformation was performed on the first three output variables. These fits produced higher R^2 values and lower RMS errors than fits attempted for the direct values of the output variables. This increased accuracy is likely due to the presence of hyperbolic functions within the analytic solutions comprising the mass and electronic transport models as well as the fuel depletion current model. The presence of hyperbolic functions within these solutions creates an exponential dependence, specifically with

respect to geometric variables, which can be simplified using a logarithmic transformation of the data. The quality of the fits generated for the output variables is demonstrated in Figures 4.1-4.4. These plots compare the value calculated from the analytic solution to the value predicted by the response surface equation generated within JMP.

Table 4.1. Input variables, and respective ranges, for hydrogen fractional pressure drop Design of Experiments study

Composition (% Hydrogen)	Current Density (A/cm^2)	Unit Cell Width (mm)	Length Fraction	Anode Thickness (μm)	Porosity	Tortuosity
5	0.1	1	0.125	500	0.1	2
50	1	5	0.5	1500	0.3	6
95	2	10	0.875	2500	0.5	10

Table 4.2. Input variables, and respective ranges, for fuel depletion current density Design of Experiments study

Composition (% Hydrogen)	Unit Cell Width (mm)	Length Fraction	Anode Thickness (μm)	Porosity	Tortuosity
5	1	0.125	500	0.1	2
50	5	0.5	1500	0.3	6
95	10	0.875	2500	0.5	10

Table 4.3. Input variables, and respective ranges, for anode area specific resistance and anode lead voltage Design of Experiments study

Composition (% Hydrogen)	Current Density (A/cm^2)	Width (mm)	Length Fraction	Thickness (μm)
5	0.1	1	0.125	500
50	1	5	0.5	1500
95	2	10	0.875	2500

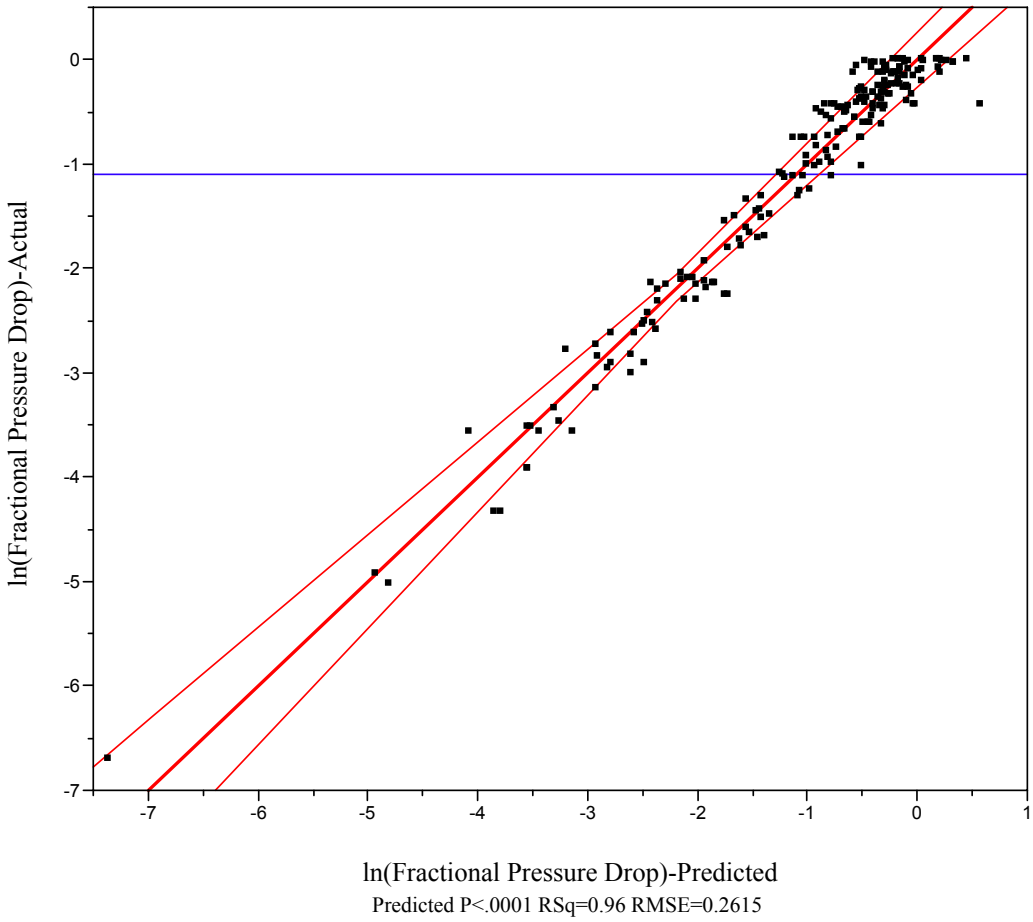

Figure 4.1. Actual response versus predicted response for fractional pressure drop design of experiments (DOE) model

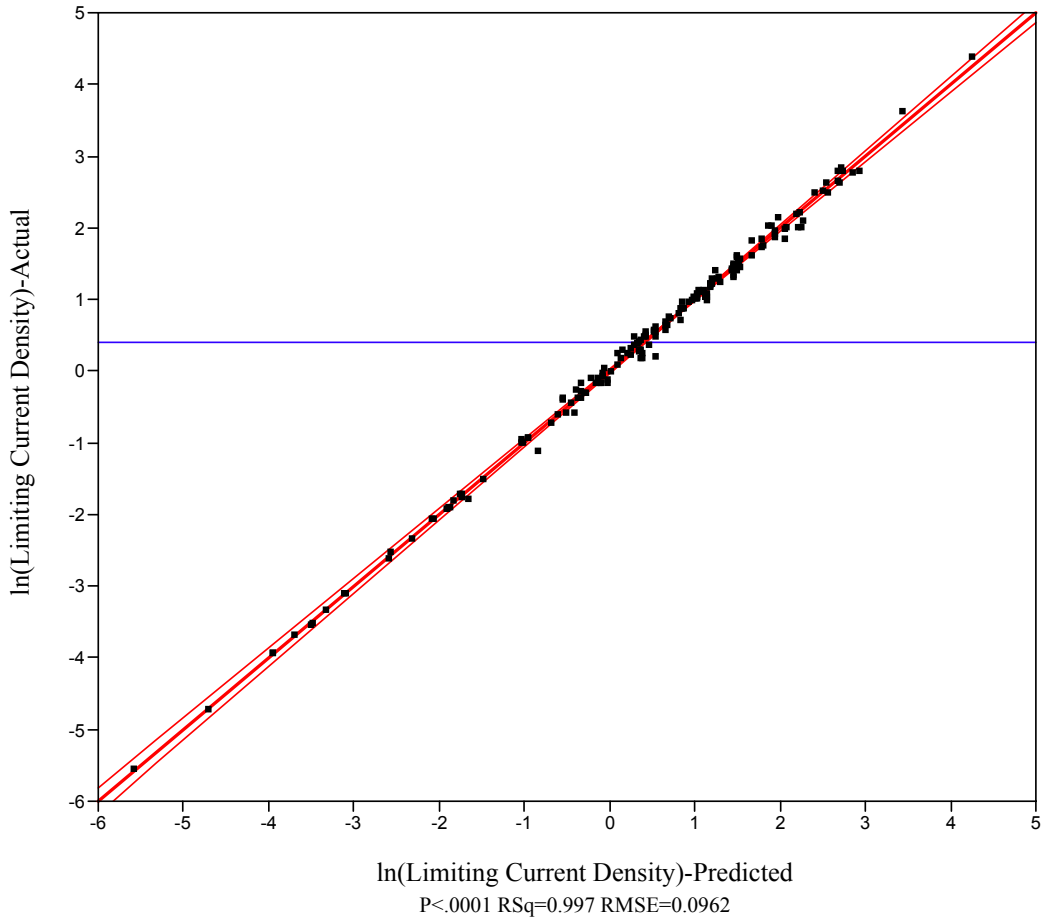

Figure 4.2. Actual response versus predicted response for fuel depletion current density DOE model

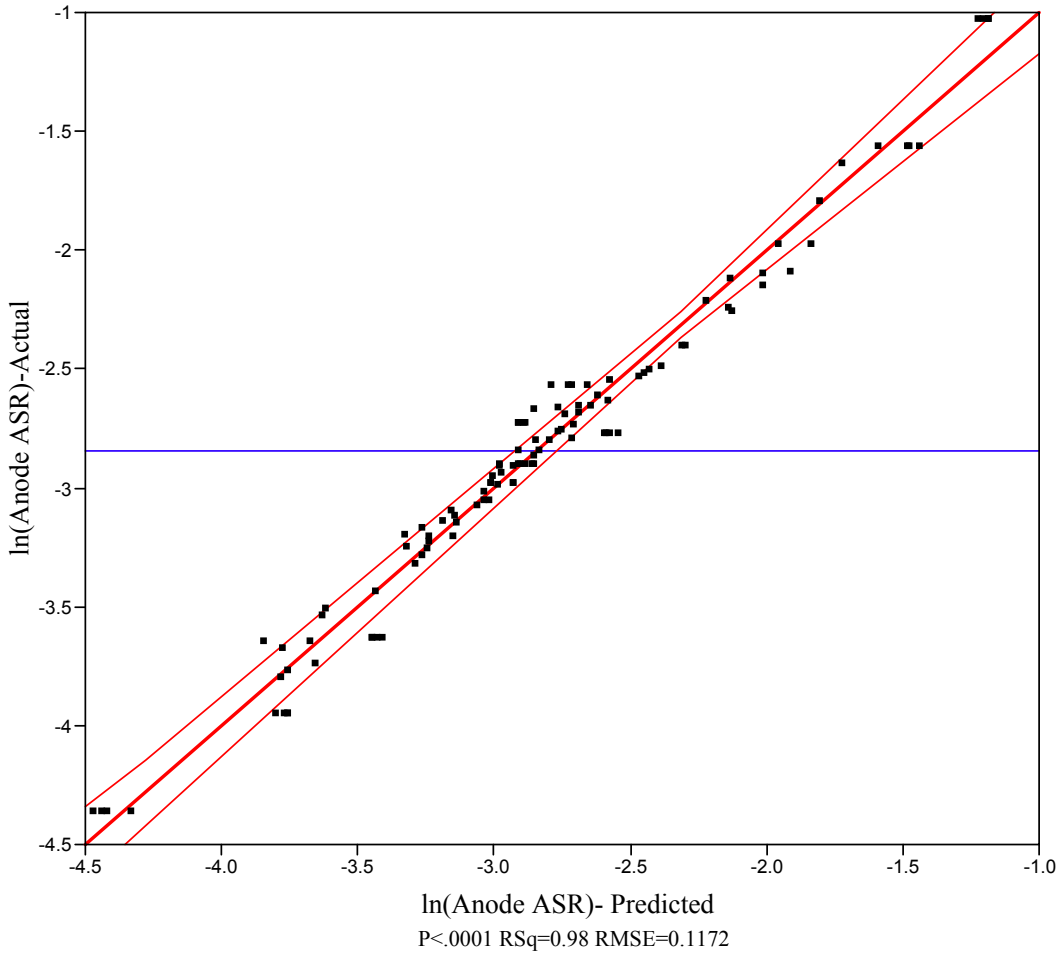

Figure 4.3. Actual response versus predicted response for anode ASR DOE model

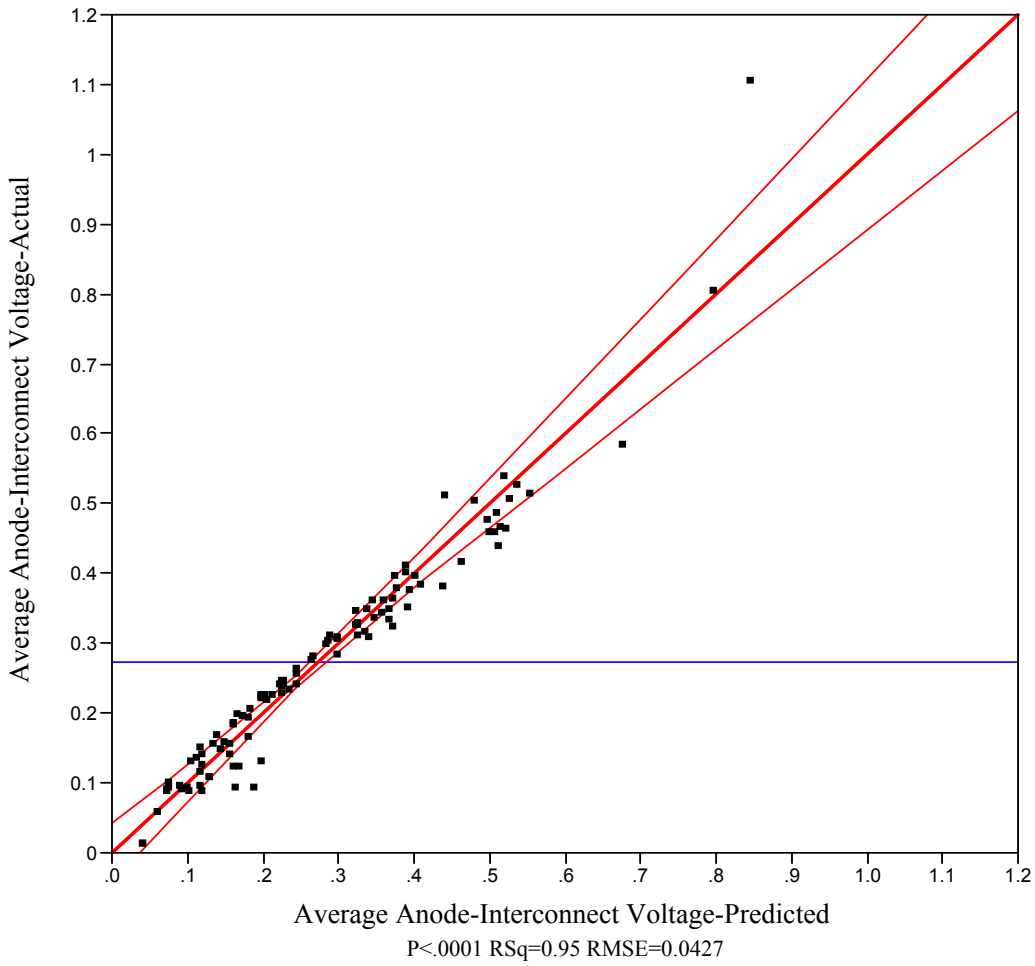

Figure 4.4. Actual response versus predicted response for anode lead voltage DOE model

The influence of the design variables listed in Tables 4.1-4.3 above was determined using Pareto plots generated within JMP along with the fit models. These plots, shown in Figures 4.5-4.8, rank the design variables based upon the effect each design variable has on models' response: fractional pressure drop, fuel depletion current density, anode ASR, or anode lead voltage. These results are used to highlight the variables that affect the cell performance the most. For the mass and electronic transport cases the variables are divided into tiers based upon the DOE results shown in the Pareto plots below. For fractional pressure drop, the anode porosity and tortuosity, the fuel

stream hydrogen composition, and the current density demand exert the primary influence over cell performance. Referring to the previous chapter, these variables establish the characteristics of the hydrogen transport problem. Porosity and tortuosity are used in defining an analogous conductivity for diffusion mass transfer, restated below in Equation (4.1). The fuel stream composition and current density demand establish the hydrogen flux across the anode-electrolyte and anode-fuel stream interface.

$$k_{\text{analog}} = \frac{D_{H2-H2O}}{R_u T}\frac{\varepsilon}{\tau} \tag{4.1}$$

In the case of fuel depletion current density, the fuel stream hydrogen composition exerts the greatest influence with unit cell width, porosity, and tortuosity demonstrating secondary levels of influence. The influence of the fuel stream hydrogen composition and the anode porosity and tortuosity can be seen readily in the revised definition for the fuel depletion current density, restated in Equation (4.2) and (4.3). The increased influence of the unit cell width may seem counterintuitive. However, this higher level influence can be linked to the presence of the unit cell half-width, a, within the eigenvalues, λ_n, shown in Equation (4.4).

$$i''_{FD} = \frac{2FD_{H2-H2O}}{R_u T}\frac{\varepsilon}{\tau}\frac{p_{H_2,an-FS}}{t_{an} + \sum_{n=1}^{\infty} B_n\left[\cosh(\lambda_n t_{an}) - \cos n\pi\right]} \tag{4.2}$$

$$B_n = \frac{A_n}{A_0} = \frac{2\sin(\lambda_n b)}{n\pi\lambda_n \sinh(\lambda_n t_{an})}\left(\frac{a}{b}\right) \tag{4.3}$$

$$\lambda_n = \frac{n\pi}{a} \tag{4.4}$$

The designs of experiments for both fractional pressure drop and fuel depletion current density suggest that composition and current density demand exert primary influences on SOFC mass transport phenomena. Therefore parametric studies focusing upon the influence of these variables have been conducted. SOFC geometry, specifically with respect to unit cell width and length fraction, has been factored into these studies via representative values.

Term	Orthog Estimate
Porosity	-0.5157761
Current Density	0.4810783
Composition	-0.4739411
Tortuosity	0.4722654
(Current Density-0.67164)*(Current Density-0.67164)	-0.3387373
UC Width	0.3003519
Length Fraction	-0.2977190
Anode Thickness	0.2364499
(UC Width-5.46826)*(Anode Thickness-1466.79)	-0.1420961
(UC Width-5.46826)*(Length Fraction-0.49509)	-0.1050010
(Composition-52.4329)*(UC Width-5.46826)	0.0999690
(Length Fraction-0.49509)*(Anode Thickness-1466.79)	0.0927796
(Composition-52.4329)*(Porosity-0.29861)	-0.0898795
(Composition-52.4329)*(Tortuosity-6.19789)	0.0858617
(Tortuosity-6.19789)*(Tortuosity-6.19789)	-0.0821398
(Composition-52.4329)*(Length Fraction-0.49509)	-0.0780149
(Porosity-0.29861)*(Tortuosity-6.19789)	0.0718221
(Composition-52.4329)*(Current Density-0.67164)	-0.0637828
(Current Density-0.67164)*(UC Width-5.46826)	-0.0611686
(UC Width-5.46826)*(Porosity-0.29861)	0.0525018
(UC Width-5.46826)*(Tortuosity-6.19789)	-0.0499629
(Current Density-0.67164)*(Length Fraction-0.49509)	0.0493325
(Porosity-0.29861)*(Porosity-0.29861)	0.0472426
(Current Density-0.67164)*(Anode Thickness-1466.79)	0.0424891
(Length Fraction-0.49509)*(Porosity-0.29861)	-0.0311501
(Length Fraction-0.49509)*(Length Fraction-0.49509)	-0.0271587
(Length Fraction-0.49509)*(Tortuosity-6.19789)	0.0242909
(Composition-52.4329)*(Composition-52.4329)	-0.0185006
(Anode Thickness-1466.79)*(Tortuosity-6.19789)	-0.0154760
(Composition-52.4329)*(Anode Thickness-1466.79)	0.0143699
(UC Width-5.46826)*(UC Width-5.46826)	0.0136143
(Current Density-0.67164)*(Porosity-0.29861)	0.0119959
(Anode Thickness-1466.79)*(Porosity-0.29861)	0.0101699
(Current Density-0.67164)*(Tortuosity-6.19789)	-0.0093521
(Anode Thickness-1466.79)*(Anode Thickness-1466.79)	0.0073227

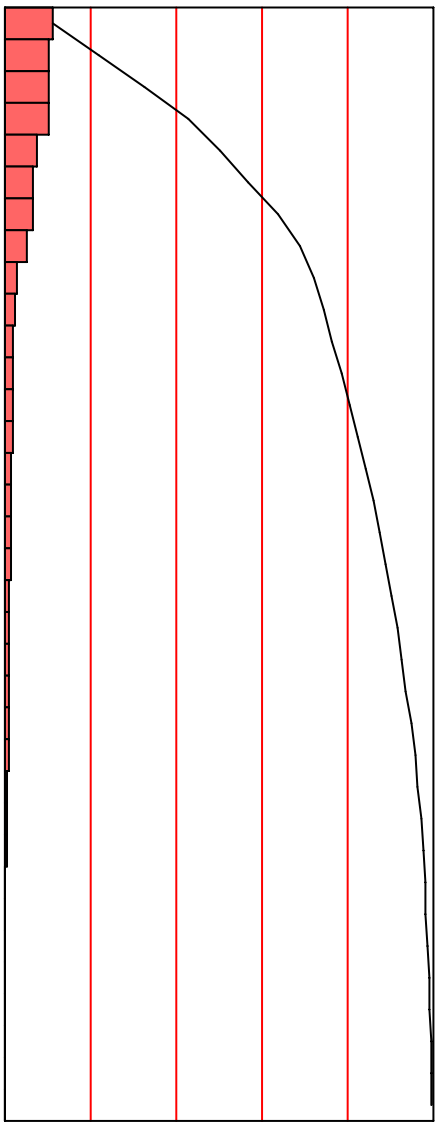

Figure 4.5. Pareto plot for variable influence on fractional pressure drop

Term	Orthog Estimate
Composition	1.119776
UC Width	-0.603450
Tortuosity	-0.564028
Porosity	0.556668
Length Fraction	0.383857
(UC Width-5.23141)*(Anode Thickness-1538.11)	0.305175
(Composition-75.5337)*(Composition-75.5337)	-0.197079
(UC Width-5.23141)*(Length Fraction-0.51329)	0.182175
(Length Fraction-0.51329)*(Anode Thickness-1538.11)	-0.107138
Anode Thickness	-0.105711
(Tortuosity-6.2102)*(Tortuosity-6.2102)	0.071475
(Porosity-0.29922)*(Porosity-0.29922)	-0.050788
(Anode Thickness-1538.11)*(Anode Thickness-1538.11)	-0.033223
(Composition-75.5337)*(Porosity-0.29922)	-0.016828
(Composition-75.5337)*(UC Width-5.23141)	0.015724
(Composition-75.5337)*(Tortuosity-6.2102)	0.015077
(Length Fraction-0.51329)*(Length Fraction-0.51329)	-0.014568
(UC Width-5.23141)*(UC Width-5.23141)	-0.006888
(Length Fraction-0.51329)*(Tortuosity-6.2102)	-0.006391
(UC Width-5.23141)*(Porosity-0.29922)	0.006181
(Composition-75.5337)*(Anode Thickness-1538.11)	0.006074
(Composition-75.5337)*(Length Fraction-0.51329)	0.006003
(Length Fraction-0.51329)*(Porosity-0.29922)	-0.005880
(Anode Thickness-1538.11)*(Tortuosity-6.2102)	0.005600
(Porosity-0.29922)*(Tortuosity-6.2102)	-0.001326
(UC Width-5.23141)*(Tortuosity-6.2102)	0.001023
(Anode Thickness-1538.11)*(Porosity-0.29922)	-0.000034

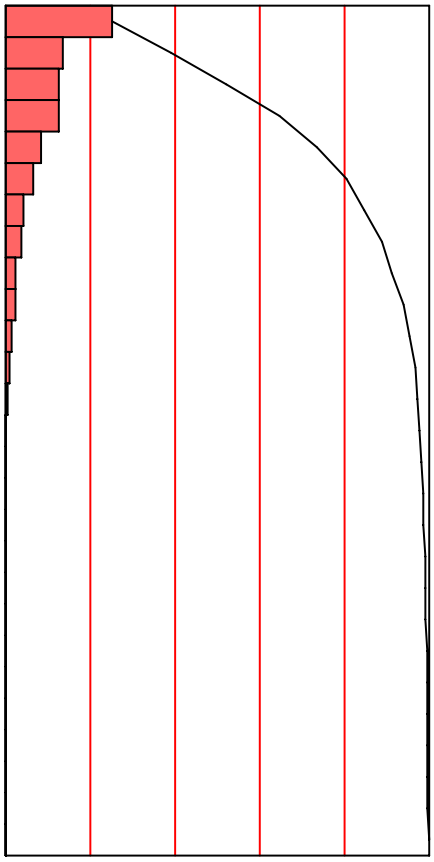

Figure 4.6. Pareto plot for variable influence on fuel depletion current density

For the anode ASR, the geometric factors of length fraction, unit cell width, and anode thickness demonstrate the greatest influence over performance. In this case, a clear division exits between the top three influential variables. The influence of the length fraction and unit cell width in this case can be linked to the calculation of the anode ASR, which is based upon the average voltage across the anode-interconnect contact surface. The size of this boundary is directly determined by the length fraction and unit cell width. Furthermore, the unit cell half-width, *a*, is again present within the eigenvalues of the solution for the anodic voltage distribution, and thus holds strong

influence over the mathematics of the voltage difference calculation. Parametric studies of anodic area specific resistance focus primarily on the effects of these two geometric variables.

Term	Orthog Estimate
Length Fraction	0.4345502
UC Width	0.3302587
Anode Thickness	0.2736253
(UC Width-5.54918)*(Length Fraction-0.48943)	0.2177987
(Length Fraction-0.48943)*(Anode Thickness-1471.35)	-0.1664099
(UC Width-5.54918)*(Anode Thickness-1471.35)	-0.1502083
(Current Density-0.77506)*(Length Fraction-0.48943)	-0.0688406
Composition	-0.0373519
(Composition-54.3832)*(Current Density-0.77506)	0.0331691
(Current Density-0.77506)*(UC Width-5.54918)	0.0294390
(Composition-54.3832)*(Length Fraction-0.48943)	-0.0214851
(Current Density-0.77506)*(Current Density-0.77506)	0.0212131
(Length Fraction-0.48943)*(Length Fraction-0.48943)	0.0192838
(Composition-54.3832)*(UC Width-5.54918)	0.0158155
(Current Density-0.77506)*(Anode Thickness-1471.35)	-0.0144725
(UC Width-5.54918)*(UC Width-5.54918)	-0.0069055
Current Density	0.0054649
(Composition-54.3832)*(Composition-54.3832)	-0.0044497
(Composition-54.3832)*(Anode Thickness-1471.35)	0.0043871
(Anode Thickness-1471.35)*(Anode Thickness-1471.35)	-0.0008876

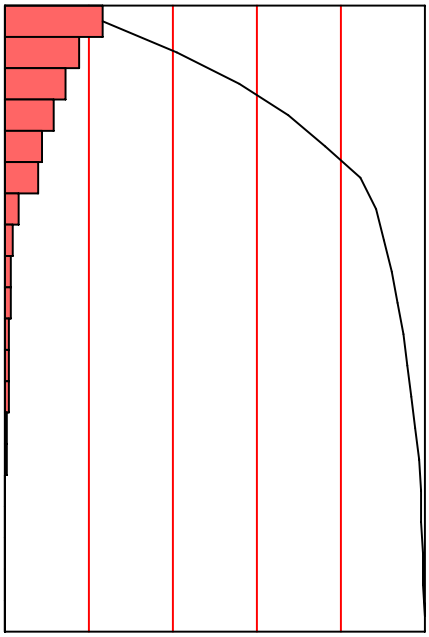

Figure 4.7. Pareto plot for variable influence on anode area specific resistance

Finally, the anode lead voltage has a primary dependence on current density, with a secondary dependence on composition. These two dependencies are similar to those of the fractional pressure drop. Therefore, the same studies of composition and current loading effects conducted for the fractional pressure drop are conducted for anode lead voltage.

Term	Orthog Estimate
Current Density	0.1342905
Composition	0.0660721
(Current Density-0.77506)*(UC Width-5.54918)	0.0306172
UC Width	0.0235395
Length Fraction	0.0234712
(Composition-54.3832)*(UC Width-5.54918)	0.0200127
(UC Width-5.54918)*(Length Fraction-0.48943)	0.0178184
(Current Density-0.77506)*(Length Fraction-0.48943)	0.0111478
(UC Width-5.54918)*(Anode Thickness-1471.35)	-0.0084681
Anode Thickness	0.0076807
(UC Width-5.54918)*(UC Width-5.54918)	0.0065016
(Length Fraction-0.48943)*(Anode Thickness-1471.35)	-0.0063593
(Composition-54.3832)*(Length Fraction-0.48943)	0.0057339
(Current Density-0.77506)*(Current Density-0.77506)	-0.0057142
(Composition-54.3832)*(Current Density-0.77506)	0.0055302
(Length Fraction-0.48943)*(Length Fraction-0.48943)	0.0041318
(Anode Thickness-1471.35)*(Anode Thickness-1471.35)	0.0019717
(Composition-54.3832)*(Anode Thickness-1471.35)	-0.0015056
(Current Density-0.77506)*(Anode Thickness-1471.35)	-0.0004656
(Composition-54.3832)*(Composition-54.3832)	0.0002190

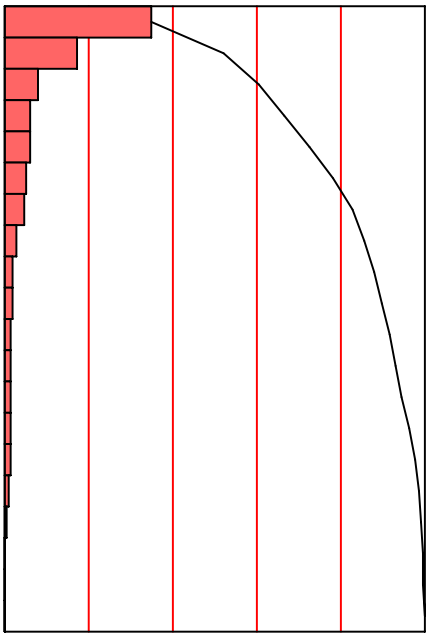

Figure 4.8. Pareto plot for variable influence on anode lead voltage

4.2 Parametric Studies of SOFC Performance

Parametric studies based on the above designs of experiments were conducted. All results shown share the following (constant) parameters: anode thickness (750 μm), temperature (1073 K), and anode porosity and tortuosity (0.30 and 5.0, respectively). For a constant current density load, the effects of fuel stream hydrogen composition on fractional pressure drop, fuel depletion current density, and anode lead voltage were examined for three representative unit cell widths (1.0, 5.0, and 10 mm) and three representative length fraction values (0.125, 0.50, and 0.875). For these same geometries, the effects of load current density on fractional pressure drop and anode lead voltage were examined at a constant fuel stream composition. Finally, length fraction effects on anodic ASR were examined for the three representative unit cell sizes.

At low fuel stream hydrogen concentrations, the anodic fractional pressure drop can approach 1.0 for smaller unit cell widths, as shown in Figure 4.9. Larger unit cell geometries demonstrate lower fractional pressure drops that are generally more stable across the range of concentrations examined. However, it must be noted that more stable, and in some cases almost constant, fractional pressure drops are achieved in larger unit cell geometries at the cost of the onset of fuel depletion at the anode-electrolyte interface occurring at much higher fuel stream hydrogen concentrations. For the smallest unit cell geometry (1.0 mm width), fuel depletion occurs primarily at lower fuel stream compositions as expected. Fuel depletion occurs at a high fuel stream composition in the largest unit cell geometry because for the same anode thickness (750 μm for the cases shown) the width of the interconnect rib is much greater than the anode thickness. In such cases the unit cell width serves as the greatest distance for hydrogen diffusion and results in a significant pressure drop in the lateral direction (Figure 4.10) and a relatively low pressure drop between points across the anode thickness.

Here, it is important to note that while the severe pressure drop in the lateral direction could be mitigated for larger unit cell geometries by increasing anode thickness, the analysis of such geometries is not desirable within the present work. State-of-the-art SOFC design has tended toward thin anode-electrolyte-cathode structures, with typical anode thicknesses between 250 and 2500 μm. Within this range, anode supported SOFCs typically employ anodes of 500 to 1500 μm in thickness.

The onset of fuel depletion is demonstrated by the fractional pressure drop in Figure 4.9 reaching a plateau at approximately 80% hydrogen in the fuel stream for the largest unit cell geometry studied. In the tests conducted if the prescribed current density

demand (herein 1.0 A/cm^2) exceeded the fuel depletion current density (which is based upon operating conditions), the latter value replaced the former value; *i.e., excessive current demand was precluded*. This replacement results in the forced maintenance of a constant fractional pressure drop. Thus the plateau in fractional pressure drop occurs when the fuel depletion current density for a given geometry is less than the current density demand.

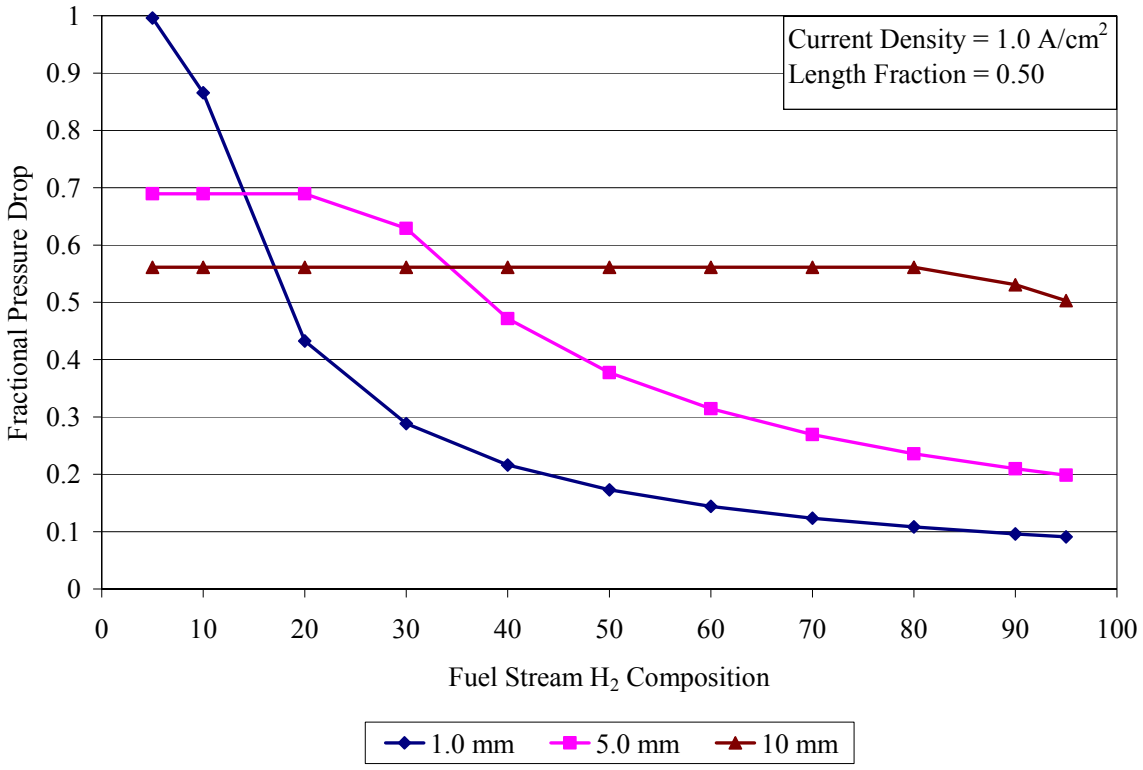

Figure 4.9. Fractional pressure drop dependence on fuel stream hydrogen content

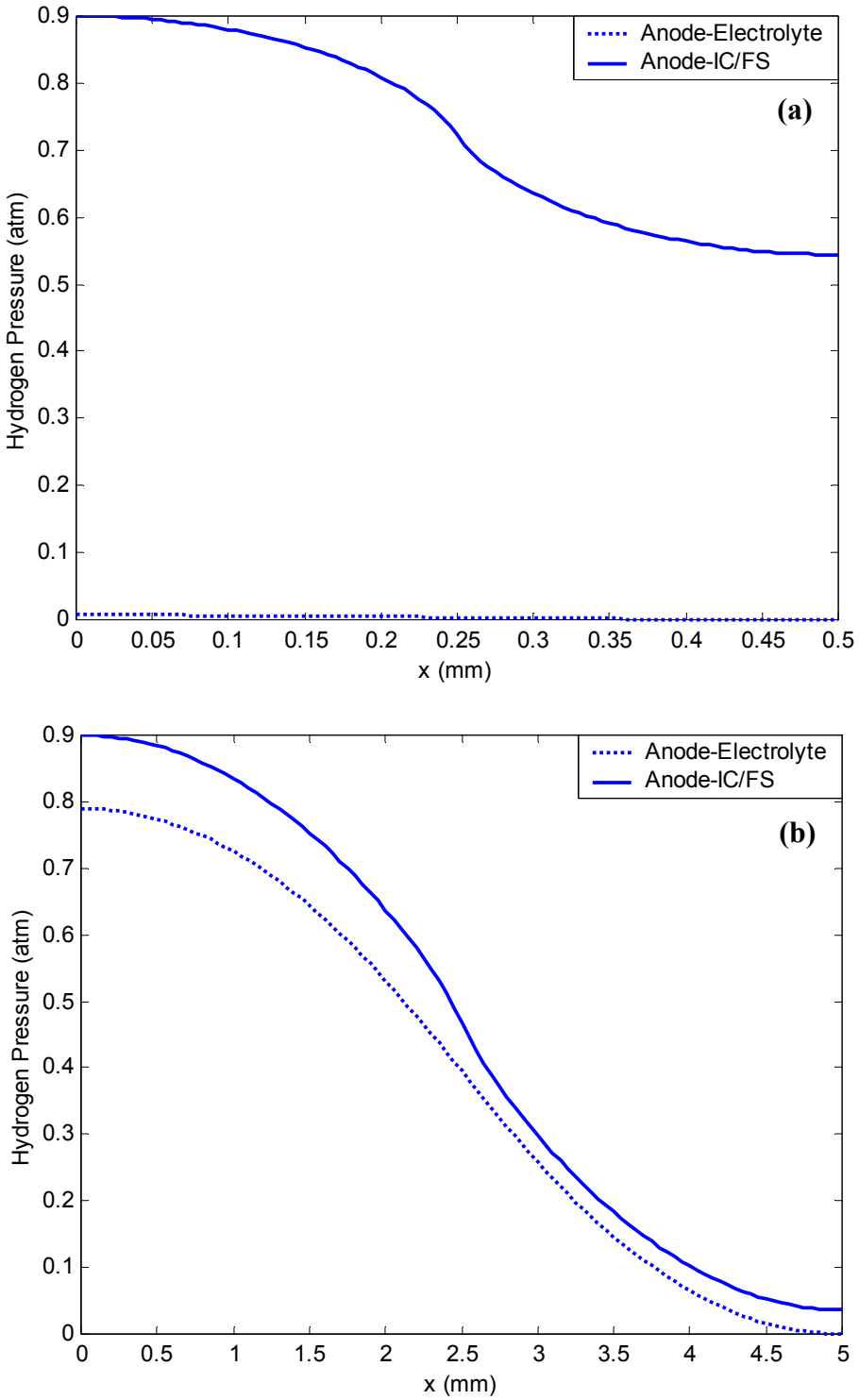

Figure 4.10. Hydrogen partial pressure distributions at the fuel depletion current density for unit cells of (a) 1.0 mm width and (b) 10.0 mm width (90% fuel stream hydrogen)

The dependence of fractional pressure drop on current density is further illustrated in Figures 4.11-4.13. The results shown are for tests conducted for a fuel stream hydrogen composition of 90% and a range of current densities from 0.1 to 2.0 A/cm^2. In Figures 4.12 and 4.13, the limiting aspects of larger unit cell widths become apparent. In each of these figures, the point coinciding with fuel depletion current density for a given geometry is circled. For example, at fuel stream hydrogen concentrations lower than 90% a SOFC with a unit cell width of 10 mm and a length fraction of 0.50 cannot supply a current density greater than ~1.05 A/cm^2 without the occurrence of fuel depletion at the anode-electrolyte interface. Again, the larger unit cell widths are limiting because, for the same anode thickness, the lateral distance for hydrogen diffusion is significantly greater that the distance for diffusion across the anode.

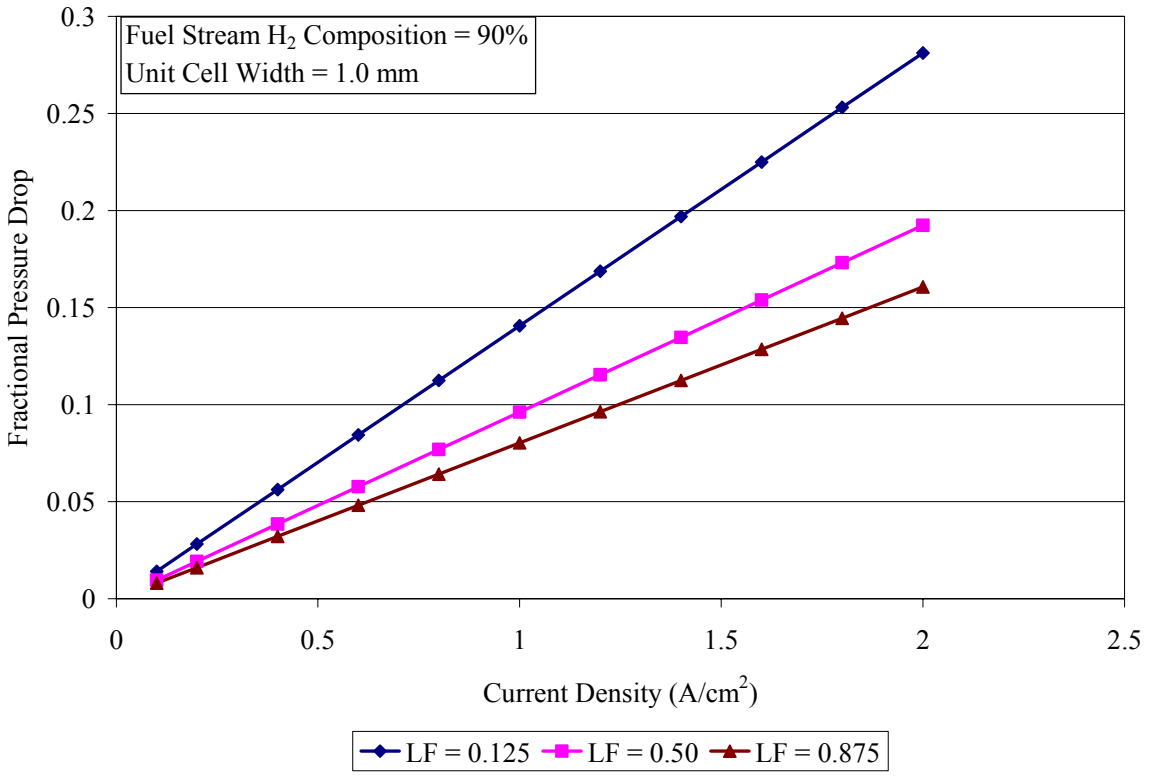

Figure 4.11. Fractional pressure drop dependence on current density

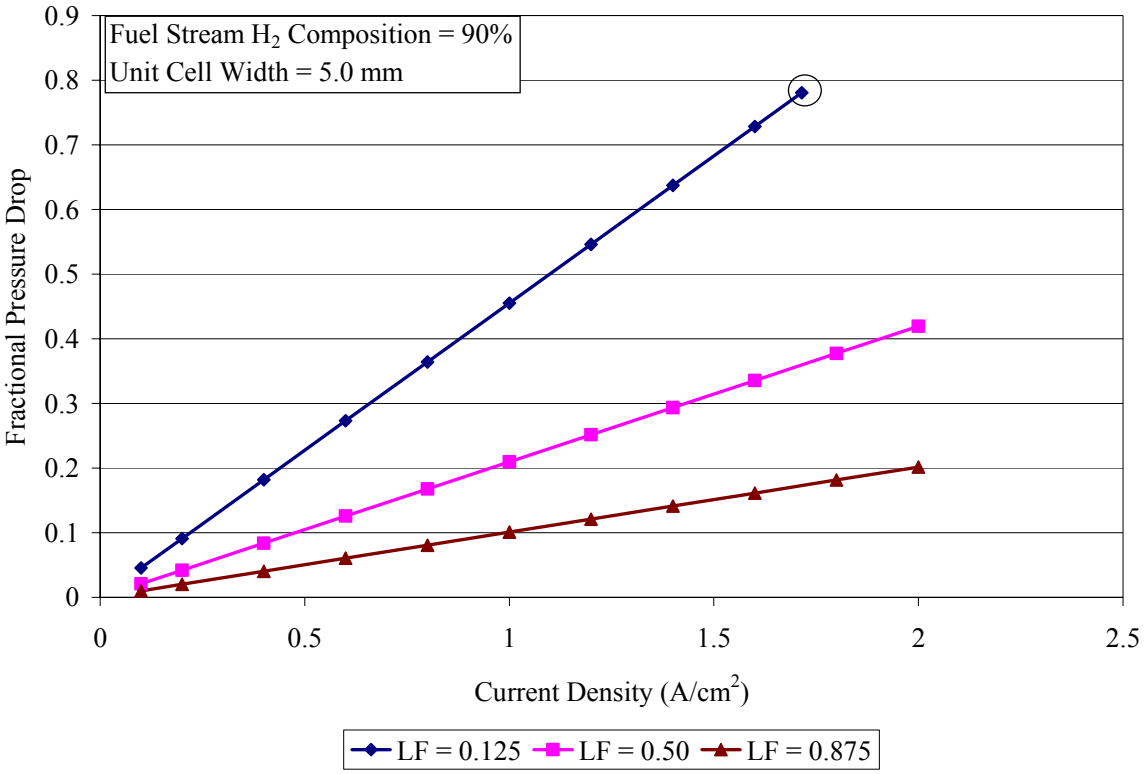

Figure 4.12. Fractional pressure drop dependence on current density

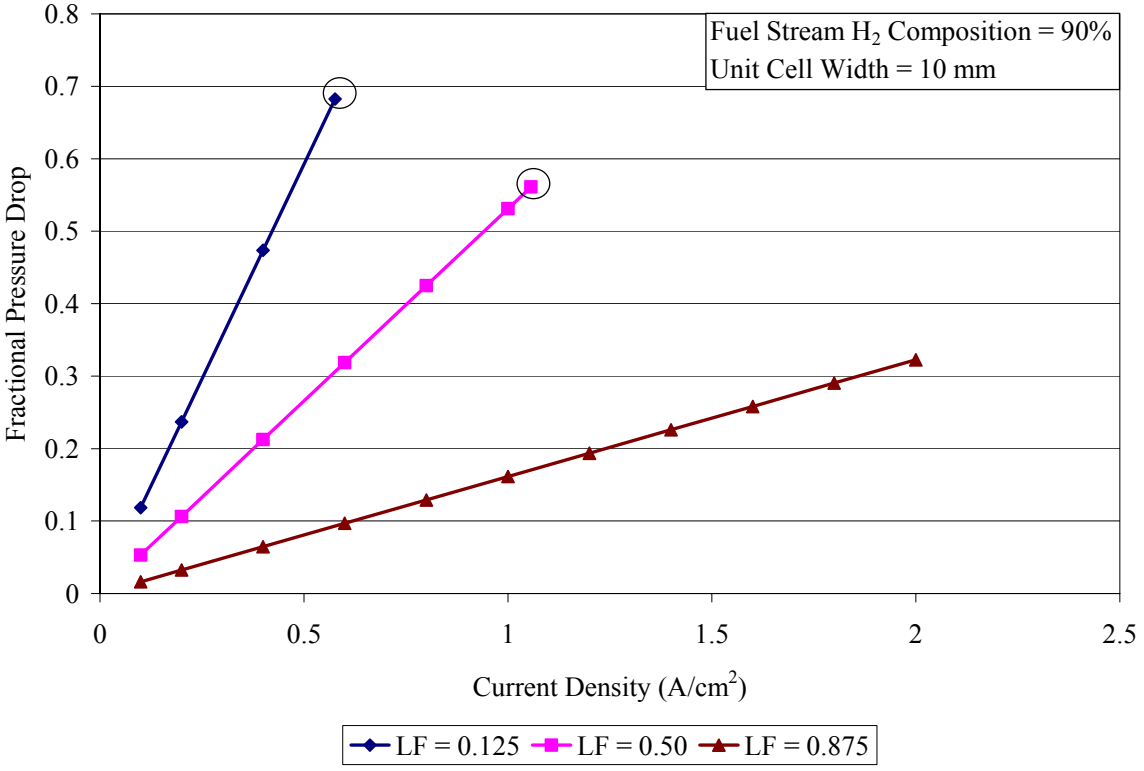

Figure 4.13. Fractional pressure drop dependence on current density

Further manifestations of the advantage of smaller SOFC unit cell widths can be seen through examining the dependence of fuel depletion current density on fuel stream hydrogen content. This dependence is illustrated in Figures 4.14-4.16 for the representative unit cell geometries studied. It is evident from these three figures that smaller SOFC unit cell widths result in the achievement of higher fuel depletion current densities. For example, at all concentrations shown a SOFC with a unit cell width of 1.0 mm can achieve operational current densities approximately three times greater than those achieved by a SOFC with a unit cell width of 5.0 mm. The same 1.0 mm unit cell SOFC can achieve fuel depletion current densities almost ten times greater than those achieved with a SOFC with a 10 mm unit cell. Representative values of the fuel depletion current densities achieved for each unit cell geometry are given in Table 4.4.

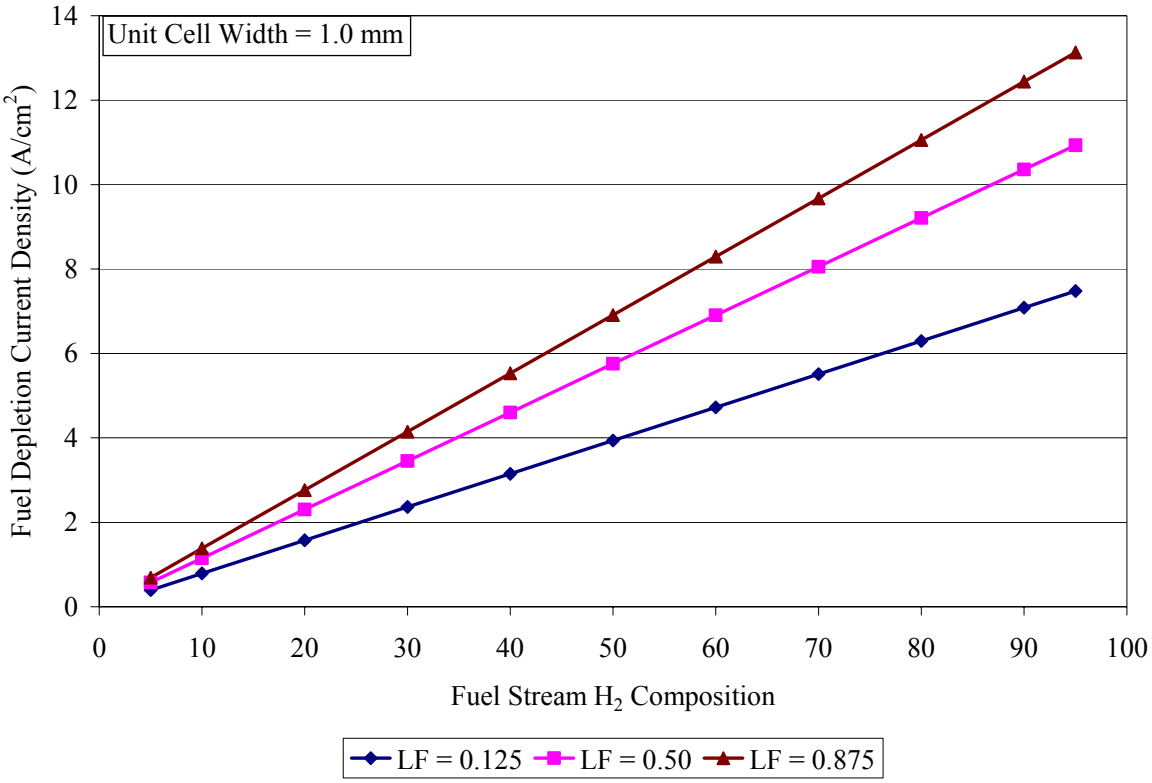

Figure 4.14. Fuel depletion current density as a function of fuel stream hydrogen content

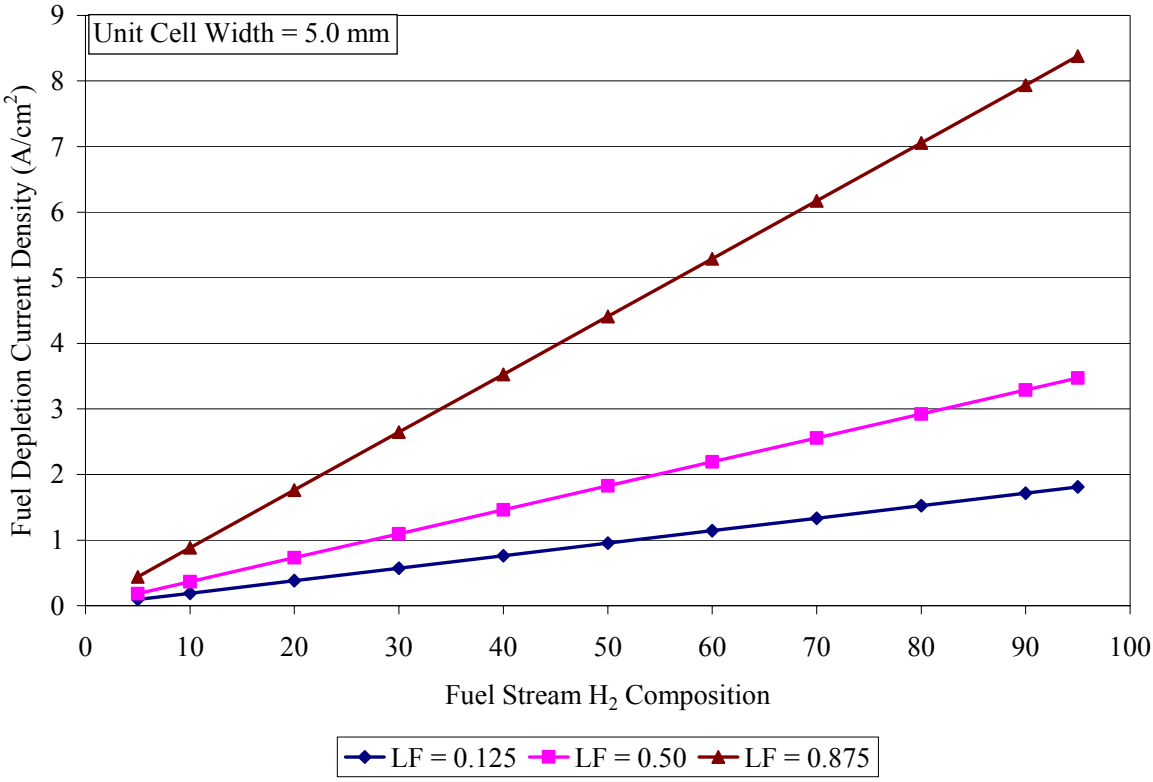

Figure 4.15. Fuel depletion current density as a function of fuel stream hydrogen content

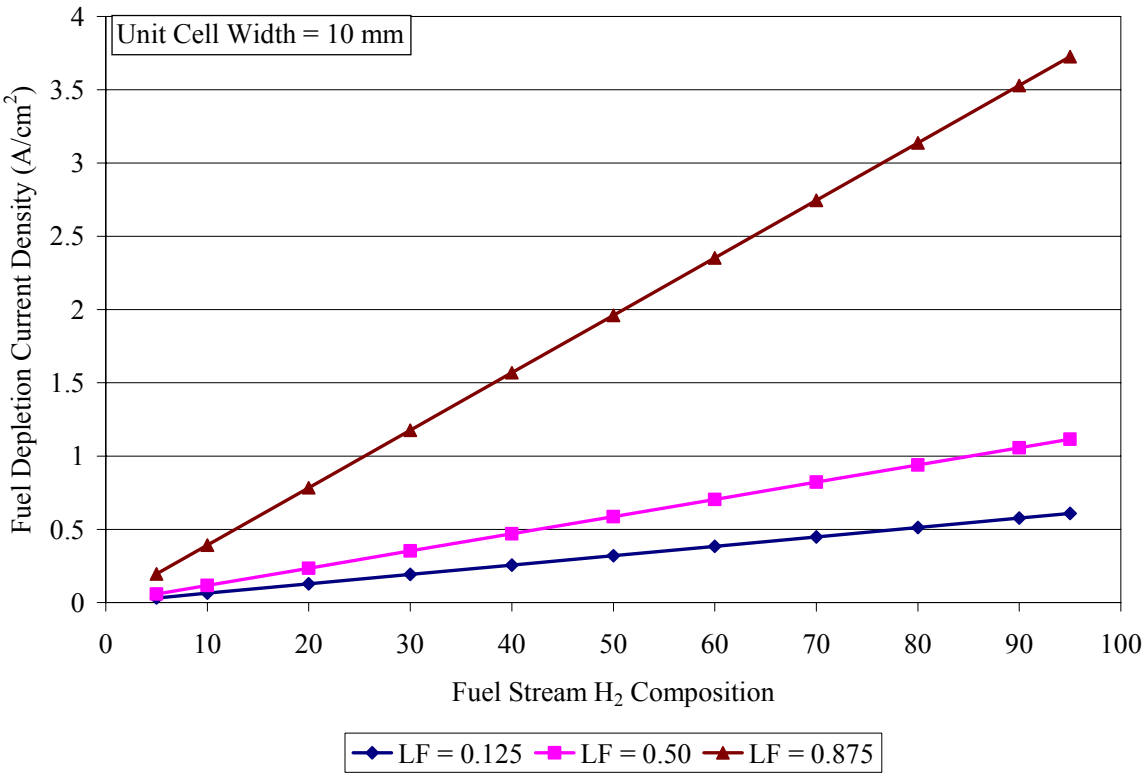

Figure 4.16. Fuel depletion current density as a function of fuel stream hydrogen content

Table 4.4. Fuel depletion current densities over a range of fuel stream (FS) compositions

FS Hydrogen Composition	Fuel Depletion Current Density (A/cm^2)		
	1.0 mm	5.0 mm	10 mm
5 %	0.58	0.18	0.06
10 %	1.15	0.37	0.12
50 %	5.75	1.83	0.59
90 %	10.36	3.29	1.06
95 %	10.93	3.47	1.12

Finally, the advantage of smaller unit cell widths can be seen through a comparison of the effects of unit cell geometry on anodic electronic transport phenomena. As previously shown, ASR can increase significantly when accounting for geometry effects (~36% between a button-cell case and a geometry of unit cell width of 2.0 mm and LF = 0.5). For smaller unit cell widths this increase is less pronounced, as shown in Figure 4.17. A SOFC with a unit cell width of 1.0 mm and length fraction 0.50 experiences an increase of ~10% in anodic ASR compared to the button-cell case (i.e. LF = 0**).** This reduced ASR is the result of reduced sheet resistance within the anode, caused by shorter electronic transport paths within the lateral direction. Additionally, smaller geometries show better electronic performance over a range of fuel stream hydrogen compositions. This enhanced performance is partially due to the fact that smaller geometries are not as limited by fuel depletion as larger geometries. As shown in Figure 4.18, SOFCs with larger unit cell geometries must operate within restricted ranges of fuel stream hydrogen composition to avoid the onset of fuel depletion. For the prescribed current density of 1.0 A/cm^2 fuel depletion occurs between 80% and 90% hydrogen for a unit cell of 10 mm width, and between 20% and 30% hydrogen for a unit cell of 5.0 mm

width. Of the unit cell geometries examined, only the smallest geometry achieves operation over the full range of fuel stream compositions. In this case the anode lead voltage shows a steep rise, suggesting a dominance of concentration polarization losses. This increased dominance of concentration losses can be attributed to the onset fuel depletion in smaller unit cell geometries occurring at current densities near the traditionally defined limiting current density. As demonstrated in Figure 4.10a, fuel depletion in such geometries corresponds to what is almost the complete absence of hydrogen at the anode-electrolyte interface. A final demonstration of the enhanced electronic performance of smaller unit cell geometries can be made by comparing the anode lead voltages within the operational ranges of fuel stream composition common to all the unit cell geometries studied. In these ranges, from 30% to 95% hydrogen composition, the greater ohmic losses associated with the increased sheet resistance in larger unit geometries are shown to detract from the overall cell performance. The higher anode lead voltages associated with larger unit cell geometries will ultimately result in lower overall cell voltage (as defined in Equation (4.5)). This fact is shown by plotting the voltage-current density characteristic of the cell geometries examined (Figure 4.19). The cell voltage is directly proportional to the cell efficiency, which is calculated based on the lower heating value of hydrogen and the fuel utilization, μ_F, according to Equation (4.6). Thus higher voltages result in higher overall cell efficiencies.

$$V_{cell} = V_{cathode\ lead} - V_{anode\ lead} \tag{4.5}$$

$$\eta_{cell} = \mu_F \left(\frac{V_{cell}}{1.25} \right) \times 100\% \tag{4.6}$$

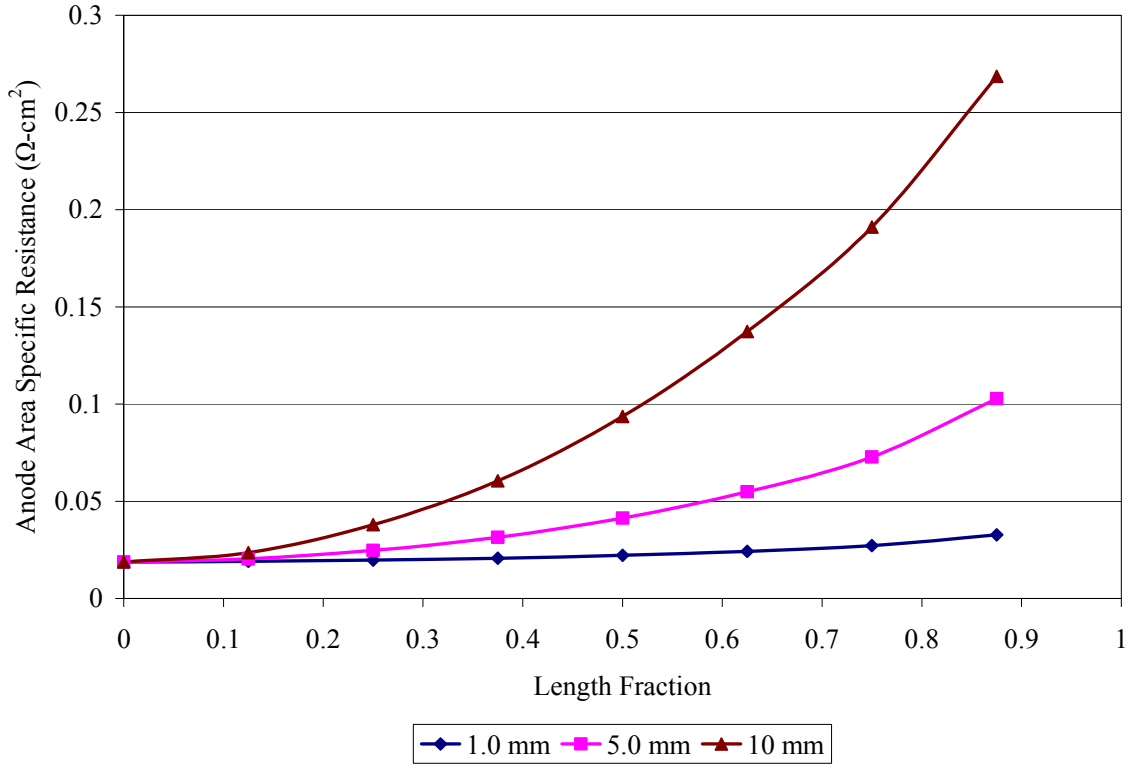

Figure 4.17. Anode ASR as a function of length fraction for several unit cell sizes

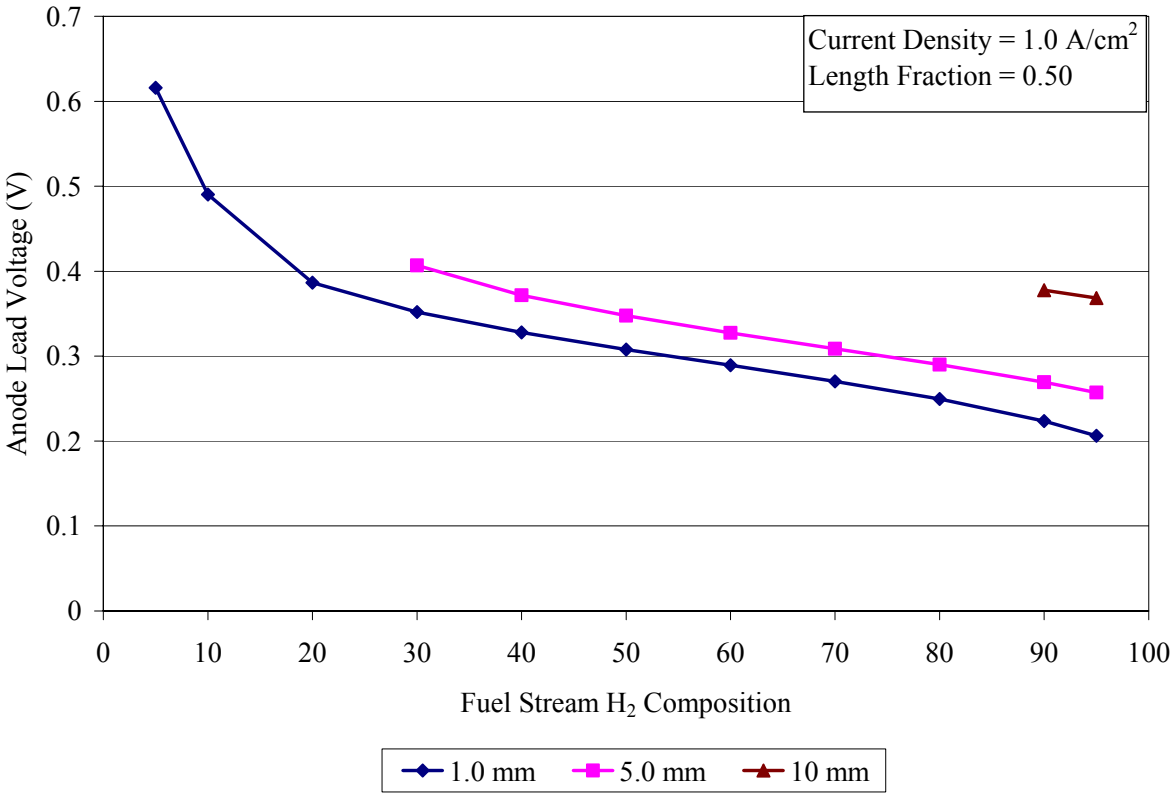

Figure 4.18. Anode lead voltage dependence on fuel stream hydrogen content

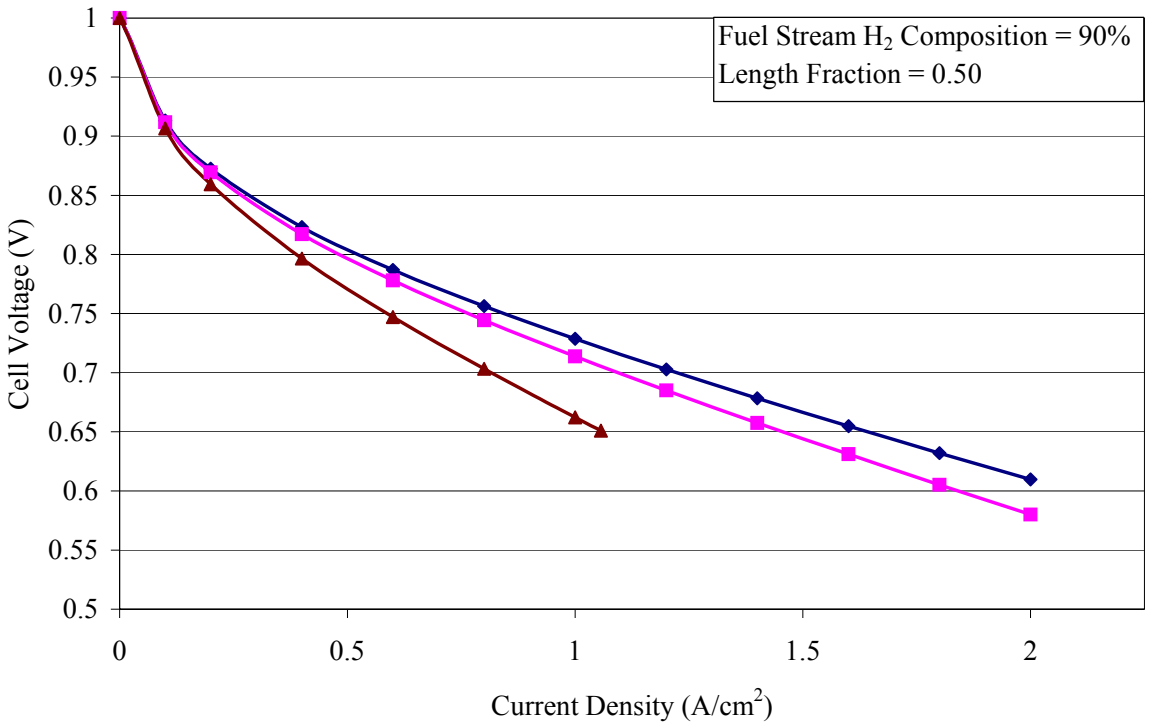

Figure 4.19. Voltage current characteristic curves for several unit cell geometries

With the advantages of smaller unit cell widths established, the effects of length fraction on mass and electronic transport can be further explored. This exploration is facilitated through the definition of a normalized pressure drop and a normalized area specific resistance. These parameters are defined in Equations (4.7) and (4.8).

$$\Delta p^*_{H_2} = \frac{\left(\Delta p_{H_2} / p_{H_2,an-FS}\right)}{\left(\Delta p_{H_2} / p_{H_2,an-FS}\right)_{\max}} = \frac{\left(\Delta p_{H_2}\right)}{\left(\Delta p_{H_2}\right)_{\max}} \tag{4.7}$$

$$ASR^* = \frac{ASR}{ASR_{\max}} \tag{4.8}$$

The normalized pressure drop and the normalized ASR are compared in Figure 4.20 for a unit cell of width 1.0 mm and a current density of 1.0 A/cm^2. As previously

demonstrated, ASR is primarily determined by geometric parameters. Fractional pressure drop is influenced primarily by operational variables. Thus, two cases for fuel stream hydrogen composition are shown: one for high hydrogen content and one for low hydrogen content. For high fuel stream hydrogen composition the fractional pressure drop and the anode ASR reach the same percentage of their respective maximum values at a length fraction of ~0.50. As predicted, lower hydrogen content in the fuel stream demonstrates a shift towards the dominance of mass transport effects. This dominance is shown by the shift of the intersection of the normalized pressure drop and the normalized ASR curves toward higher length fraction values. The dominance of mass transport effects on performance is also shown by the reduced sensitivity of the normalized pressure drop with respect to changes in length fraction. For such cases, significant increases in length fraction yield relatively slight changes in pressure drop.

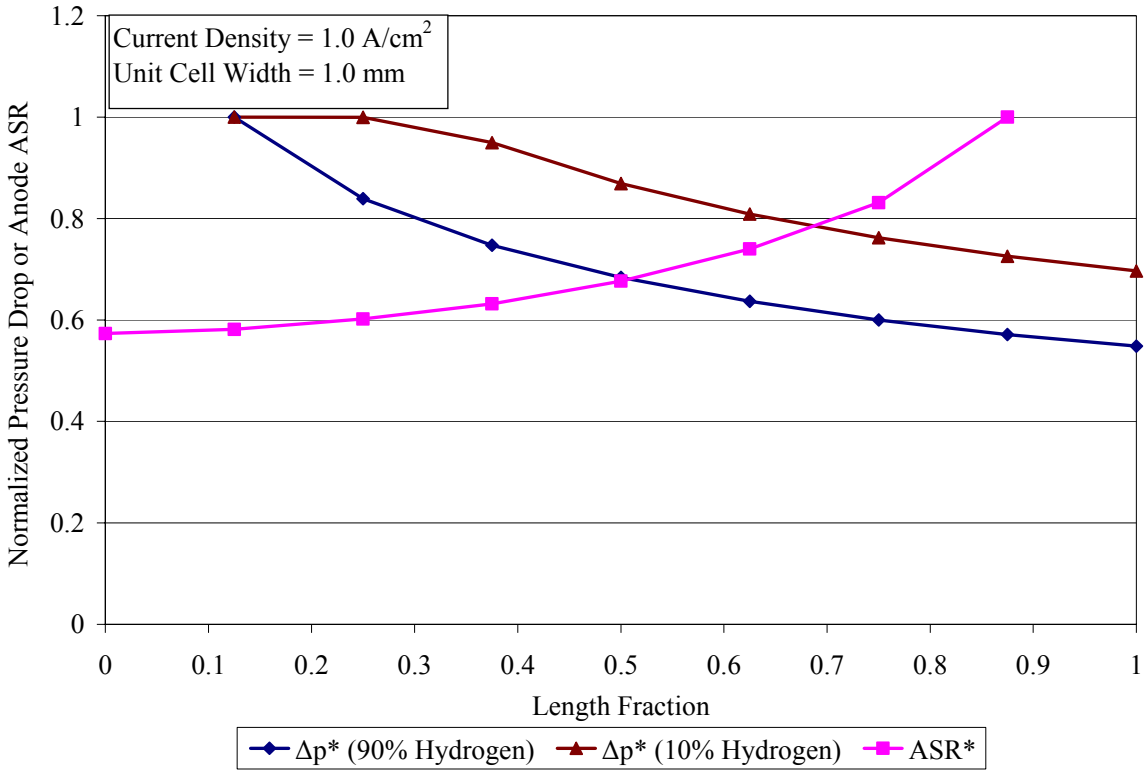

Figure 4.20. Balance of mass and electronic transport geometry effects for SOFC

4.3 Application to Solid Oxide Electrolysis Cells

Two primary distinctions exist between the electrolysis and fuel cell modes of solid oxide cells. Under operation as SOFCs, solid oxide cells consume hydrogen and generate electrical current. As solid oxide electrolysis cells (SOECs), solid oxide cells produce hydrogen from a hydrogen-steam mixture under an applied electrical current. Thus, for SOFC operation the fuel stream hydrogen concentration limits mass transport performance, while for SOEC operation the steam concentration is the limiting mass transport variable. Furthermore, for SOFC operation electrical current is treated as positive, as it is produced by the cell, while the electrical current supplied to the cell under SOEC operation is treated as negative. This sign convention for current is

common within existing analyses, where SOEC operation is simply treated as the reverse of SOFC operation [14, 28]. Although the simplifying assumption of reversed operation is convenient for the present analysis, the development of a more nuanced understanding of SOEC operation will likely be needed in future work.

Drawing upon the distinctions above, the parametric studies conducted for SOFC performance were run under reversed current conditions. Fuel depletion current densities were determined based on fuel stream steam content. This redefinition was achieved by replacing the fuel stream hydrogen partial pressure in the SOFC fuel depletion current density with the fuel stream steam partial pressure and multiplying by negative one. The resulting SOEC fuel depletion current density is given in Equation (4.9).

$$i''_{FD,SOEC} = -\frac{2FD_{H2-H2O}}{R_u T}\frac{\varepsilon}{\tau}\frac{p_{H_2O,an-FS}}{t_{an} + \sum_{n=1}^{\infty} B_n\left[\cosh(\lambda_n t_{an}) - \cos n\pi\right]} \tag{4.9}$$

$$B_n = \frac{2\sin(\lambda_n b)}{n\pi\lambda_n \sinh(\lambda_n t_{an})}\left(\frac{a}{b}\right) \tag{4.10}$$

The results of the SOEC parametric studies are summarized in Figures 4.21-4.23. As is the case with SOFCs, larger unit cell geometries are more stable with respect to steam fractional pressure drop and show lower overall values of fractional pressure drop (see Figure 4.21), but this apparent advantage again comes at the cost of limitations with respect to fuel depletion. These limitations are further demonstrated through the examination of voltage-current density traces across both SOFC and SOEC operation shown in Figure 4.22. The advantages of smaller unit cell geometries under SOFC operation are readily discernible, and upon closer examination (Figure 4.22b) these

geometries demonstrate lower voltage requirements in SOEC operation. The voltage-current density traces shown in Figure 4.22 are for a fuel stream composition of 90% hydrogen and 10% steam. However, the lower voltage advantage of smaller unit cell geometries holds true across the range of fuel stream compositions studied, as shown in Table 4.5.

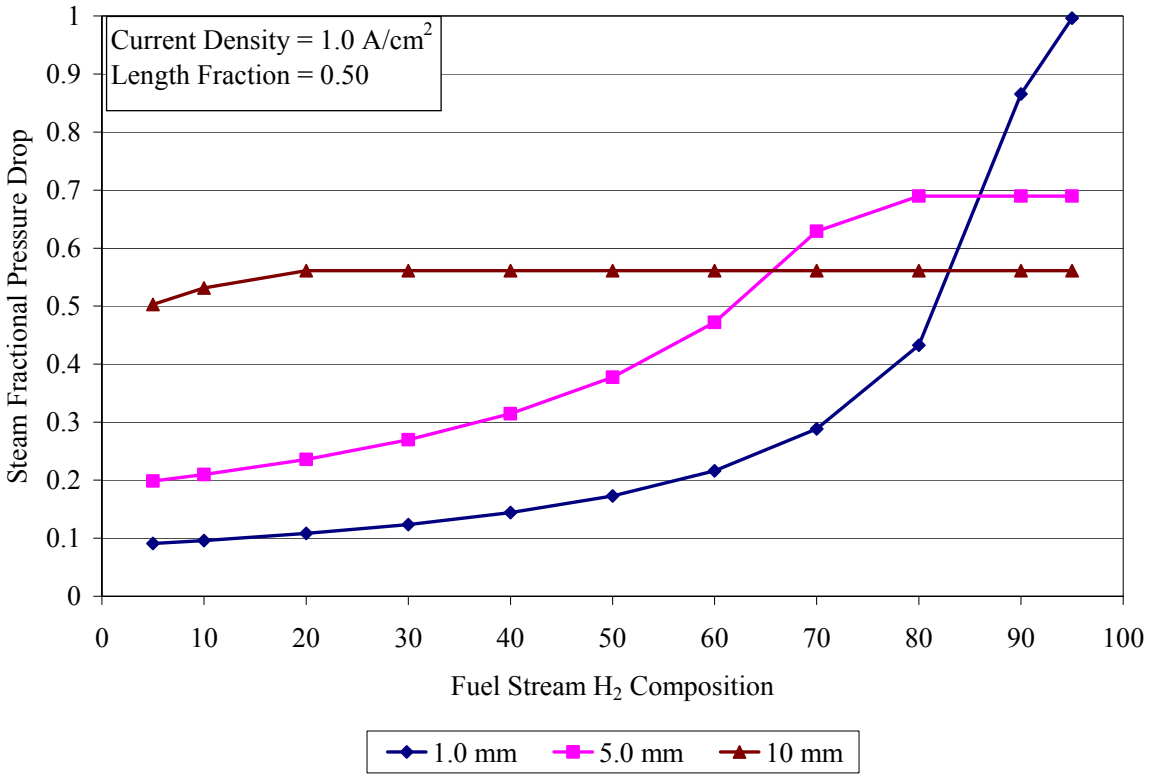

Figure 4.21. Steam fractional pressure drop dependence on fuel stream H_2 content

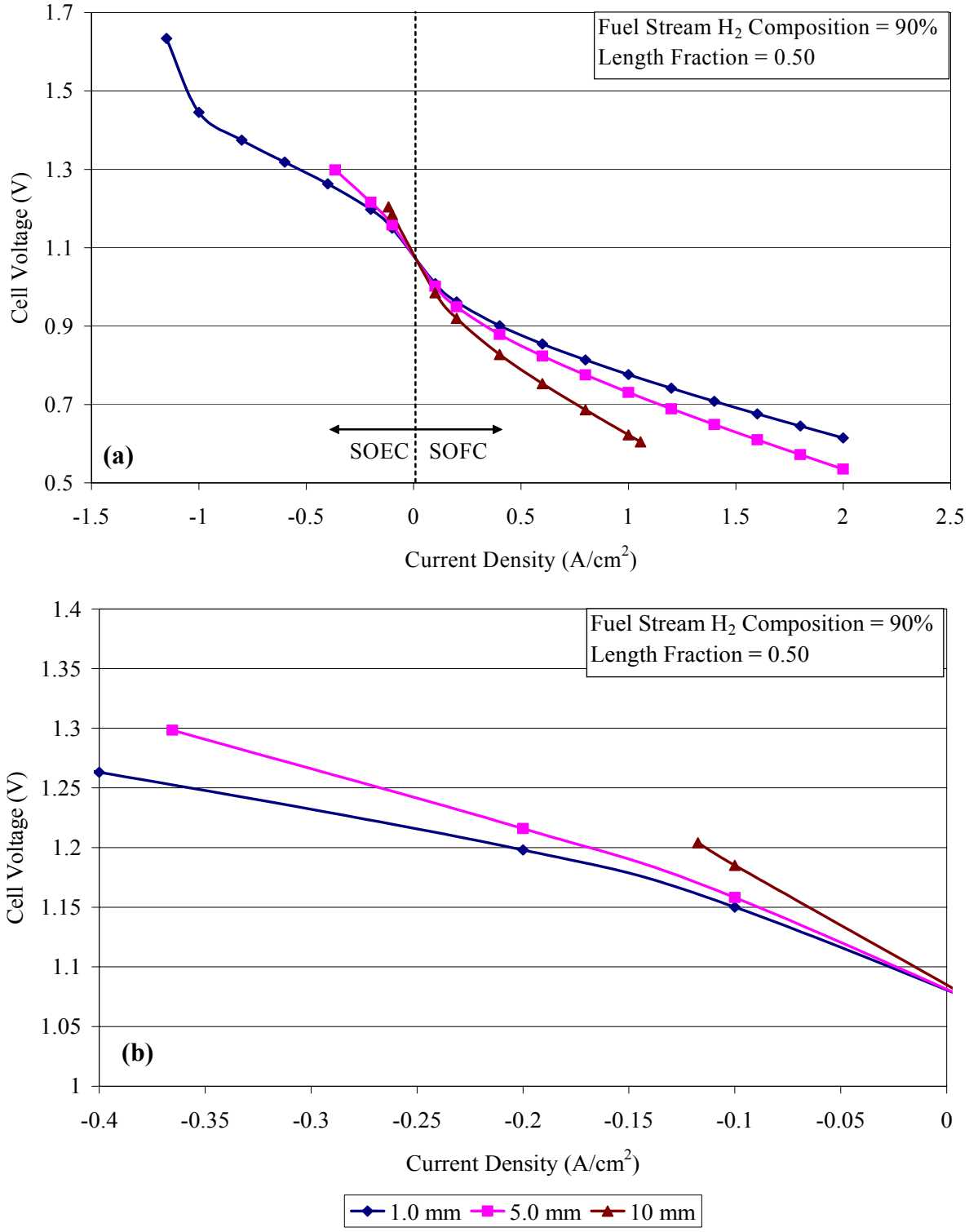

Figure 4.22. Voltage-current density characteristics (a) for the SOFC and SOEC operation of several solid oxide cell unit cell geometries and (b) a detail of SOEC characteristics

Table 4.5. SOEC voltage requirements over a range of fuel stream compositions

Unit Cell Width (mm)	Required Cell Voltage (V) at 1.0 A/cm^2				
	5% H_2	10% H_2	50% H_2	90% H_2	95% H_2
1.0	1.16	1.18	1.26	1.45	N/A
5.0	1.21	1.22	1.30	N/A	N/A
10	1.32	1.33	N/A	N/A	N/A

N/A: current density demand greater than cell limiting current density

Finally, as in the case of SOFC operation, insights into SOEC performance can be gained from examining the length fraction effects on mass and electronic transport and comparing them through a normalized fractional pressure drop and normalized anode ASR. In the case of SOEC operation, however, the normalized pressure drop must be defined based on steam, and not hydrogen, partial pressures. This definition is altered because, as previously stated, under SOEC operation steam partial pressure limits mass transport. The balance shown in Figure 4.23 is essentially the same as that shown in Figure 4.20 with the pressure drop behavior inverted. At higher fuel stream hydrogen partial pressure (i.e. lower steam concentration) mass transport effects become more dominant in SOECs, and at lower fuel stream hydrogen partial pressure the fractional pressure drop and the anode ASR reach the same percentage of their respective maximum values at a length fraction of ~0.50. As anode area specific resistance is primarily a function of cell geometry, there is no change seen between the ASR values in Figures 4.20 and 4.23.

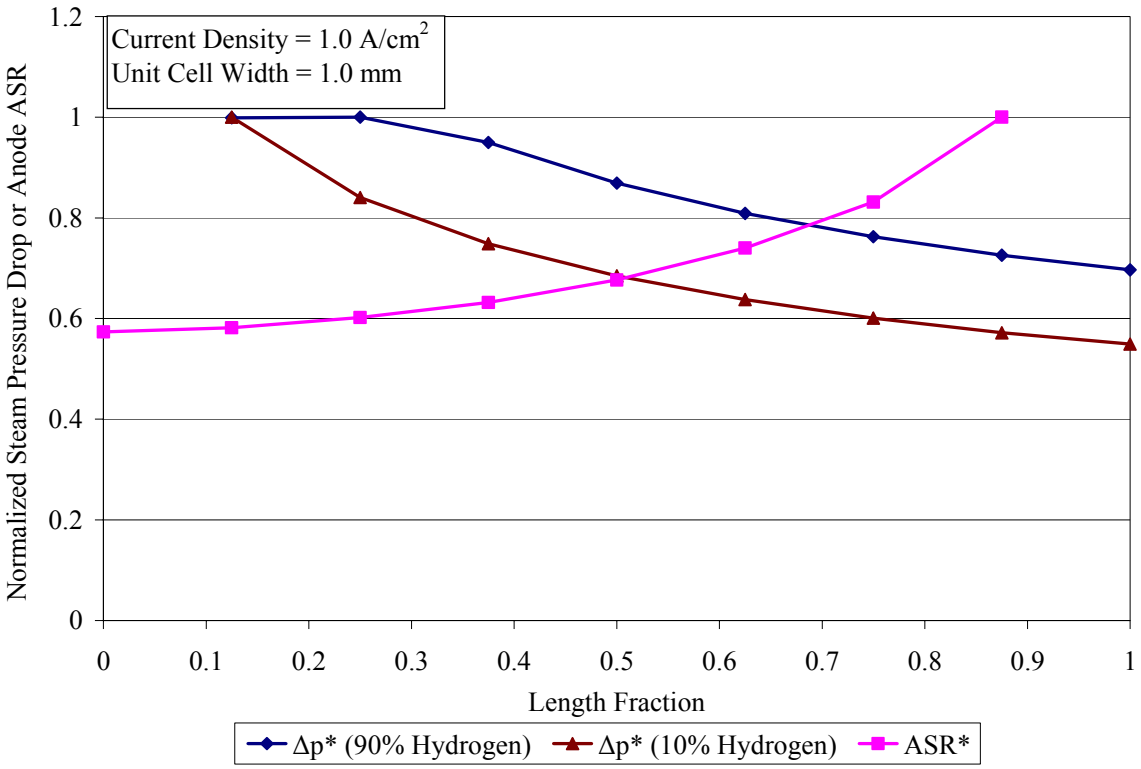

Figure 4.23. Balance of mass and electronic transport geometry effects for SOEC

CHAPTER 5

ELECTROCHEMICAL IMPACT OF DELAMINATION

The electrochemical degradation of solid oxide fuel cells presents a serious design challenge. Cracking about and within the critical electrolyte component layer can lead to increased internal ohmic losses. Such losses caused by delamination cracks located at the electrode-electrolyte interfaces can be explored via analytical and computational methods. Analytically, potential flow theory can be applied to crack-affected regions of the electrolyte to resolve voltage and current distributions and glean an understanding of the mechanisms of electrochemical degradation. However, analytical solutions for delamination problems demonstrate slow convergence, which presents an increased computational burden. For this reason computational methods, such as finite element analysis, greatly facilitate the analysis of delamination cracking phenomena. Finite element analysis (FEA) studies can be implemented based upon a thermal analogy to ionic conduction. These FEA studies can be employed in tandem with analytic solutions to develop dimensionless parameters that aid understanding the electrochemical impact of delamination.

In the following analyses delamination cracks are treated as current flow obstructions that lead to the distortion of current within the electrolyte. This distortion serves to lengthen transport paths and therefore increase resistance. Given increasingly thin electrolytes, this current distortion may lead to the effective loss of electroactive area at both electrode-electrolyte interfaces via actual and "virtual" delamination. Additionally, regions of unutilized electrolyte cross-sectional area may result. These

collective phenomena are herein referred to as “masking”. The occurrence of masking can be described using a dimensionless current parameter that operates as a function of a dimensionless electrolyte thickness parameter. Furthermore, a method is proposed for incorporating the electrochemical effects of delamination within full cell- and stack- level simulations using the dimensionless parameters developed. The relation of these parameters allows for the establishment of a threshold at which masking will occur.

5.1 Analytic Model

For the case of delamination, a “button cell” is a small, circular, sample SOFC fuel cell which includes an electrode-electrolyte interfacial crack, as shown in Figure 5.1. Analysis of the voltage distribution within this button-cell can be used to provide insight into the effects of delamination cracks on electrolyte resistance.

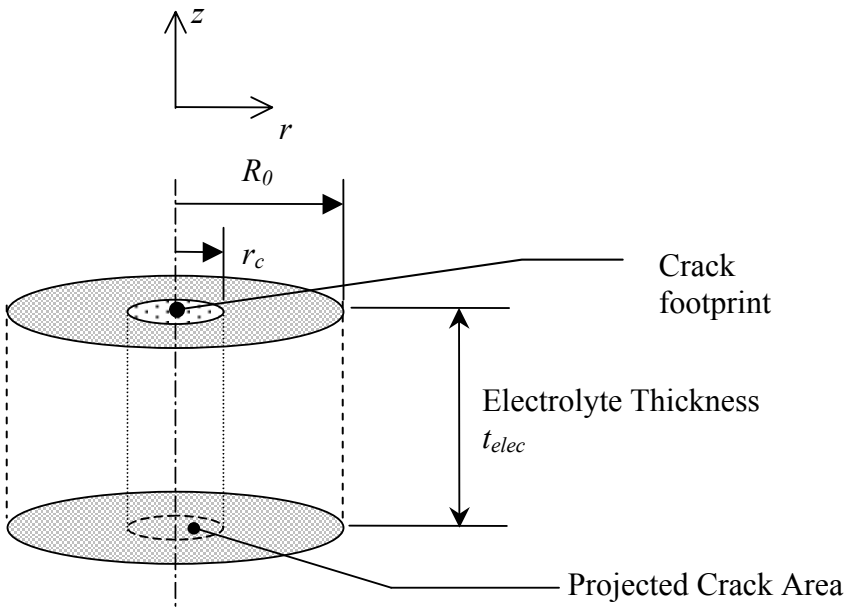

Figure 5.1. Delamination crack zone and affected area

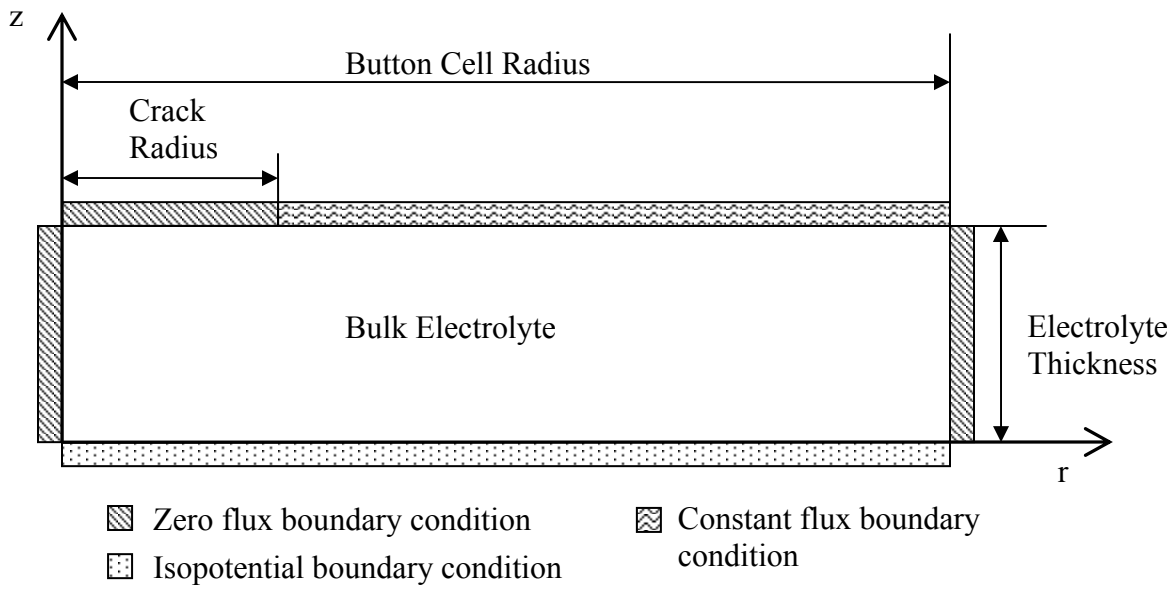

Figure 5.2. Domain of boundary value problem for delamination

The boundary value problem for the electrolyte voltage distribution is defined in Equations (5.1)-(5.5). This problem consists of the Laplace equation based upon a relative voltage, as defined in Equation (5.2), with no current generation within the electrolyte. An isopotential boundary condition is specified at the unaltered electrode-electrolyte interface. A composite Neumann boundary condition is presumed at the cracked interface. An insulated condition is presumed inside of the crack radius, and a uniform[1] current flux is specified for radii greater than that of the delamination crack.

$$\frac{\partial^2 V^*}{\partial z^2}+\frac{\partial^2 V^*}{\partial r^2}+\frac{1}{r}\frac{\partial V^*}{\partial r}=0 \tag{5.1}$$

$$V^*(r,z)=V(r,z)-V(r,0) \tag{5.2}$$

$$V^*(r,0)=0 \tag{5.3}$$

[1] Future studies where this isoflux condition is relaxed and/or replaced are plausible.

$$\frac{\partial V^*}{\partial z}\left(r, t_{electrolyte}\right) = \begin{cases} 0; & 0 \le r < r_c \\ \dfrac{i''_{ideal}}{\sigma_{elec}} \dfrac{R_0^2}{R_0^2 - r_c^2}, & r_c \le r < R_0 \end{cases} \tag{5.4}$$

$$\frac{\partial V^*}{\partial r}(0, z) = 0 \;,\; \frac{\partial V^*}{\partial r}(R_0, z) = 0 \tag{5.5}$$

The scaling factor in Equation (5.4) is the result of charge conservation within the button-cell volume and the reduction in area between the participating interfaces. The total current crossing each interface is equated and the current density at the cracked interface is found. This calculation readily reveals the scaling relationship.

$$i_{cracked} = i_{ideal}$$

$$i''_{cracked} \int dA_{cracked} = i''_{ideal} \int dA_{non-cracked}$$

$$i''_{cracked} = i''_{ideal} \frac{R_0^2}{R_0^2 - r_c^2}$$

The solution for the electrolyte voltage distribution in the presence of a delamination crack is given in Equation (5.6). The eigenvalue, λ_n, is defined in Equation (5.7), where β_n is the nth positive zero of the first order Bessel function $J_1(r)$.

$$\begin{aligned} V(r, z) = V(r, 0) &+ \frac{i''_{ideal}}{\sigma_{elec}} \left(\frac{R_0}{R_0 + r_c} \right) z \\ &- \sum_{n=1}^{\infty} \frac{2 i''_{ideal}}{\sigma_{elec} \lambda_n^2 \cosh(\lambda_n t_{elec})} \frac{r_c}{R_0^2 - r_c^2} \frac{J_1(\lambda_n r_c)}{J_0^2(\lambda_n R_0)} \left[\sinh(\lambda_n z) J_0(\lambda_n r) \right] \end{aligned} \tag{5.6}$$

$$\lambda_n = \frac{\beta_n}{R_0} \tag{5.7}$$

5.1.1 Dimensionless Parameters

Further analysis of the effects of delamination cracks can be facilitated through the use of three dimensionless parameters: a dimensionless current, a dimensionless electrolyte thickness, and a dimensionless radius. These parameters are defined in Equations (5.8)-(5.10).

$$i^* = \frac{i_{cracked,\text{Projected Crack}}}{i_{ideal,\text{Projected Crack}}} \tag{5.8}$$

$$r^* = \frac{r_{\|}}{r_c} \tag{5.9}$$

$$t^* = \frac{t_{elec}}{r_c} \tag{5.10}$$

In the absence of a delamination, the current passing through the electrolyte is of uniform density at both interfaces (Figure 5.3a). With the onset of a delamination, the electro-active area at the cracked interface is reduced and the current density increases according to the scaling relation discussed above. For a small enough delamination no significant current density effects would be experienced at the interface opposite the delamination, and the distribution of current across this interface would remain uniform (Figure 5.3b). However, as the delamination becomes larger, the current passing through the projected crack area is reduced until it ultimately becomes negligible in comparison to the original ideal current value (Figure 5.3c). At this point, the electro-active area at the interface opposite the delamination is reduced, and the crack zone is masked by the delamination. The dimensionless current, i^*, defined in Equation (5.8), provides a metric for the onset of such masking phenomena by comparing the current passing across the

projected crack area of Figure 5.1 to the ideal current that would pass across the same area if no delamination were present.

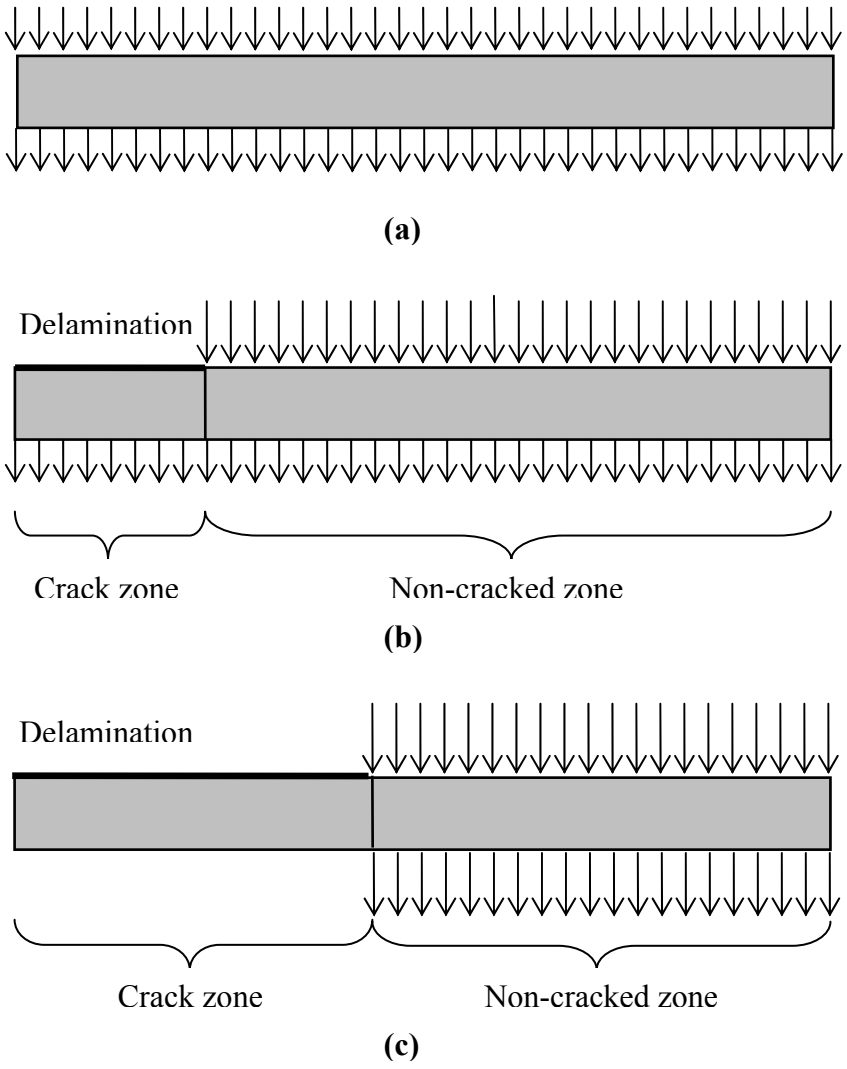

Figure 5.3. Progression of delamination growth from no crack (a) to a small crack with negligible masking effects (b) to a delamination resulting in masking (c)

In regions surrounding the delamination, current flow will bend around the delamination, as shown in Figure 5.4. In such regions, the current has both axial and radial components. The dimensionless radius, r^*, is used to define the radius at which

axial current flow is the dominant form of current flow. This radius, referred to as $r_{||}$, allows for the definition of the crack-affected area as a separate resistance that can be treated as a resistance in parallel with the bulk electrolyte resistance in areas not affected by the delamination crack. The dimensionless thickness, t^*, is the ratio of the electrolyte thickness to the crack radius and allows for a simplification of the complex geometric relations inherent in the analytical solution provided in Equation (5.6).

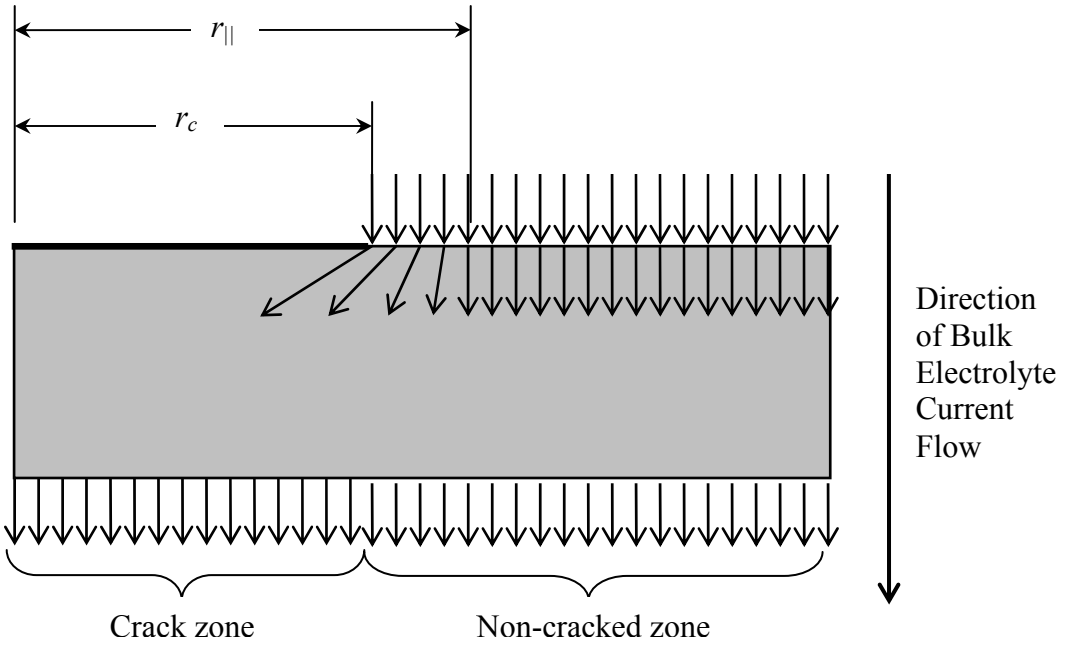

Figure 5.4. Current flow geometry for the establishment of r^*

Of these three dimensionless parameters, an expression for the dimensionless current, i^*, can be found readily from the analytic solution provided in Equation (5.6). First, the derivatives of Equation (5.6) are taken with respect to r and z, as shown in Equations (5.11) and (5.12). These derivatives are then cast as functions of r by evaluating them at $z = 0$ (i.e. Equations (5.13) and (5.14)). As expected the derivative in

the radial direction is zero, which results from the isopotential boundary condition applied along the non-cracked interface.

$$\frac{dV}{dz} = \frac{i''_{ideal}}{\sigma_{elec}}\left(\frac{R_0}{R_0 + r_c}\right) - \sum_{n=1}^{\infty} \frac{2i''_{ideal}}{\sigma_{elec}\lambda_n \cosh(\lambda_n t_{elec})} \frac{r_c}{R_0^2 - r_c^2} \frac{J_1(\lambda_n r_c)}{J_0^2(\lambda_n R_0)} [\cosh(\lambda_n z) J_0(\lambda_n r)] \tag{5.11}$$

$$\frac{dV}{dr} = -\sum_{n=1}^{\infty} \frac{2i''_{ideal}}{\sigma\ \lambda_n \cosh(\lambda_n t_{electrolyte})} \frac{r_c}{R_0^2 - r_c^2} \frac{J_1(\lambda_n r_c)}{J_0^2(\lambda_n R_0)} [\sinh(\lambda_n z) J_1(\lambda_n r)] \tag{5.12}$$

$$\frac{dV}{dz}(r,0) = \frac{i''_{ideal}}{\sigma_{elec}}\left(\frac{R_0}{R_0 + r_c}\right) - \sum_{n=1}^{\infty} \frac{2i''_{ideal}}{\sigma_{elec}\lambda_n \cosh(\lambda_n t_{elec})} \frac{r_c}{R_0^2 - r_c^2} \frac{J_1(\lambda_n r_c)}{J_0^2(\lambda_n R_0)} J_0(\lambda_n r) \tag{5.13}$$

$$\frac{dV}{dr}(r,0) = 0 \tag{5.14}$$

As stated, the dimensionless current is defined as the ratio of the ideal to actual current passing through the projected crack area shown in Figure 5.1. Each current can be defined as the integral of the respective current density over the projected crack area, as in Equation (5.15). The current density in the cracked case is expressed in terms of the ideal current density in Equation (5.16).

$$i^* = \frac{i_{cracked,\text{Projected Crack}}}{i_{ideal,\text{Projected Crack}}} = \frac{\iint_{\text{Projected Crack}} i''_{cracked}\, dA_{crack}}{\iint_{\text{Projected Crack}} i''_{ideal}\, dA_{crack}} = \frac{2\int_0^{r_c} i''_{cracked}\, r dr}{i''_{ideal} r_c^2} \tag{5.15}$$

$$\begin{aligned} i''_{cracked} &= \sigma_{elec} \frac{dV}{dz}(r,0) \\ &= i''_{ideal}\left(\frac{R_0}{R_0 + r_c}\right) - \sum_{n=1}^{\infty} \frac{2i''_{ideal}}{\lambda_n \cosh(\lambda_n t_{elec})} \frac{r_c}{R_0^2 - r_c^2} \frac{J_1(\lambda_n r_c)}{J_0^2(\lambda_n R_0)} J_0(\lambda_n r) \end{aligned} \tag{5.16}$$

Completing each integration and taking the ratio of the two currents yields an expression for i^*, with the eigenvalue λ_n previously defined in Equation (5.7).

$$i^* = \left(\frac{R_0}{R_0 + r_c} \right) - \frac{4}{R_0^2 - r_c^2} \sum_{n=1}^{\infty} \frac{J_1^2(\lambda_n r_c)}{\lambda_n^2 \cosh(\lambda_n t_{elec}) J_0^2(\lambda_n R_0)} \tag{5.17}$$

While the development of analytic expressions for the electrolyte voltage distribution and the dimensionless current is promising, these expressions demonstrate slow convergence when implemented. This slow convergence is the result of a singularity that is present at the delamination crack-tip where the current flux shifts from zero to a constant non-zero value as expressed in Equation (5.4). This singularity results from the model treating the delamination as an obstruction in a flow of current. Under actual SOFC operation the generation of current occurs at the electrode-electrolyte interface. Thus the treatment of the delamination crack as an obstruction within a flow may require further examination in future work. Considering this fact, it must also be reiterated that the non-uniform hydrogen concentrations at the anode-electrolyte interface demonstrated in previous chapters may lead to a non-uniform current density at the anode-electrolyte interface. Thus the uniform current density boundary condition given in Equation (5.4) may be subject to further refinement in future analyses.

5.2 Numerical (FEA) Model

The convergence issues encountered in the analytic solutions previously discussed can be mitigated through the use of numerical methods. Finite element analysis can be employed to provide a greater understanding of the effects of delamination cracks, especially with respect to the dimensionless parameters defined above. While an

expression for i^* can be developed directly from the analytic solution achieved, corroboration of this result using numerical techniques is pertinent. This corroboration can be achieved using FEA. Furthermore, derivation of an expression for the dimensionless radius, r^*, from the analytic solution is not quite as straightforward and can be greatly facilitated using finite element analysis.

As in the case of the anodic partial pressure distribution, a thermal conduction analogy can be established for ionic conduction within the electrolyte. This analogy allows for the use of thermal finite element analysis within the ANSYS FEA program to analyze the effects of delamination phenomena.

$$k\left(\frac{\partial^2 T}{\partial z^2}+\frac{\partial^2 T}{\partial r^2}+\frac{1}{r}\frac{\partial T}{\partial r}\right)=0 \tag{5.18}$$

$$\sigma_{elec}\left(\frac{\partial^2 V}{\partial z^2}+\frac{\partial^2 V}{\partial r^2}+\frac{1}{r}\frac{\partial V}{\partial r}\right)=0 \tag{5.19}$$

Employing this thermal analogy, the problem defined in Equations (5.1)-(5.5) and illustrated in Figures 5.1 and 5.2 can be established in a FEA program. In the studies presented the commercially available finite element analysis program ANSYS was used. The basic geometry consists of a quarter of a circular crack and the surrounding affected region. This geometry is shown in Figure 5.5. In the present model an isopotential boundary condition is applied along the non-cracked interface. Within the crack region a zero-flux boundary condition is applied, and a constant flux boundary condition is applied across the cracked interface outside of the crack region. For all cases studied a current density of 0.6 A/cm^2 was applied. The application of this constant flux condition

allows for both axial and radial current flow at the cracked interface and provides insight into the nature of the current flux at first entry into the electrolyte. Along the vertical boundaries (i.e., r = 0, r = R_0) zero-flux boundary conditions are applied.

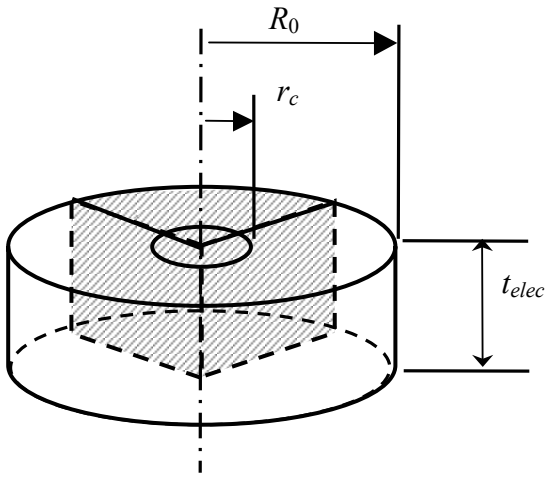

Figure 5.5. Basic button-cell geometry for delamination FEA Model

Two models are employed for the delamination finite element analysis: one for small geometries (r_c < 70 μm) and one for large geometries ($r_c \geq$ 70 μm). The basic parameters of these two models are outlined in Tables 5.1 and 5.2 below. For a large crack geometry, the non-cracked region is divided into two regions. One region extending from the crack tip to $r = 1.5r_c$ contains a more refined mesh size, with an element length of 2 μm. For this model a less refined mesh is used in regions further from the crack-tip ($r > 1.5r_c$) in order to reduce the total element count within ANSYS.

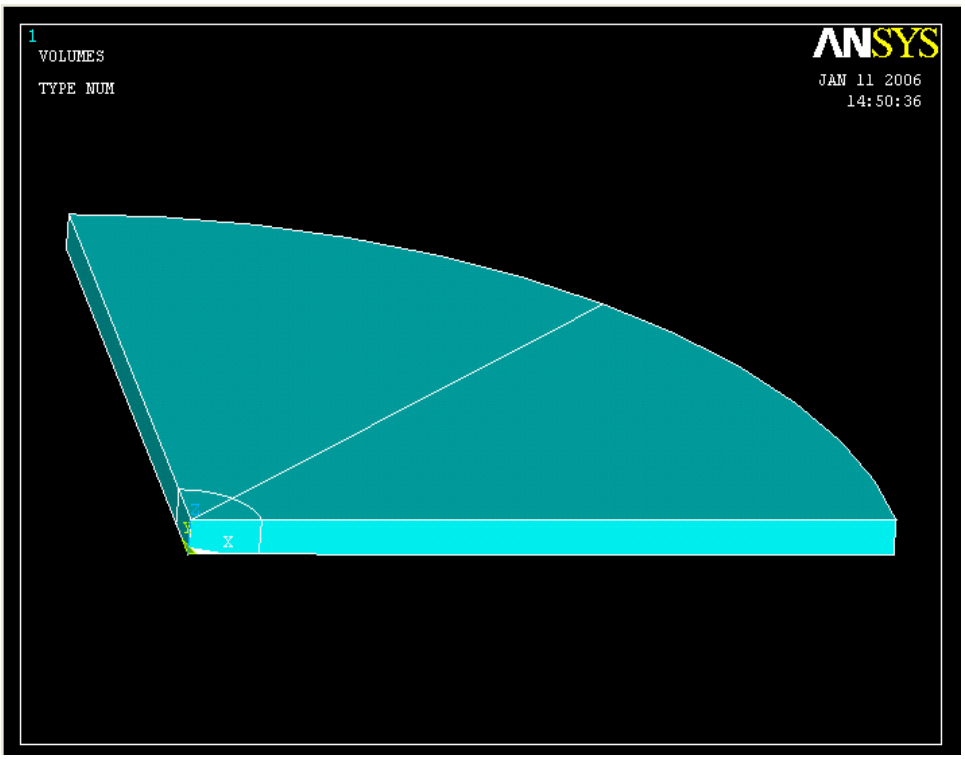

Figure 5.6. Small delamination crack FEA geometry

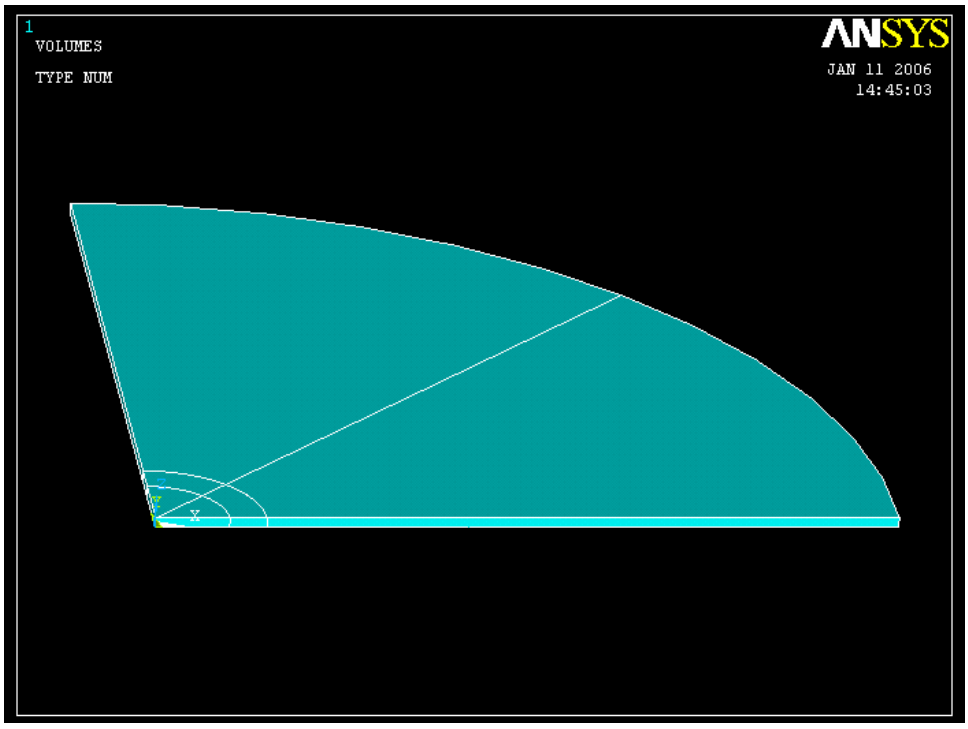

Figure 5.7. Large delamination crack FEA geometry

Table 5.1. Crack zone mesh size for small and large crack geometries

Crack Geometry	Element Divisions
Small Crack	20
Large Crack	20

Table 5.2. Non-Crack zone mesh size for small and large crack geometries

Crack Geometry	Non-Crack Region Element Length (μm)
Small Crack	2.00
Large Crack ($r_c < r < 1.5r_c$)	2.00
Large Crack ($r > 1.5r_c$)	5.00

The element size for the regions outside of the crack-zone is established through convergence studies of the smallest, largest, and nominal crack geometries. These geometries are given in Table 5.3 along with an outline of the geometries used in the study of button-cell radius effects on the ANSYS FEA model. In each case, convergence studies were performed for the largest outer radius. The nominal crack geometry is for a 20 μm crack radius. Convergence characteristics of the dimensionless radius, r^*, are shown in Figure 5.8.

The number of element divisions along lines within the crack-zone is based upon the convergence of i^*. The dimensionless current is determined through numerical integration of the current flux data within the projected crack area in each FEA model. Thus the number of data points used in the integration has a direct effect upon convergence, and the number of element divisions corresponds directly to the number of

data points used in the integration. The i^* convergence characteristics are shown in Figure 5.9 for two numerical integration methods: the trapezoidal rule and Simpson's rule. The method labeled Simpson's Rule is a combination of the 1/3 and 3/8 technique, with the 1/3 Rule being used perform the integration at the ends of the interval of data points.

Table 5.3. Crack and model geometries studied for button-cell radius effects

Crack Radius (μm)	Model Outer Radii (μm)				t^*
5	12.5	25	37.5	50	2.00
10	25	50	75	100	1.00
15	37.5	75	112.5	150	0.67
20	50	100	150	200	0.50
25	62.5	125	187.5	250	0.40
30	75	150	225	300	0.33
40	100	200	300	400	0.25
50	125	250	375	500	0.20
60	150	300	450	600	0.17
70	175	350	525	700	0.14
80	200	400	600	800	0.13
90	225	450	675	900	0.11
100	250	500	750	1000	0.10

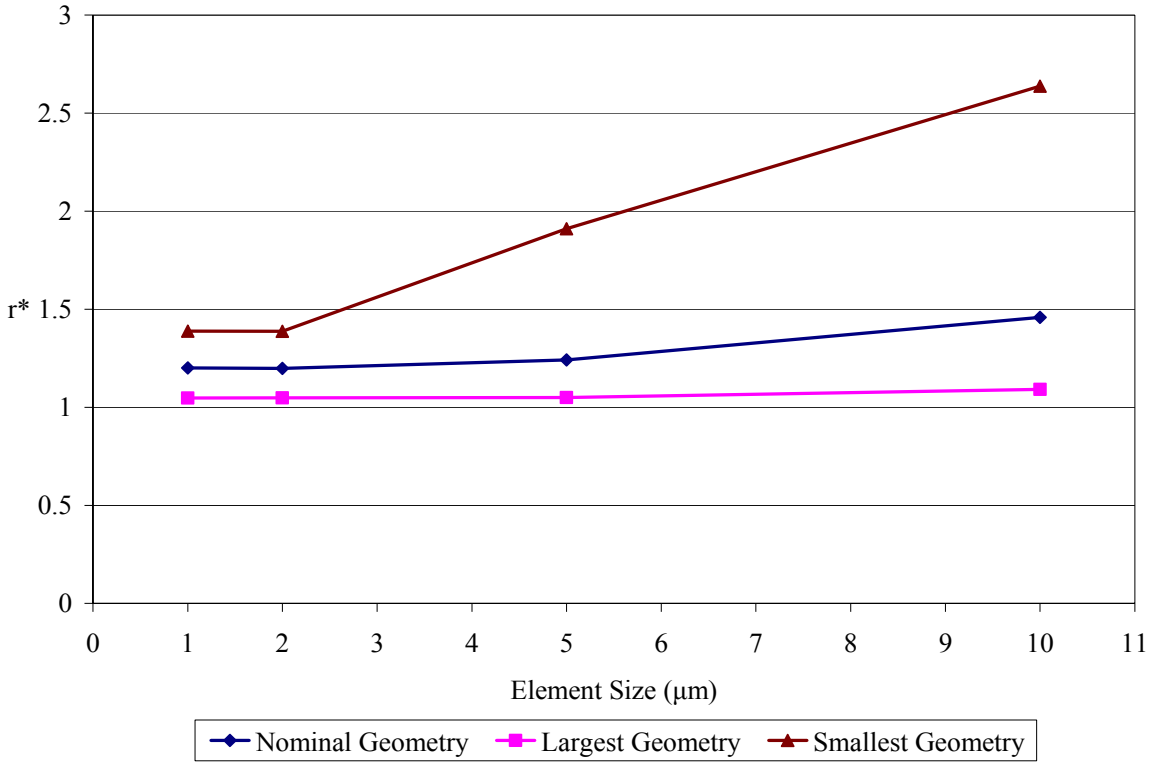

Figure 5.8. Convergence of *r** based on element size

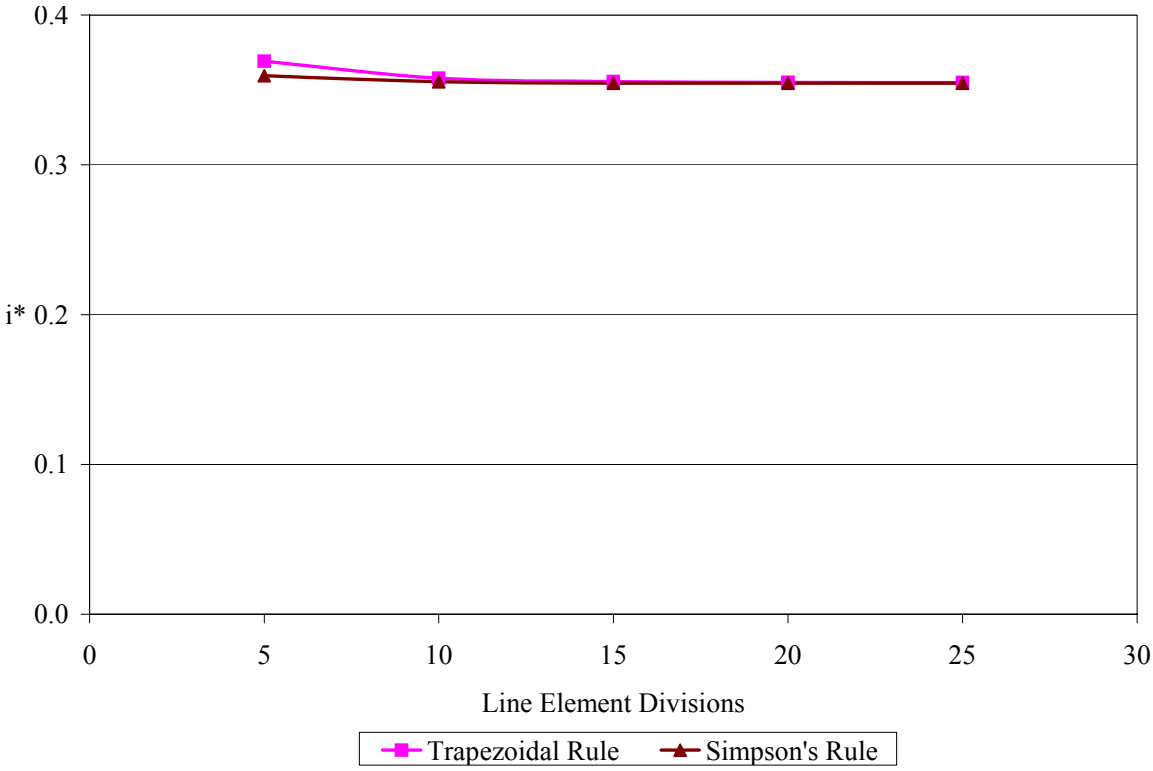

Figure 5.9. Convergence of *i** based on line element division within crack-zone

The geometries used in the following FEA studies are those corresponding to a button-cell radius of ten times the crack radius, as determined from the studies of button-cell radius effects outlined in Table 5.3. This geometry was used because of the strong dependence of i^* convergence on outer crack radius, which is rooted in the current density scaling factor M given below as demonstrated in Table 5.4 below.

$$M = \frac{R_0^2}{R_0^2 - r_c^2} \tag{5.20}$$

Table 5.4. Convergence of i^* as related to current density scaling (Crack Radius: 20 μm)

Outer Radius (μm)	i^*	% Change from Previous Value	R_0/r_c	Current Density Scaling Factor	% Change from Previous Value
50	0.422	--	2.50	1.19	--
100	0.369	12.49	5.00	1.04	12.50
150	0.361	2.25	7.50	1.02	2.26
200	0.358	0.78	10.00	1.01	0.79

The analytic solution developed for the case of delamination can be used in tandem with the FEA model to gain insight into the behavior of the dimensionless current. The dimensionless current i^* derived from the delamination analytic solution is given previously in Equation (5.17). Most important to note is that this expression is solely a function of geometry. This independence is further demonstrated through the FEA model. The nominal geometry is an electrolyte of 10 μm thickness with a delamination crack 20 μm in radius. For these studies this constant geometry is maintained with a variable ionic conductivity ranging from 0.01 to 0.10 S/cm. The

parameters of this study are outlined in Table 5.5, along with the results of representative ionic conductivity values over the range studied.

Table 5.5. Conductivity dependence study for dimensionless parameters

Crack Radius (μm)		20
Electrolyte Thickness (μm)		10
Current Density (A/cm^2)		0.6
Conductivity (S/cm)	i^*	r^*
0.02	0.358	1.198
0.04	0.358	1.198
0.06	0.358	1.198
0.08	0.358	1.198
0.1	0.358	1.198

The influence of electrolyte thickness on i^* and r^* has also been examined. Electrolyte thickness was varied from 1.0 to 200 μm for a nominal crack radius of 20 μm. An outline of these studies, with representative results, is provided in Table 5.6. Varying the electrolyte thickness allows for further examination of the t^* dependence of the dimensionless current and dimensionless radius.

In Figures 5.10-5.12, the FEA results based on the cases run from Tables 5.5 and 5.6 are compared to model for $i^*(t^*)$ given in Equation (5.17). As in the case of the hydrogen partial pressure distribution, the analytic and numerical solutions corroborate each other. As it is derived from the analytic solution for the delamination voltage distribution, the analytic expression for i^* shows a strong sensitivity to both the outer radius term, R_0, and the number of terms used in the series. For the crack geometries studied the ratio R_0/r_c was on the order of 1000 with the number of required series terms, n, on the order of 10000. This case yielded consistent convergence and agreement with

the finite element model for all geometries studied. This dependence presents a disadvantage by increasing computational burden and requiring a large crack-free region to establish a valid button-cell model.

Table 5.6. Electrolyte thickness dependence study for dimensionless parameters

Crack Radius (μm)			20
Ionic Conductivity (S/cm)			0.02
Current Density (A/cm^2)			0.6
Thickness (μm)	t^*	r^*	i^*
1	0.05	1.024	0.039
2	0.1	1.049	0.074
3	0.15	1.075	0.113
4	0.2	1.097	0.150
5	0.25	1.112	0.186
7.5	0.375	1.165	0.275
10	0.5	1.198	0.358
25	1.25	1.344	0.696
50	2.5	1.389	0.891
75	3.75	1.399	0.951
100	5	1.398	0.975
200	10	1.400	0.997

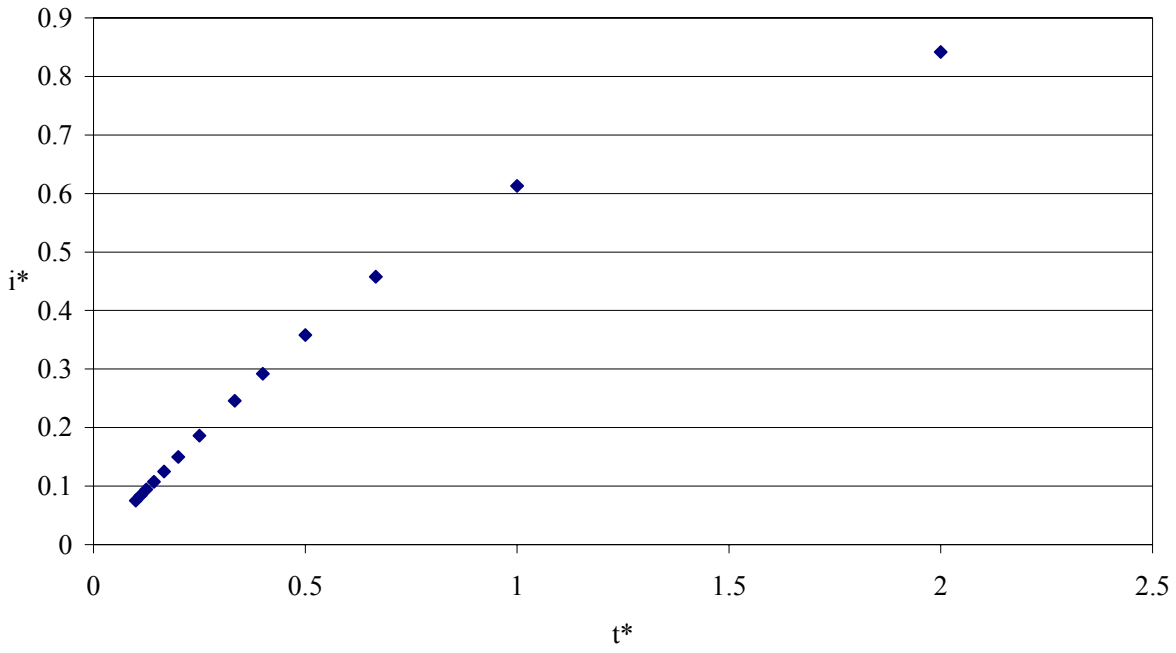

Figure 5.10. Results for $i^*(t^*)$, from FEA based on variable crack radius

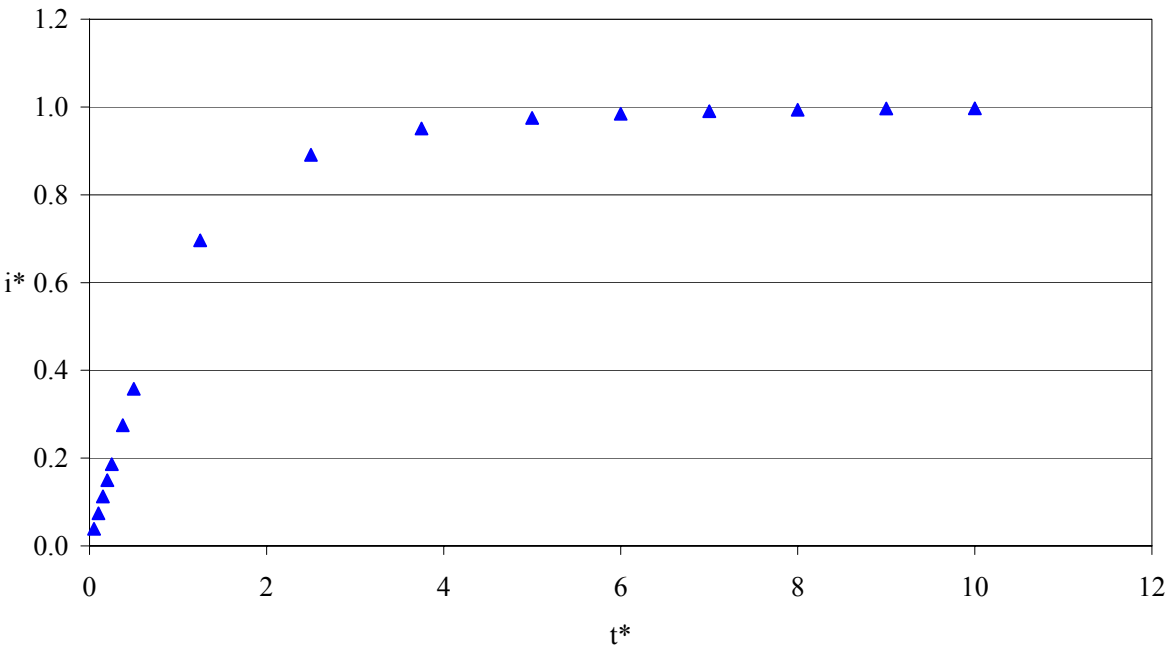

Figure 5.11. Results for $i^*(t^*)$, from FEA based on variable electrolyte thickness

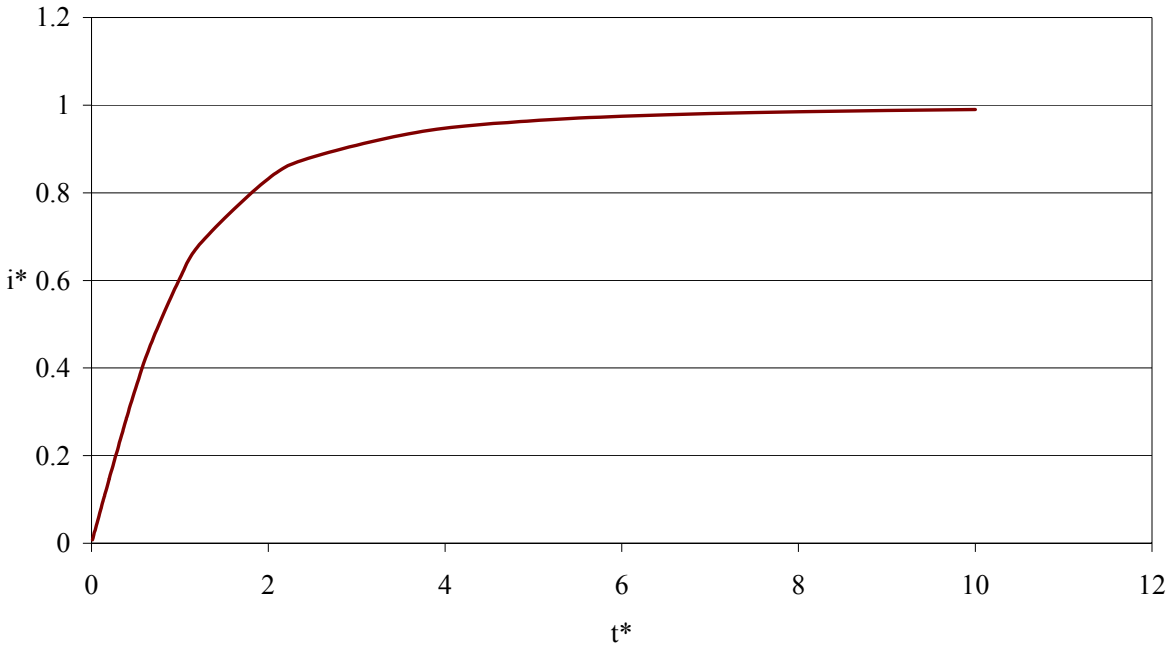

Figure 5.12. Results of analytic model of $i^*(t^*)$

The dimensionless radius shows a similar dependence upon t^*, as shown in Figures 5.13-5.15. Here, the results of the FEA studies varying crack radius and the results of the studies varying electrolyte thickness are shown along with a composite of the two datasets. The composite set takes r^* from the crack radius studies for $t^* < 2$, with the exception of the r^* values at $t^* = 0.05$ and 1.25. These two values of r^*, and those corresponding with $t^* > 2$, are taken from the studies varying electrolyte thickness.

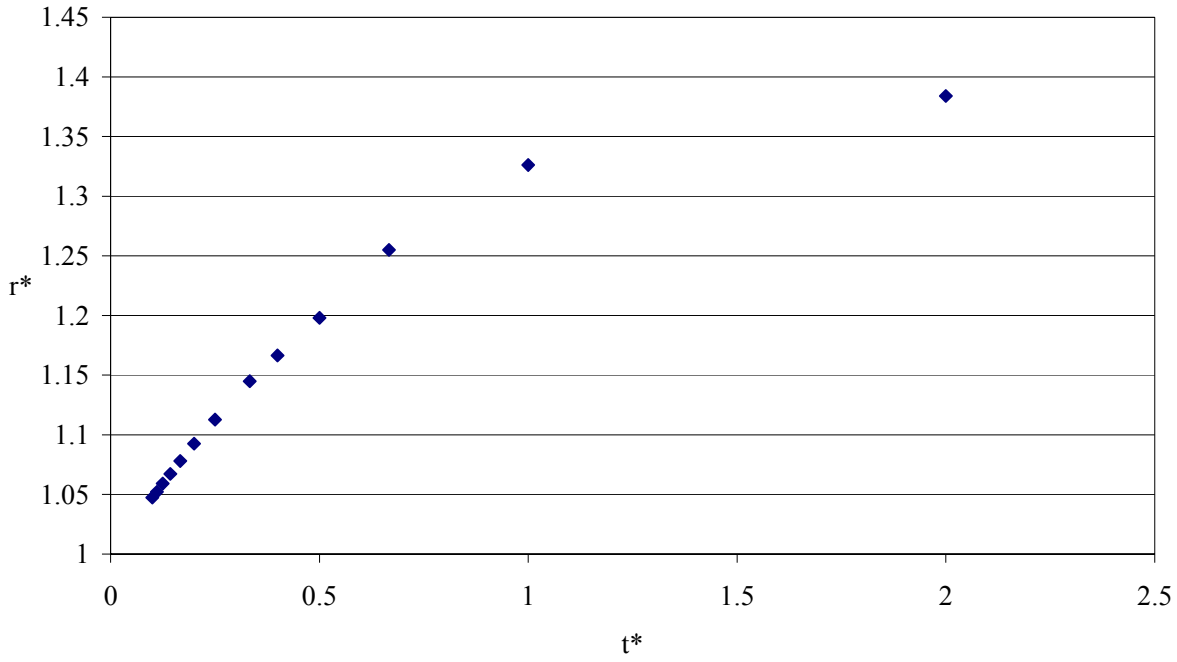

Figure 5.13. FEA results for $r^*(t^*)$ for variable crack radius studies

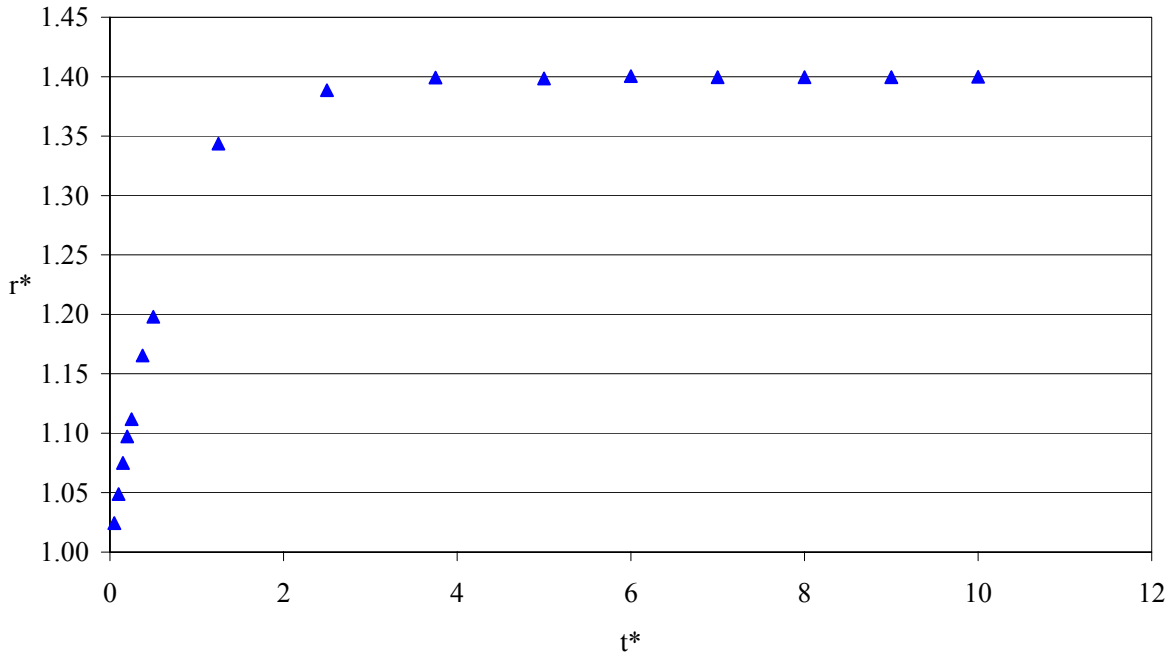

Figure 5.14. FEA results for $r^*(t^*)$ for variable electrolyte thickness studies

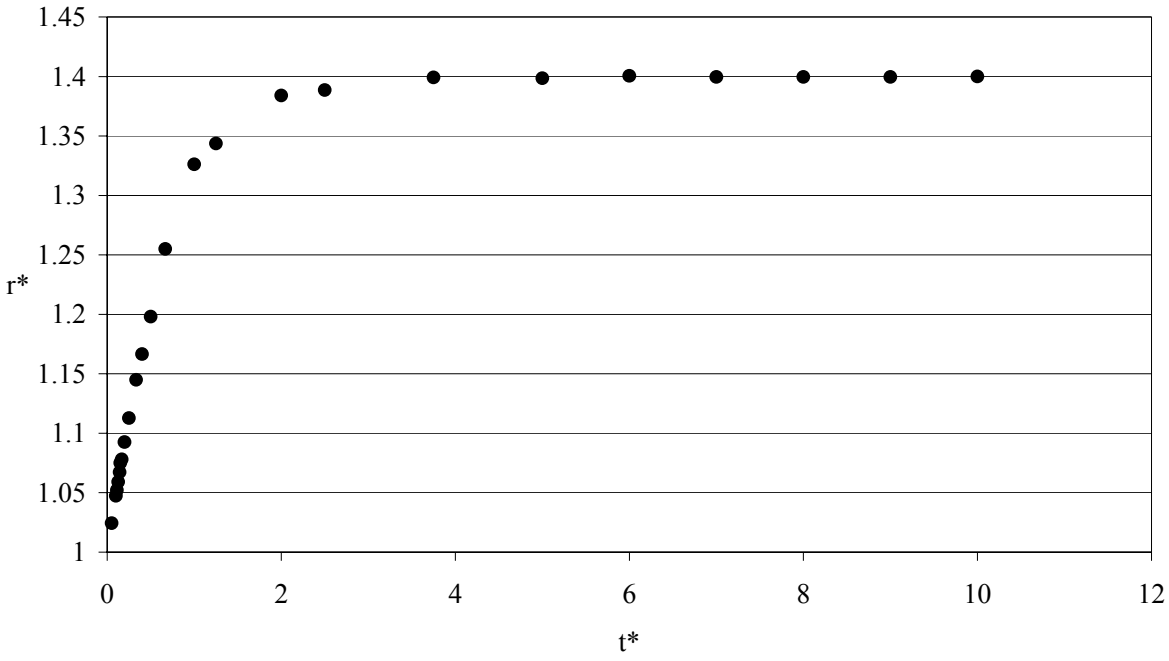

Figure 5.15. Finite element analysis results for $r^*(t^*)$, composite dataset

To simplify the analysis of delamination cracks within SOFCs two basic expressions are developed for i^* and r^* as functions of the dimensionless electrolyte thickness, t^*. In the expression for i^* derived from the analytic solution, the electrolyte thickness and crack radius that form the ratio t^* appear most prominently as the arguments of a hyperbolic cosine and a first order Bessel function of the first kind, respectively. Each of these functions can be expressed as series that are essentially polynomials as shown in Equations (5.21) and (5.22) [29]. Hence, it is proposed that the expression for $i^*(t^*)$ is a high order polynomial that can be obtained through curve fits. This fit has been obtained based on calculations from the analytic expression for i^* and is shown in Figures 5.16, as well as in Equation (5.23).

$$\cosh(x) = 1 + \frac{x^2}{2!} + \quad \frac{x^4}{4!} + \frac{x^6}{6!} + \cdots \tag{5.21}$$

$$J_1(x) = \sum_{n=0}^{\infty} \frac{(-1)^n x^{2n+1}}{2^{2n+1} n!(n+1)!} = \frac{x}{2} - \frac{x^3}{2^3(2!)} + \frac{x^5}{2^5(2!)(3!)} - \frac{x^7}{2^7(3!)(4!)} + \cdots \tag{5.22}$$

$$\begin{aligned} i^* = & -1\times10^{-5}(t^*)^6 + 0.0004(t^*)^5 - 0.0078(t^*)^4 \\ & + 0.0701(t^*)^3 - 0.3423(t^*)^2 + 0.8828(t^*) - 0.0095 \end{aligned} \tag{5.23}$$

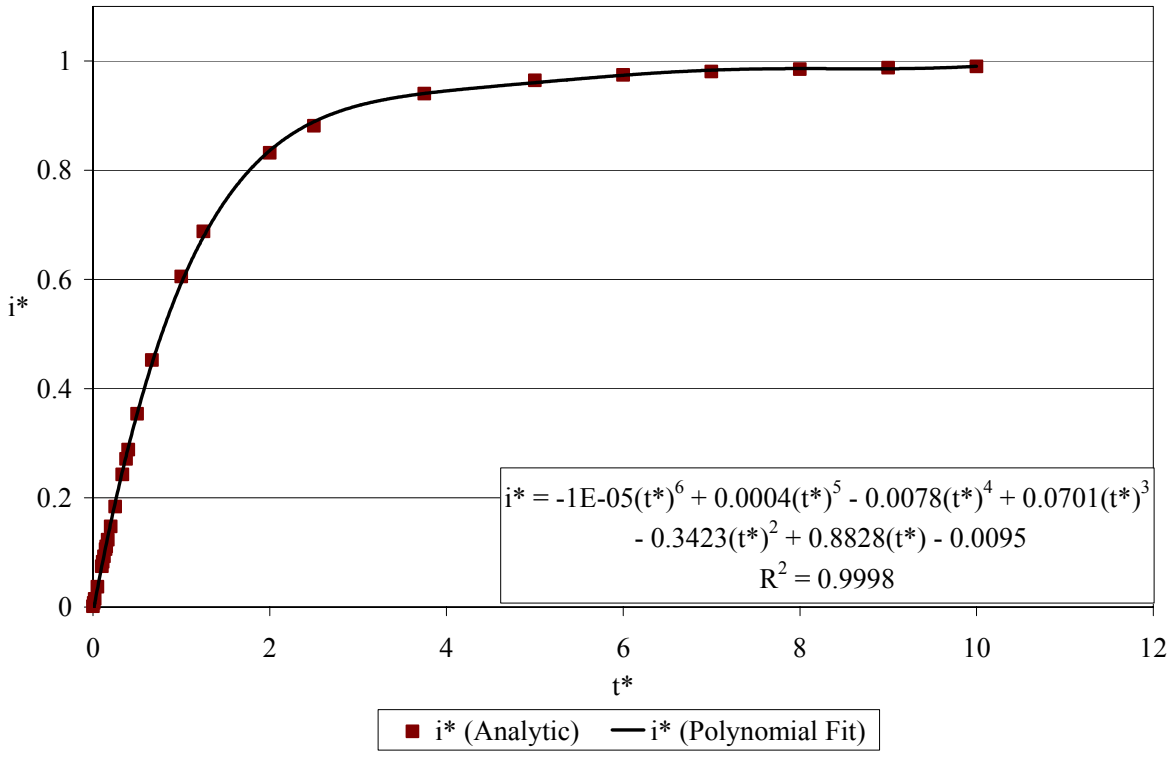

Figure 5.16. Polynomial fit model of $i^*(t^*)$

An expression for the dimensionless radius, r^*, can be found using the composite data obtained from the finite element studies. An exponential fit for $r^*(t^*)$ is generated using a linear transform of the dimensionless radius, as shown in Equation (5.24). This transformed data is plotted versus t^* and a linear fit is obtained as shown in Figure 5.17. This fit can then be used to cast the dimensionless radius, r^*, as a function of the

dimensionless thickness t^*, as shown in Equation (5.25). The resulting fit for $r^*(t^*)$ is shown in Figure 5.18.

$$r^* \to \ln(1.4 - r^*) \tag{5.24}$$

$$r^* = 1.4 - \exp(-1.6322t^* - 0.848) \tag{5.25}$$

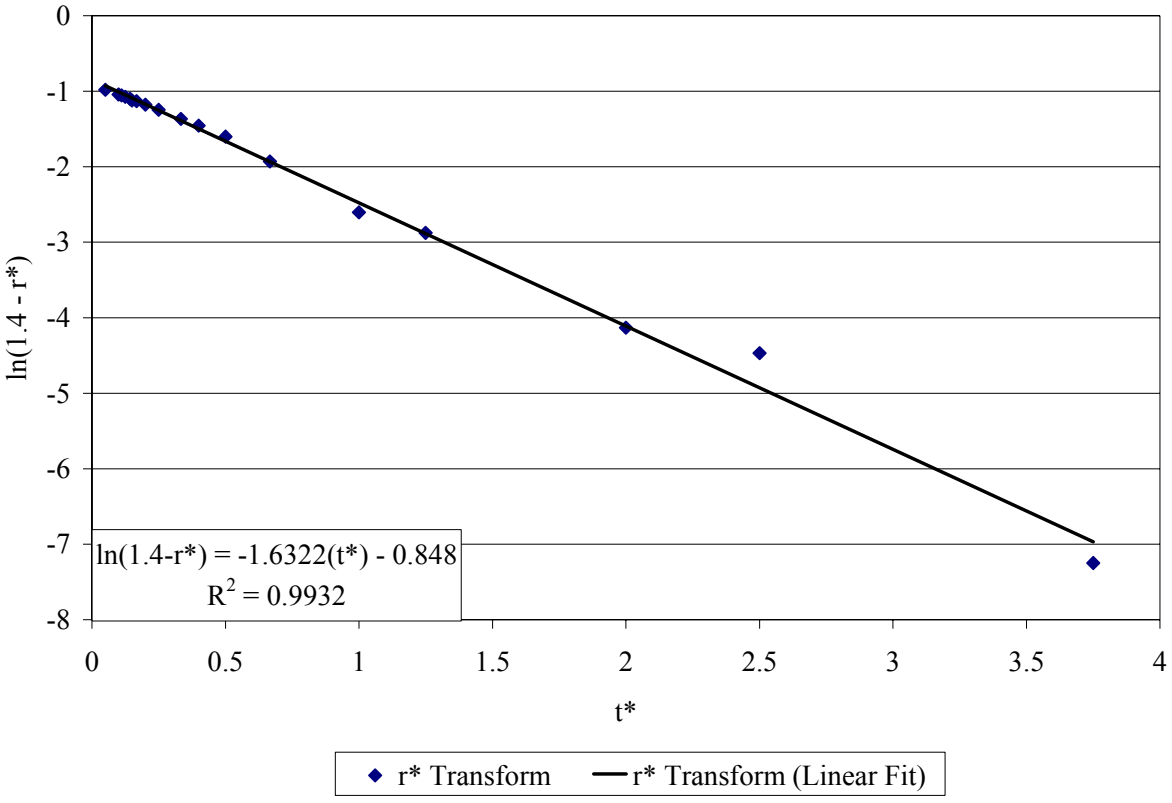

Figure 5.17. Linear transform for $r^*(t^*)$

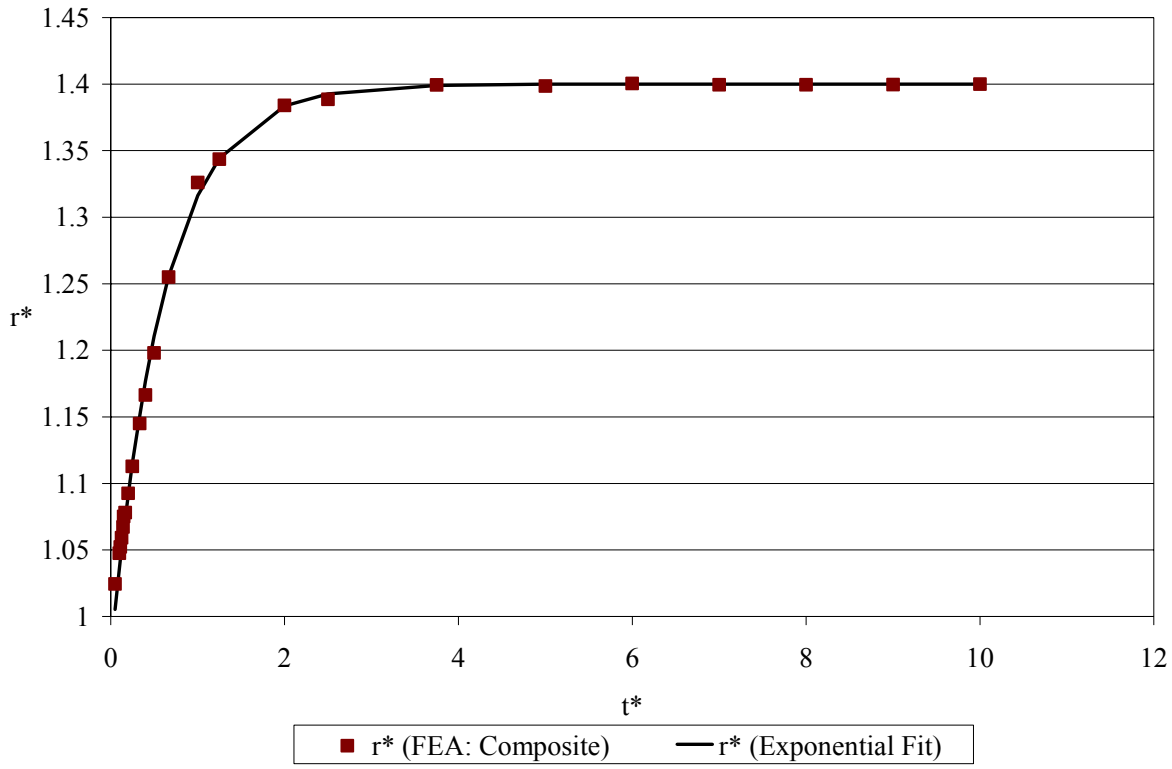

Figure 5.18. Exponential fit model of $r^*(t^*)$

With the dimensionless parameters of Equations (5.8)-(5.10) properly defined, further analysis of the effects of a single delamination can be performed. Most importantly the effects of a delamination on electrolyte area specific resistance (ASR) can be examined. Using the dimensionless radius, the section of electrolyte containing non-parallel current flow caused by the crack can be removed and treated as a resistance in parallel with the remaining bulk electrolyte, as shown in Figure 5.19. This section of electrolyte is termed the "affected area."

Using the expression developed for the electrolyte voltage distribution in the presence of a delamination crack, an expression for the electrolyte area specific resistance (ASR) can be found. The ASR for the affected area of the electrolyte is defined in

Equation (5.26). The crack-affected area is defined as extending to the radius at which the flow current is approximately parallel. This radius is previously defined in Equation (5.9) as $r_{\|}$. It can also be defined as the product of the dimensionless radius, r^*, and the crack radius, as shown in Equation (5.26). The resistance of the affected area is defined in Equation (5.27) as the ratio of the ideal voltage drop to the total current passing through the affected area. Applying current conservation allows for evaluation of the integral in the denominator of Equation (5.27) at the non-cracked interface. This step allows for simplified integration. The resulting expression for the area specific resistance is given in Equation (5.28).

$$ASR_{\text{affected area}} = \pi\left(r_c r^*\right)^2 R_{\text{affected area}} \tag{5.26}$$

$$R_{\text{affecd area}} = \frac{\Delta V_{ideal}}{i_{\text{affected area}}} = \frac{V\left(R_0, t_{elec}\right) - V\left(R_0, 0\right)}{2\pi \int_0^{r^* r_c} i''_{cracked} r dr} \tag{5.27}$$

$$R_{\text{affected area}} = \frac{\dfrac{t_{elec}}{\sigma_{elec}} - \dfrac{2r_c}{\sigma R_0\left(R_0 - r_c\right)} \displaystyle\sum_{n=1}^{\infty} \frac{J_1\left(\lambda_n r_c\right)\sinh\left(\lambda_n t_{elec}\right)}{\lambda_n^2 \cosh\left(\lambda_n t_{elec}\right) J_0\left(\lambda_n R_0\right)}}{\pi\left(r^* r_c\right)^2 - \dfrac{4\pi r^* r_c^2}{R_0\left(R_0 - r_c\right)} \displaystyle\sum_{n=1}^{\infty} \frac{J_1\left(\lambda_n r_c\right) J_1\left(\lambda_n r^* r_c\right)}{\lambda_n^2 \cosh\left(\lambda_n t_{elec}\right) J_0^2\left(\lambda_n R_0\right)}} \tag{5.28}$$

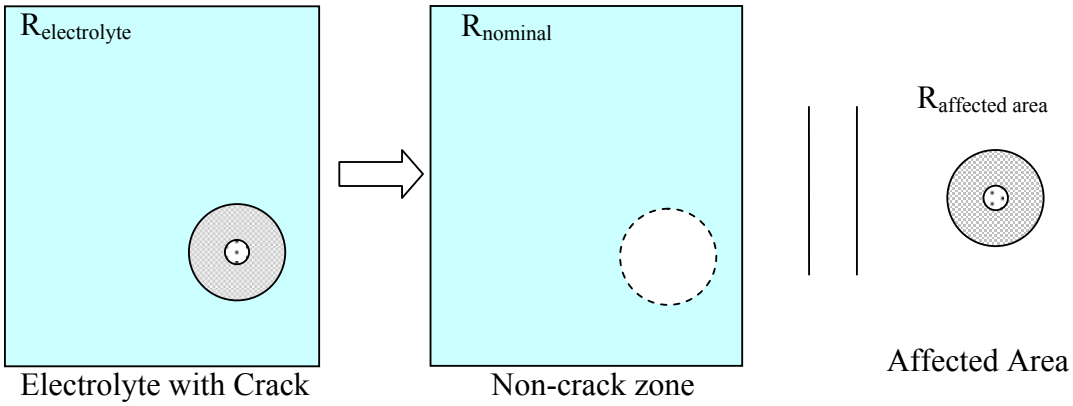

Figure 5.19. Division into parallel resistances of a section of electrolyte containing a single delamination crack

The effects of a delamination on area specific resistance within the affected area are shown for several electrolyte thicknesses in Figure 5.20. The minimum and maximum crack radii analyzed are 1.0 μm and 200 μm, respectively. Each case demonstrates an apparently exponential dependence on the dimensionless thickness, t^*. This dependence and the behavior of the dimensionless current, i^*, can provide insight into the phenomena of masking, in which unused cross-sections of the electrolyte result from a delamination crack. As t^* decreases to below 0.15, the dimensionless current drops to approximately 0.10. That is, the current crossing the interfacial surface opposite the delamination is only 10% of the ideal current. It is at this point that masking of the region of electrolyte containing the delamination can be assumed. For all of the cases shown in Figure 5.20, this limit falls within the range of t^* where the ASR of the crack-affected region increases to values significantly greater than the nominal ASR of the unaffected regions of the electrolyte. This nominal ASR is approached asymptotically

for increasing t^*. As the size of a delamination grows, its resulting resistance effects within the crack-affected area become more significant until masking is reached. For thinner electrolytes this transition to masking is much more abrupt than for thicker electrolytes.

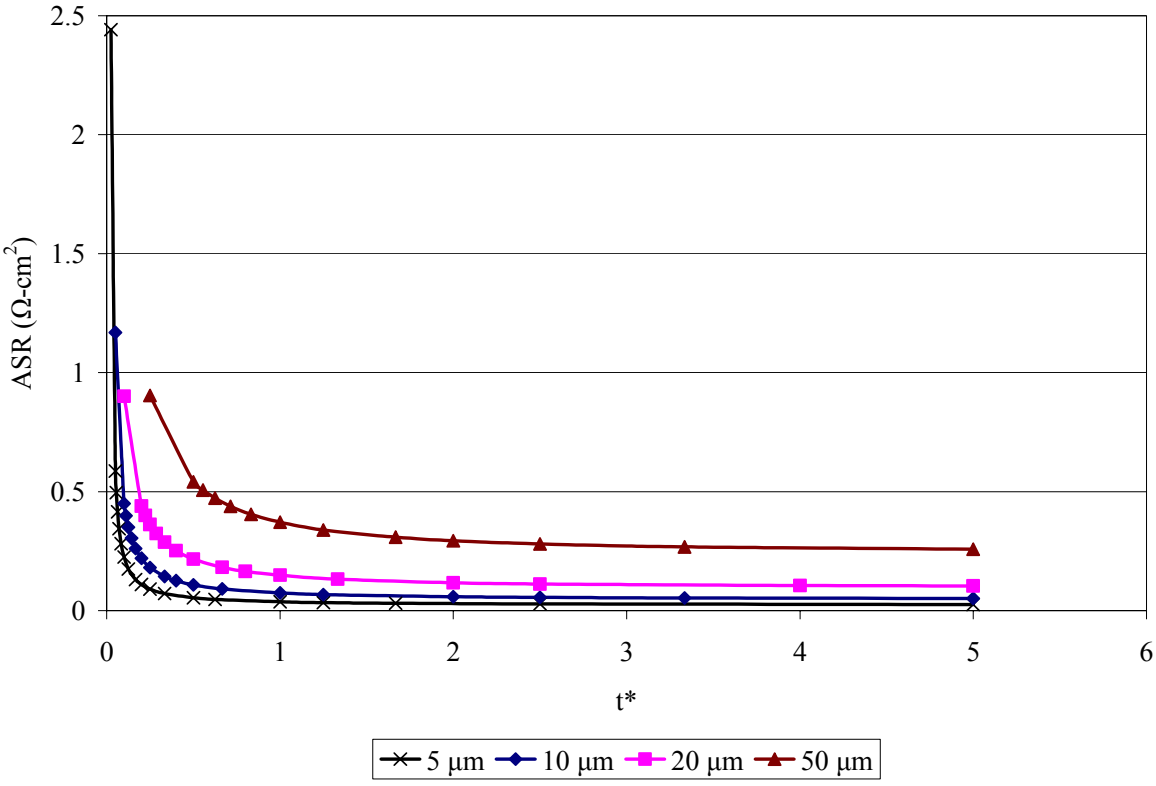

Figure 5.20. Dependence of crack-affected area ASR on t^* for several electrolyte thickness values (1.0 µm < r_c < 200 µm)

CHAPTER 6

CONCLUSION

Resistance effects that arise from increased transport path lengths within solid oxide cells have been analyzed through the analytic and numerical modeling of key mass and electronic transport phenomena. These resistance effects are collectively referred to as constriction resistance effects because the increase in transport path length directly results from reductions in active transport area. Two means of reducing active transport area within solid oxide cells have been explored within the preceding chapters. The first, and most emphasized, of these means are the reductions in mass and electronic transport area that arise from solid oxide cell interconnect and anode design. The study of these geometry effects focused primarily on the mass and electronic transport effects of fuel stream and interconnect contact lengths within solid oxide fuel cell anodes. However, the effects cell geometry has upon solid oxide electrolysis cell performance were also considered. Of secondary emphasis were the resistance effects of delamination cracking phenomena about the anode-electrolyte interface of SOFCs.

The performance of the anode layer of solid oxide fuel cells was examined using analytic solutions of the Laplace equation for mass and electronic transport. The solutions obtained show that significant resistance effects can be attributed to actual SOFC interconnect geometry in comparison to the common button-cell assumption. For a representative anode and interconnect geometry (750 μm thick, 2.0 mm unit cell width, and length fraction of 0.50) resistances were found to be ~50% higher for hydrogen transport and ~36% higher for electronic transport. For mass transport, finite element

models constructed within ANSYS demonstrate strong agreement between analytic and numerical results, and the use of potential flow theory in the case of electronic transport predicts anode area specific resistance and resistivity values that agree with experimentally determined values [5].

In addition to showing the significance of geometry effects, the analytic model for hydrogen transport allows for the unique definition of a modified concept of limiting current density: a fuel depletion current density. This definition of limiting current density accounts for SOFC geometry when modeling actual cell geometry and reduces to the standard definition of limiting current density when applying a button-cell assumption. However, the fuel depletion current density does not vary with anode thickness in the same way as the traditional definition of limiting current density. Specifically, reducing anode thickness does not invariably increase the fuel depletion current density. For thin anodes increased sheet resistance effects will result in a decrease in the current density that can be achieved prior to the onset of fuel depletion at the anode-electrolyte interface.

The minimization of geometric resistance effects through the proper sizing of the fuel stream-anode and anode-interconnect contact areas was explored initially through parametric studies developed from a design of experiments approach. Mass transport was found to be effected primarily by fuel stream hydrogen concentration and current density. The geometric variables of unit cell width and length fraction demonstrated a secondary influence upon mass transport phenomena. Electronic transport was found to be affected primarily by the previously mentioned geometric variables. These parametric studies demonstrated the benefits of smaller SOFC unit cell widths. However, the effects

of unit cell width reduction on fuel stream pressure drop must be further considered to achieve a true optimization of SOFC geometry.

For the present work, unit cell geometries with smaller widths were shown to experience lower ohmic losses and achieve more stable anode lead voltages over a range fuel stream compositions and higher limiting current densities. Furthermore, narrower unit cell geometries achieve cell voltages and efficiencies that are significantly higher than those of SOFCs with larger unit cell geometries. This superior performance is attributed to the reduced influence of sheet resistance effects in narrower unit cell geometries, when a constant anode thickness is maintained. Finally, in fuel streams with lower concentrations of hydrogen, geometry effects lead to a dominant influence of mass transport on SOFC performance.

The parametric studies conducted for geometry effects on SOFC performance were run under reversed current loading with fuel stream steam concentration treated as the transport limiting variable. These two reversals effectively model a solid oxide electrolysis cell. Results of the SOEC performance parametric studies were similar to those conducted for SOFC performance. For SOEC operation smaller unit cell geometries demonstrated performance benefits that included better limiting current density performance and slightly reduced cell power requirements.

Finally, potential flow theory has been applied to modeling the effects of delamination cracking about the anode-electrolyte interface within a SOFC. Although analytic solutions can be obtained for the boundary value problem describing SOFC delamination phenomena, series terms within these solutions demonstrate slow convergence. The convergence issues encountered with analytic models of SOFC

delamination have been addressed using numerical techniques, specifically finite element analysis built upon a thermal analogy to ionic conduction. The FEA delamination models were applied in tandem with analytic solutions to develop expressions that describe the effects of delamination phenomena in terms of three key dimensionless parameters: a dimensionless current, a dimensionless electrolyte thickness, and a dimensionless radius. The FEA studies conducted and the expressions developed show that delamination cracking serves to significantly increase the resistance of crack-affected regions of the electrolyte. For certain crack geometries the delamination was shown to create inactive regions of electrolytic cross-section. This phenomenon is referred to as masking and has been shown to occur when the dimensionless thickness (i.e. the ratio electrolyte thickness to crack radius) decreases below 0.15. This limit corresponds to the current passing through the crack-affected regions of the electrolyte being only ten percent of the ideal current and is defined by the point at which the dimensionless current decreases below 0.10.

REFERENCES

1. Minh, N.Q., *Ceramic fuel cells.* Journal of the American Ceramic Society, 1993. **76**(3): p. 563-588.

2. Hawkes, G.L., et al. *CFD Model of a Planar Solid Oxide Electrolysis Cell for Hydrogen Production from Nuclear Energy*. in *The 11th International Topical Meeting on Nuclear Reactor Thermal-Hydraulics (NURETH-11)*. 2005. Popes' Palace Conference Center, Avignon, France.

3. O'Brien, J.E., et al., *Performance measurements of solid-oxide electrolysis cells for hydrogen production.* Journal of Fuel Cell Science and Technology, 2005. **2**(3): p. 156-63.

4. Chan, S.H. and Z.T. Xia, *Polarization effects in electrolyte/electrode-supported solid oxide fuel cells.* Journal of Applied Electrochemistry, 2002. **32**(3): p. 339-47.

5. Zhao, F. and A.V. Virkar, *Dependence of polarization in anode-supported solid oxide fuel cells on various cell parameters.* Journal of Power Sources, 2005. **141**(1): p. 79-95.

6. Kim, J.-W., et al., *Polarization effects in intermediate temperature, anode-supported solid oxide fuel cells.* Journal of the Electrochemical Society, 1999. **146**(1): p. 69-78.

7. Black, A.F., V. Singhal, and S.V. Garimella, *Analysis and prediction of constriction resistance for contact between rough engineering surfaces.* Journal of Thermophysics and Heat Transfer, 2004. **18**(1): p. 30-36.

8. Greenwood, J.A., *Constriction resistance and the real area of contact.* British Journal of Applied Physics, 1966. **17**(12): p. 1621-1632.

9. Timsit, R.S., *Electrical contact resistance: Properties of stationary interfaces.* IEEE Transactions on Components and Packaging Technologies, 1999. **22**(1): p. 85-98.

10. Rostami, A.A., A.Y. Hassan, and P.C. Lim, *Parametric study of thermal constriction resistance.* Heat and Mass Transfer, 2001. **37**(1): p. 5-10.

11. Timsit, R.S., *The potential distribution in a constricted cylinder.* Journal of Physics D (Applied Physics), 1977. **10**(15): p. 2011-17.

12. Lin, Z., J.W. Stevenson, and M.A. Khaleel, *The effect of interconnect rib size on the fuel cell concentration polarization in planar SOFCs.* Journal of Power Sources, 2003. **117**(1-2): p. 92-97.

13. Tanner, C.W. and A.V. Virkar, *A simple model for interconnect design of planar solid oxide fuel cells.* Journal of Power Sources, 2003. **113**(1): p. 44-56.

14. Gemmen, R.S. and C.D. Johnson, *Effect of load transients on SOFC operation - current reversal on loss of load.* Journal of Power Sources, 2005. **144**(1): p. 152-64.

15. Khaleel, M.A., et al., *A finite element analysis modeling tool for solid oxide fuel cell development: coupled electrochemistry, thermal and flow analysis in MARC(R).* Journal of Power Sources, 2004. **130**(1-2): p. 136-48.

16. Ferguson, J.R., J.M. Fiard, and R. Herbin, *Three-dimensional numerical simulation for various geometries of solid oxide fuel cells.* Journal of Power Sources, 1996. **58**(2): p. 109-22.

17. Campanari, S. and P. Iora, *Comparison of finite volume SOFC models for the simulation of a planar cell geometry.* Fuel Cells, 2005. **5**(1): p. 34-51.

18. Fleig, J. and J. Maier. *The influence of inhomogeneous potential distributions on the electrolyte resistance in solid oxide fuel cells*. 1997. Aachen, Germany: Electrochem. Soc.

19. Fleig, J., et al., *Inhomogeneous current distributions at grain boundaries and electrodes and their impact on the impedance.* Solid State Ionics, 1998. **113-115**: p. 739-747.

20. Hsiao, Y.C. and J.R. Selman, *Degradation of SOFC electrodes.* Solid State Ionics, 1997. **98**(1-2): p. 33-38.

21. Radovic, M., et al. *Effect of thickness and porosity on the mechanical properties of planar components for solid oxide fuel cells at ambient and elevated temperatures*. 2003. Cocoa Beach, FL, United States: American Ceramic Society.

22. Mazumder, S.K., et al., *Solid-oxide-fuel-cell performance and durability: Resolution of the effects of power-conditioning systems and application loads.* IEEE Transactions on Power Electronics, 2004. **19**(5): p. 1263-1278.

23. Eguchi, K., T. Hatagishi, and H. Arai, *Power generation and steam electrolysis characteristics of an electrochemical cell with a zirconia- or ceria-based electrolyte.* Solid State Ionics, 1996. **86-88**(pt 2): p. 1245-1249.

24. Reid, R.C., J.M. Prausnitz, and T.K. Sherwood, *The Properties of Gases and Liquids*. 3rd ed. 1977, New York: McGraw-Hill.

25. Incropera, F.P. and D.P. DeWitt, *Fundamentals of Heat and Mass Transfer*. 5th ed. 2002, New York: John Wiley and Sons.

26. Moore, W.J., *Physical Chemistry*. 4 ed. 1972, Englewood, NJ: Prentice-Hall.

27. Gemmen, R.S., *Analysis for the Effect of Inverter Ripple Current on Fuel Cell Operating Condition.* Journal of Fluids Engineering, 2003. **125**: p. 576-585.

28. Hino, R., et al., *R&D on hydrogen production by high-temperature electrolysis of steam.* Nuclear Engineering and Design, 2004. **233**(1-3): p. 363-75.

29. Myers, G.E., *Analytical Methods in Conduction Heat Transfer*. 2nd ed. 1998, Madison, WI: AMCHT Publications.